DETERMINATION OF THE CHARGE RADII OF SEVERAL LIGHT NUCLEI FROM PRECISION, HIGH-ENERGY ELECTRON ELASTIC SCATTERING

A dissertation submitted

to Kent State University in partial

fulfilment of the requirements for the

degree of Doctor of Philosophy

by

Al Amin Kabir

December, 2015

Dissertation written by

Al Amin Kabir

B.Sc., University of Dhaka, 2001

M.S., University of Dhaka, 2002

Ph.D., Kent State University, 2015

Approved by

_____, Chair, Doctoral Dissertation Committee
Dr. Bryon D. Anderson

_____, Members, Doctoral Dissertation Committee
Dr. Douglas W. Higinbotham

_____
Dr. John W. Watson

_____
Dr. D. Mark Manley

_____
Dr. Philip Bos

_____
Dr. Edgar Kooijman

_____
Dr. Jonathan Selinger

Accepted by

_____, Chair, Department of Physics
Dr. James T. Gleeson

_____, Dean, College of Arts and Sciences
Dr. James L. Blank

TABLE OF CONTENTS

ABSTRACT

Al Amin Kabir, Ph.D., December 2015 PHYSICS

DETERMINATION OF THE CHARGE RADII OF SEVERAL LIGHT NUCLEI FROM PRECISION, HIGH-ENERGY ELECTRON ELASTIC SCATTERING (144 PP.)

Dissertation Advisors: Dr. Bryon D. Anderson, Dr. Douglus W. Higinbotham, and Dr. John W. Watson

Analysis of high-energy electron scattering has been used to determine the charge radii of nuclei for several decades. Recent analysis of the Lamb shift in muonic hydrogen found an r.m.s. radius significantly different than the electron scattering result. To understand this puzzle we have analyzed the "LEDEX" data for the $(e, e^{'}p)$ reaction. This experiment includes measurements on several light nuclei, hydrogen, deuterium, lithium, boron, and carbon. To test our ability to measure absolute cross sections, as well as our ability to extract the charge radius, we tested our technique against the extremely well-measured carbon case and found excellent agreement using the Fourier-Bessel parametrization. We then extended the procedure to boron and lithium, which show nice agreement with the latest theoretical calculations. For hydrogen, we see clearly the limits of this technique and therefore, the charge radius is determined from the traditional extrapolation to $q^2 = 0$. We will show that there is a model dependence in extracting the charge radius of hydrogen and its unambiguous determination is very difficult with available electron-scattering measurements.

LIST OF FIGURES

LIST OF TABLES

ACKNOWLEDGEMENTS

I would like to express the deepest appreciation to my advisors Dr. Bryon D. Anderson, Dr. Douglus W. Higinbotham, and Dr. John W. Watson, who have the attitude and the substance of genius: they continually and convincingly conveyed a spirit of adventure in regard to research and scholarship. Without their guidance and persistent help this dissertation would not have been possible.

Besides my advisors, I would like to thank the rest of my thesis committee: Dr. D. Mark Manley, Dr. Jonathan Selinger, Dr. Edgar Kooijman, and Dr. Philip Bos for their insightful comments and encouragement, and also for the hard questions which gave me incentive me to widen my research from various perspectives.

In addition, thanks to Dr. Arshad Momen, Without his teachings, mentorship, and support, graduate school would not have been an option for me.

Last but not the least, I would like to thank my family: my wife, my parents, and to my brother and sister for supporting me spiritually throughout writing this dissertation and my life in general.

Chapter 1

INTRODUCTION

1.1 Motivation

From experiments performed near the beginning of 19^{th} century, it became clear that inside the atom there is a dense matter core or nucleus whose size is hundreds of times smaller than that of the whole atom. As time progressed, the importance of electron scattering experiments became apparent; the amount of information we can extract from the scattered electron allows us to visualize the nucleus and its constituents. From the earliest electron-scattering experiments at the University of Illinois [1], the Stanford University, and the University of Michigan [2–4], a picture of the sizes of nuclei emerged. Robert Hofstadter received the Nobel prize in Physics in 1961 for his pioneering studies of electron scattering in atomic nuclei and for the consequent discoveries concerning the structure of nucleons [5], [6]. Though the basic technique remains almost the same, technological advancements allow us to perform these experiments now with greater precision.

The charge distribution inside a nucleus is one of the basic experimental quantities used to test models of nuclear structure. The root-mean-square (rms) charge radius of a nucleus is one of the most important nuclear parameters concerning its size and structure [7]. High-energy electron scattering can be used to measure this radius via the electromagnetic interaction between the electron and the charge inside the nucleus.

In a typical electron scattering experiment, electrons measure a range of cross sections for which the rms radius can be extracted. Inside the nucleus, the positive

charge is distributed in a way that includes a fuzzy edge [8]. An electron, being negatively charged, is deflected when it strikes the nucleus according to how the charge is distributed inside the nucleus. The quantum mechanical wave particle duality tells us that, although electrons are particles, the deflected electrons will produce a diffraction pattern with a greater concentation of electrons at some angles and lesser at others. This diffraction pattern which includes a minima in the form factor, can be analyzed to tell exactly how large the charge distribution of the nucleus is. However, for very light nuclei, this diffraction pattern is not well defined. In these cases we find the size of the nuclei by finding the slope of the form factor as the momentum transfer goes to zero.

Beside electron scattering, the rms radius can also be deduced from atomic spectroscopy that measures the effect of finite nuclear size on the energy levels of atomic electrons [9]. Bound-state quantum electrodynamic calculations can exactly predict the size of a nucleus from the spectroscopic data. Our expectation is that both scattering and bound-state experiments should produce consistent results. Recently, an experiment was performed at the Paul Scherrer Institute (PSI) in Switzerland to determine the charge radius of the proton [10]. A muon was substituted for the usual electron in a hydrogen atom. Since a muon is 200 times heavier than an electon, the atomic radius is decreased but the energy shift in the spectra is increased. Measuring the energy shift from the $2S_{1/2}^{F=1}$ state to the $2P_{3/2}^{F=2}$ state, the charge radius of proton was estimated [11–16]. The result, $r_{rms} = 0.84087 \pm 0.00039$ fm [10], [17] for the proton's charge radius, surprised everyone; it is significantly different from the result of 0.895 ± 0.018 fm from a recent reanalysis of electron-scattering experiments [7], [18] or to the atomic hydrogen result "CODATA" (Committee on Data for Science and Technology) value of 0.879 ± 0.008 fm [19]. This is a significant, fundamental problem for nuclear physics and even for physics in general. Among other questions, even

the validity of QED and the established values of the fundamental constants (e.g., Rydberg constant) could be questioned.

Boron and lithium are very unstable targets. Lithium bonds chemically with other elements easily and boron whose natural form is powder, is very unstable against beam heating. Due to these difficulties, only a few successful electron scattering experiments have been ever performed on lithium and boron [20–22]. So, their charge radii are not known as well as for other nuclei.

In this work, we have analyzed two sets experiments performed in 2006-07 to help resolve the discrepency in the structure function of deuterium [23] and for the better determination of the charge radius values for boron and lithium [20]. Lithium was submersed in olive oil until it was put into the vacuum of the target chamber to ensure that it does not interact with other compounds and a boron-carbide was used as a target instead of pure boron to overcome the beam heating issue. These were some of the most successful lithium and boron targets ever made. Carbon and hydrogen were also as targets since their cross-section values were believed to be known to high precision, so that they can be used to cross-check our experimental procedure. We realized that these data sets would not only provide better measurements for the charge radii of boron, deuteron, and lithium, but might also provide new information about the proton charge radius.

1.2 Why Electron Scattering?

There is no direct way to see a subatomic system. For the size of quantum mechanical systems, indirect methods, such as scattering are a very useful and trustworthy way to probe the structure of particles and the underlying forces that hold them together. At the Thomas Jefferson National Accelerator Laboratory (JLab), high-energy electrons

are used to bombard static nuclei. Electrons are point particles and their electromagnetic interaction is known to a high degree of accuracy; the electromagnetic force is the best known of the fundamental forces . At the same time, the elecro-magnetic force has enough strength that it enables us to see much of the interior of the target with this probe. Because the electromagnetic force is known to high precision, the results can be described with confidence. For instance, that the proton interacts with electrons electro-magnetically immediately tells us that it has electical charge and is made up of charged constituents.

1.3 Classical Electron Scattering

Back in the early 1900s, Greiger and Marsden carried out scattering experiments with metallic foil targets such as aluminum, copper, silver, and gold, using alpha particles as the probe particles [24]. They used a lead collimator to direct alpha particles from a radioactive source onto the targets. On the other side of the target a zinc sulphide screen was placed with a movable microscope behind the screen [24].

They observed that most of the alpha particles were not deflected at all; but that of the particles that had suffered deflection, some were deflected back to the same side of the foil from where they were initially generated [24]. In fact, about one in 20,000 alpha particles were scattered through an angle greater than 90^0 by a gold film 0.4 microns thick [24]. This was large enough to rule out that they were caused by sucessive collisions. Later it was shown by Geiger that the most probable angle of deflection was 0.87^0 [25].

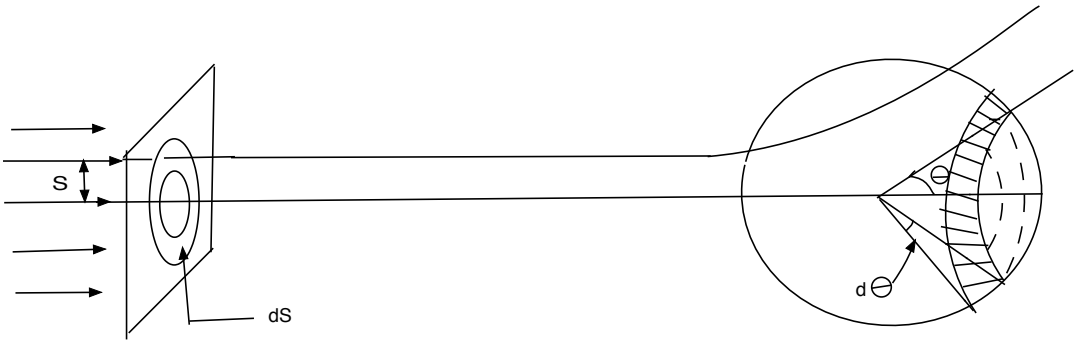

Fig. 1.1: Scattering of an incident beam of particles by a center of force [26].

Rutherford then [26] showed mathematically the probabilty that a particle will be scattered through a solid angle dΩ along the direction (Θ, ϕ) can be expressed as a differential scattering cross section [Fig.1.1], from which information about the target can be retreived, as

$$\frac{d\sigma}{d\Omega} = |\frac{s(\Theta)ds}{\sin(\Theta)d\Theta}|.$$

To obtain crosssections classically, one needs to consider trajectories of particles in the force fields. Let us consider a particle as in Fig. 1.1, that passes through a spherically symmetric force field [e.g., a Coloumb field] centered at the origin. The original trajectory of the particle is parametrized by the impact parameter, defined as the perpendicular distance between the center of force to the incident direction of the particle, as if there were no scattering, or the distance of closest approach. The scattering angle $\Theta(s)$ depends on this impact parameter. Knowing the initial conditions, the equations of motion for $\Theta(s)$, $s(\Theta)$ etc, can be obtained. A measurement of $d\sigma/d\Omega$ determines $s(\Theta)$, which in turn gives information about the potential or the force field and vice versa.

For the Geiger-Marsden experiment, the potential is the well-known Coulomb

potential:

$$V = \frac{Z_1 Z_2 e^2}{4\pi\epsilon_0 r},$$

where Z_1 is the charge of the scattered particle and Z_2 is the charge of the immobile target particle. The orbits are unbound in this Coulomb potential and have the shape of hyperbolas. For the incident kinetic energy E_k, the angle-impact parameter relation is

$$\frac{ds}{d\Theta} = -\frac{Z_1 Z_2 e^2}{8\pi\epsilon_0 E_k}\csc^2(\frac{\Theta}{2}).$$

Thus the differential scattering cross-section formula, called the Rutherford scattering cross section, becomes, [27]

$$\frac{d\sigma}{d\Omega} = (\frac{Z_1 Z_2 e^2}{16\pi\epsilon_0 E_k})^2\csc^4(\frac{\Theta}{2}), \tag{1.1}$$

where $d\Omega = 2\pi\sin\Theta d\Theta$. This formula agrees very well with experimental data. Rutherford's analysis of the Greiger-Marsden experiment indicated that the chief portion of an atom is empty space, but that there exists somewhere inside the atom, a very massive positively charged region that makes the entire atom overall electrically neutral. Rutherford, in his original paper, suggested than an atom contains at its center a charge whose magnitude is equal to an integral multiple of the electronic charge and is surrounded by a sphere with a homogeneous distribution of electrons. His theory gave birth to the idea of the nucleus and the hypothesis of the proton, a positively charged particle within the nucleus [24].

1.4 Quantum Scattering Formalism

Rutherford pictured an atom as similar to a solar system with positive charge at the center and electrons revolving around it, like the planets moving around the sun;

his theory was soon proved incomplete and ultimately incorrect. A new theory then emerged, based on quantum mechanics, and successfully explained the microscopic world where the classical theories were inconsistent. This provided a whole new perspective.

The marriage between quantum mechanics and the special theory of relativity then led to quantum electrodynamics (QED), or the relativistic quantum field theory of electrodynamics. QED describes all phenomena that involve electrically charged particles and this will be the ultimate theory for our present purposes.

In quantum mechanics we calculate the covariant scattering amplitude 'R' which is roughly related to differential scattering cross section in the following way [28]

$$\frac{d\sigma}{d\Omega'} = \frac{|R|^2}{F}, \tag{1.2}$$

where $d\Omega'$ is the Lorentz invariant phase-space factor and F is the incident flux of particles in the laboratory [28].

Let us now start calculating the elastic-scattering cross section for a spin $-1/2$ electron from a spinless point particle [the total kinetic energy of the system is conserved]. This interaction can be represented by a diagrammatic device known as a Feynman diagram. The relevant Feynmann diagram [27] for this case would be one like the following (Fig.1.2).

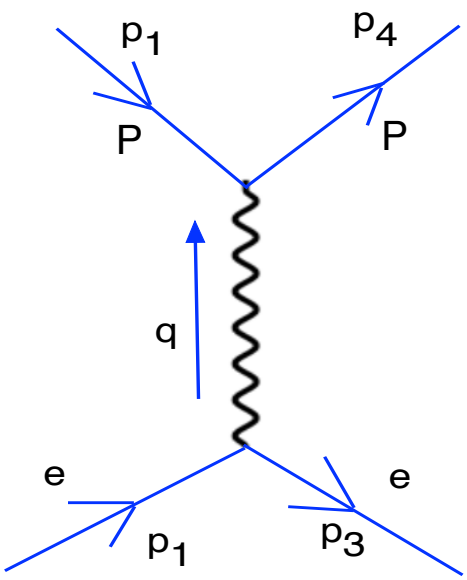

Fig. 1.2: Electron-spinless point particle scattering [27].

By using the Feynman rules for this diagram one obtains [28]

$$R = 2\pi^4 \int d^4q \overline{u}(p_3)(ie\gamma^\mu)u(p_1)\frac{-ig_{\mu\nu}}{q^2}\overline{u}(p_4)(ie\gamma^\mu)u(p_2)\delta^4(p_1 - p_3 - q)\delta^4(p_2 - p_4 + q)$$

$$R = -e^2\overline{u}(p_3)(\gamma^\mu)u(p_1)\frac{1}{q^2}\overline{u}(p_4)(\gamma^\mu)u(p_2). \tag{1.3}$$

The cross section can be found by finding the square of the modulus R and then carrying out the spin sums. For convenience we separate out the electron and spinless point particle part

$$|R|^2 = \frac{e^4}{q^4}L_e^{\mu\nu}(L_P)_{\mu\nu}. \tag{1.4}$$

Here $L_e^{\mu\nu} = \frac{1}{2}\sum_{\text{spin}}[\overline{u}(p_3)\gamma^\mu u(p_1)][\overline{u}(p_3)\gamma^\mu u(p_1)]^*$. $L_P^{\mu\nu}$ has the same structure, except that we do not have to perform the spin- summation over it. By performing the sum and using the trace theorem and the properties of γ matrices, the expression for

the $L_e^{\mu\nu}$ and $L_P^{\mu\nu}$ become, [27] [28]

$$L_e^{\mu\nu} = 2(p_1^\mu p_3^\nu + p_3^\mu p_1^\nu - (p_1.p_3 - m^2)g^{\mu\nu}) \quad (1.5)$$

$$L_P^{\mu\nu} = (p_2 + p_4)^\mu (p_2 + p_4)^\nu. \quad (1.6)$$

Now, substituting these expressions in equation 1.2, with the assumption that the electron mass is negligible compared to the target mass, we obtain the scattering cross-section in the lab frame (Fig.1.3) (where the target is at rest and $p = (M, 0, 0, 0)$. An electron with incident energy E scatters at Θ emerging with energy E' and $(E, E' \gg m_e)$, so, $p_1 = E(1, \vec{k}), p_3 = E(1, \vec{k'})$ and $\vec{p_1}.\vec{p_3} = \cos\Theta)$. The result for the spinless and structureless target can be found [28], and is known as the Mott cross section [29].

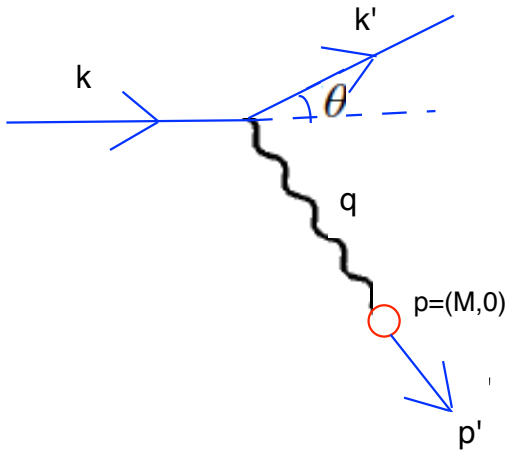

Fig. 1.3: Electron-spinless point paricle scattering in the lab frame.

$$\frac{d\sigma}{d\Omega'}|_{\text{point}} = \frac{d\sigma}{d\Omega'}|_{\text{Mott}} = \frac{(Z\alpha)^2 E^2}{4k^2 \sin^4(\Theta/2)} \frac{E'}{E} \cos^2\frac{\Theta}{2}, \quad (1.7)$$

where, $q^2 \sim -2k \cdot k' = -4EE' \sin^2\frac{\Theta}{2}$ and also $q^2 = -2p \cdot q = -2\nu M$. It is easy to see from this equation that, in the classical limit, the formula becomes the Rutherford

scattering formula [27].

Now, let us consider that we have an overall spinless charge distribution (e.g., ^{12}C nuclei), normalized so that

$$\int \rho(r) d^3r = Z. \tag{1.8}$$

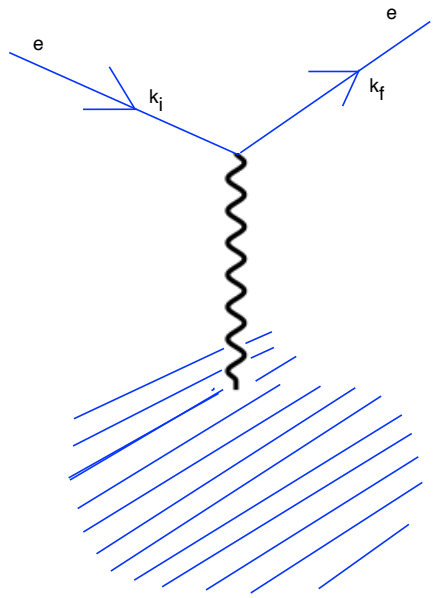

Fig. 1.4: Electron-spinless charge distribution scattering.

The Fourier transformation of the charge distribution is given by

$$F(q) = \frac{1}{Z}\int_0^\infty \rho(r)\frac{\sin(q.r)}{qr} 4\pi r^2 dr. \tag{1.9}$$

The elastic scattering cross section for this spinless charge distribution by an unpolarized electron beam then becomes [28]

$$\frac{d\sigma}{d\Omega'}|_{\text{distribution}} = (\frac{d\sigma}{d\Omega'})_{\text{Mott}}|F(q)|^2. \tag{1.10}$$

The term $F(q)$ is known as the form factor, which arises due to the fact that the target has structure. In other words, an unpolarized electron scattering off an

extended spinless source is equal to scattering off a point source modified by a form factor.

Let us now consider the scattering of an electron from a spin $-1/2$ particle (say a proton) that has internal structure (Fig.1.5). The Feynman diagram is

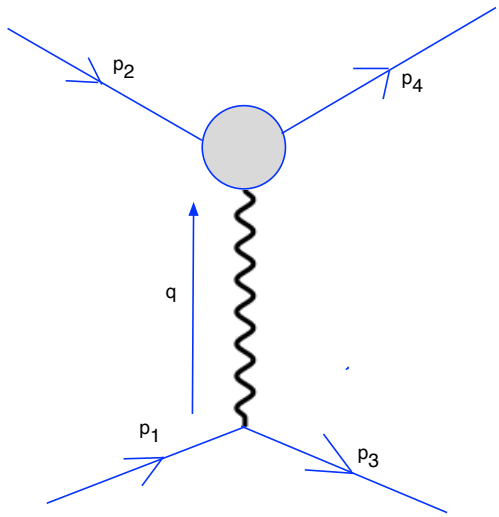

Fig. 1.5: e-p scattering [27].

We have placed a "blob" at the proton-photon vertex to reflect that we do not have any idea about what is happening there. However, the scattering is assumed to be elastic [27]. In the same way as we discussed earlier for e-point particle scattering, the covariant amplitude reads as,

$$|R|^2 = \frac{e^4}{q^4} L_e^{\mu\nu} (K_P)_{\mu\nu}. \tag{1.11}$$

$L_e^{\mu\nu}$ has the same form as before, whereas $(K_P)_{\mu\nu}$ is found to have the form [27]

$$(K_P)_{\mu\nu} == K_1(-g^{\mu\nu} + \frac{q^\mu q^\nu}{q^2}) + \frac{K_2}{M^2}(p^\mu + \frac{1}{2}q^\nu)(p^\nu + \frac{1}{2}q^\mu), \tag{1.12}$$

where, K_1, K_2 are unknown scalars or form factors that are directly related to the scattering cross section, M is the mass of the proton, and we choose $q = p_4 - p_2$, and

$p_2 = p$. Once again if we evaluate $|R|^2$ in the lab frame [27, 28, 30]:

$$|R|^2 = \frac{e^2}{4EE' \sin^4(\Theta/2)}[2K_1 \sin^2(\Theta/2) + K_2 \cos^2(\Theta/2)] \tag{1.13}$$

$$\frac{d\sigma}{d\Omega'} = (\frac{\alpha}{4ME \sin^2(\Theta/2)})^2 \frac{E'}{E}[2K_1 \sin^2(\Theta/2) + K_2 \cos^2(\Theta/2)] \tag{1.14}$$

Equation 1.14 is known as the Rosenbluth formula. This expression can also be written in terms of electric and magnetic form factors (G_E, G_M) with the following substitutions [27] $K_1 = -q^2 G_M^2$, $K_2 = |2M|^2 \frac{G_E^2 - \tau G_M^2}{1+\tau}$, and $\tau = -\frac{q^2}{4M^2}$. Then

$$\frac{d\sigma}{d\Omega'} = (\frac{\alpha^2}{4E^2 \sin^4(\Theta/2)}) \frac{E'}{E}[2\tau G_M^2 \sin^2(\Theta/2) + \frac{G_E^2 + \tau G_M^2}{1+\tau} \cos^2(\Theta/2)]$$

$$\frac{d\sigma}{d\Omega'} = (\frac{d\sigma}{d\Omega'})_{\text{Mott}}[2\tau G_M^2 \tan^2(\Theta/2) + \frac{G_E^2 + \tau G_M^2}{1+\tau}]. \tag{1.15}$$

In the limiting case $q^2 \to 0$, G_E coincides with the electric charge and G_M coincides with the magnetic moment of the proton, normalized to the elementary charge and nuclear magneton, respectively [30].

The spin-1 (D,^{6}Li) and spin-3 (^{10}B) nuclei have magnetic dipole moments and and charge quadrapole moments apart from the charge monopole and it is very much anticipated that these terms will be present in the cross-section formulation. For an unpolarized electron beam, the elastic scattering cross section for a spin-1 nucleus is found to be [31]

$$\frac{d\sigma}{d\Omega'} = (\frac{d\sigma}{d\Omega'})_{\text{Mott}}[A + B \tan^2 \frac{\Theta}{2}], \tag{1.16}$$

where, $A = G_C^2 + \frac{2}{3}\tau G_M^2 + \frac{8}{9}\tau^2 G_Q^2$, $B = \frac{4}{3}\tau(1+\tau)G_M^2$ and G_C, G_M, G_Q are the charge monopole, magnetic dipole, and electric quadrupole terms, respectively. This then, is the basic form of the differential cross section for elastic electron scattering for the purposes of this work.

Chapter 2

EXPERIMENTAL SETUP

2.1 Overview

The data analyzed for this dissertation was acquired during the "LEDEX" experiment, performed in 2006-07 at the state-of-the-art Jefferson Laboratory's (JLab) continuous Electron Beam Accelerator Facility (CEBAF) in experimental Hall A. The construction project for JLab started in 1987 and in 1995 the first experimental data were taken. It was designed to achieve an initial goal of producing a continuous electron beam up to 4 GeV, sufficient enough to probe the nucleus and study the structure and underlying fundamental forces down to the quark level [32]. Although, we did not require spin-polarized beams for our current purpose, CEBAF is capable of producing an electron beam with spin polarization greater than 75%.

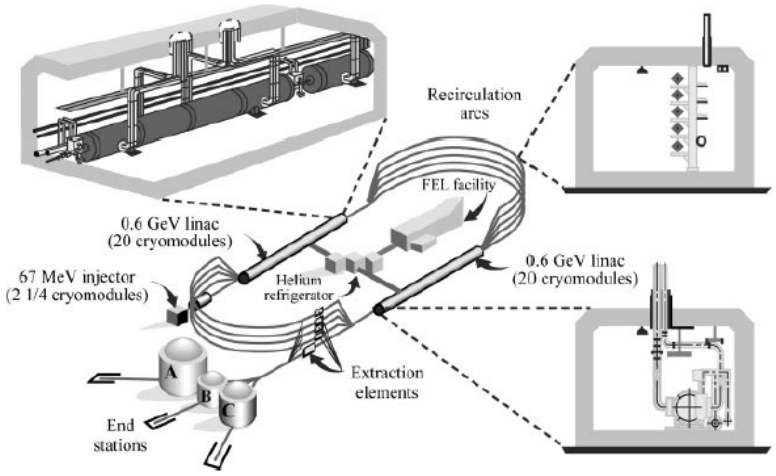

Fig. 2.1: Schematic of the CEBAF facility [33].

Figure 2.1 shows the layout of CEBAF. A strained gallium arsenide (GaAs) su-

perlattice photocathode is used to produce electrons at the injector and the beam current produced by this stream of electrons can be up to 200 μA. The GaAs superlattice has a remarkably high quantum efficiency that enables one to produce a large number of photo-electrons when illuminated with light of 780 nm wavelength from a 1497 MHz gain switched laser diode [32, 34]. The electrons so produced are then injected into the north linac after being accelerated to 45 MeV at the injector.

The CEBAF accelerator consists of two sets of niobium superconducting radio frequency (SRF) linear accelerators (Linacs) which are joined by recirculating arcs. The beam is accelerated in these two linacs (north and south) and each linac has 20 cyromodules. Each of these cyromodules contains 8 SRF cavities that are cooled to 2K by liquid helium. The accelerating gradient in the linac is around 7 MeV/m and the electrons can be accelerated up to 600 MeV before entering the recirculating arc that allows the electrons to be accelerated again. The design of the accelerator ensures that the electrons may pass through the linacs up to five times [33], resulting in a maximum attainable beam energy of 6 GeV, past the design goal of 4 GeV. After each of the first four passes through the accelerator, a beam of a particular energy can be delivered to only one of the three Halls A,B, or C. On the other hand, the final (fifth) pass can be delivered simultaneously to all three halls.

These recirculating arcs consist of a series of dipole magnets that steer the electron beam with one dipole at the start to spread out the beam into different energies and one at the end for recombining the beams [33, 35]. Electrons with lower energy are steered to the higher arcs since they can be easily handled while the higher energy electrons stay in the lower arcs. The dipole at the end is then utilized to recombine beams of different energies, which can then again be passed through the linacs.

2.2 Hall A overview

Among the three experimental Halls, Hall A is the largest with a diameter of 53 m and height of 20 m. Two High Resolution Spectrometers (HRS) are the most important devices installed in Hall A. The structural design of these two spectrometers is identical, and each can detect charged particles of a desired momentum with a resolution of 4.5%. The lay-out of Hall A is shown in Fig.2.2.

Several other elements are used in Hall A to transport the beam onto the target and measure energy, current, position of the beam, and the beam polarization before the beam hits the target. The targets are placed in a vacuum chamber made out of aluminum, which is also known as the scattering chamber. After hitting the target, the electrons scatter via electromagnetic interactions. The HRS detector systems then detect these scattered electrons and recoiling hadrons. The electrons that do not interact with the target are transported in a beam pipe and eventually stopped at the beam dump. In this experiment, both spectrometers detected electrons.The position of the Left HRS (LHRS) was changed according to the kinematic settings while the Right HRS (RHRS) was fixed at 24° for calibration purposes. The HRS systems are discussed in section 2.4.

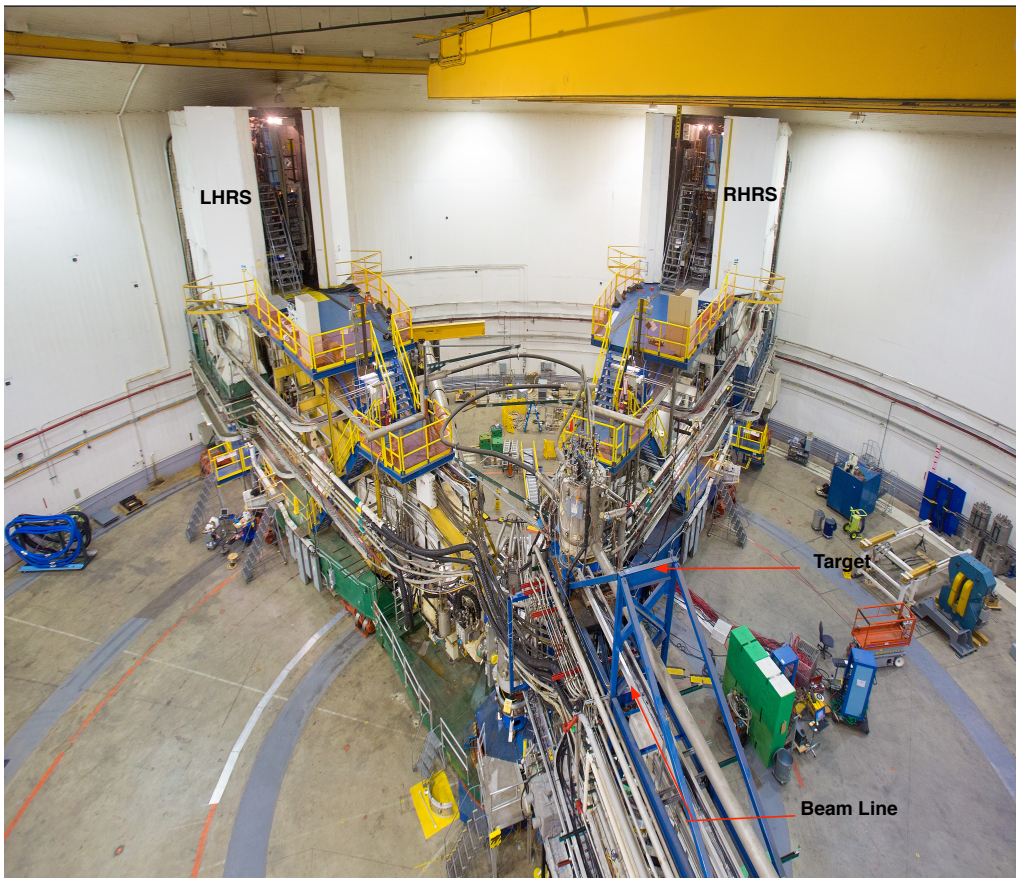

Fig. 2.2: Lay-out of Hall A. [36]

2.3 Hall A Beamline

2.3.1 Beam Energy Measurement

It is well known that the circular trajectory of an electron moving in a magnetic field depends on the strength of the magnetic field and the momentum of the electron. Conversely, we can say that the electron's momentum can be determined by measuring the arc through which the electron is deflected in a known magnetic field. This is the basic technique by which the arc method determines the energy of the beamline.

As shown in Fig. 2.3, the arc method, also known as the Tiefenbach method, measures the deflection of the beam in the arc section of the beam line. There are

eight dipoles in the line and the nominal bend angle of the beam in this section is 34.3° [31, 32]. The momentum of the beam can be calculated from the magnetic field in the dipoles and the resulting bend angle using the relation

$$p = k\frac{\int \vec{B}.d\vec{l}}{\theta}, \tag{2.1}$$

where $k = 0.299792\text{GeV} \cdot \text{rad} \cdot \text{T}^{-1} \cdot \text{m}^{-1}/c$ [32]. Two measurements are taken simultaneously to find the beam energy; the integral of the eight dipoles in the arc is measured using a 9th identical dipole (reference magnet) and the actual bend angle of the arc using a set of wire scanners.

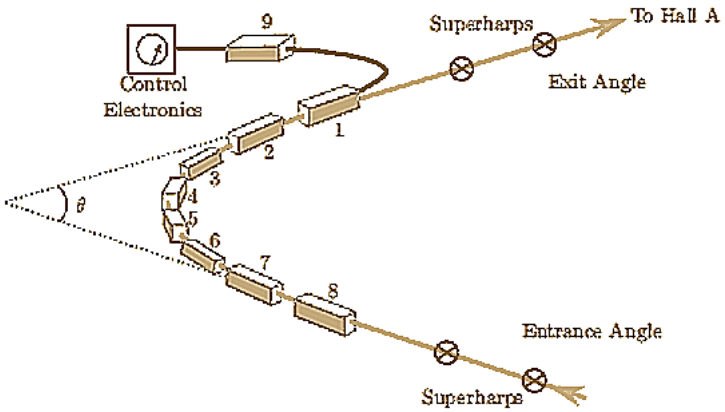

Fig. 2.3: The arc beamline section [35].

At JLab the energy of the beam can be measured by another independent method, the e-P method [32], which useds the $^1\text{H}(e, eP)$ elastic-scattering reaction. Knowing the scattered electron angle θ_e and the recoil angle of proton θ_p, the beam energy can be estimated via the following equation:

$$E = M_p\frac{\cos(\theta_e) + \sin(\theta_e)/\tan(\theta_p) - 1}{1 - \cos(\theta_p)} + O(m_e^2/E^2), \tag{2.2}$$

where M_p is the mass of the proton and m_e is the mass of the electron . The schematic diagram of the e-P system is shown in the Fig.2.4. Polyethylene (CH_2) is used as a

target about 17 m upstream from the Hall A pivot. Two sets of detectors are placed symmetrically about the beam axis. The proton detector is fixed at a particular angle with respect to the beam line while the electron detectors are varied in a range of angles that correspond to an incident energy range of 0.5 to 6.0 GeV. There are two scintillator planes and a silicon micro-strip detector in the proton detector. In the other HRS assembly, the electron detector has silicon strip detectors (SSD), a scintillator plane and a Cherenkov detector.

Both methods provide results in excellent agreement, with a very small net uncertainty of 0.03% [31].

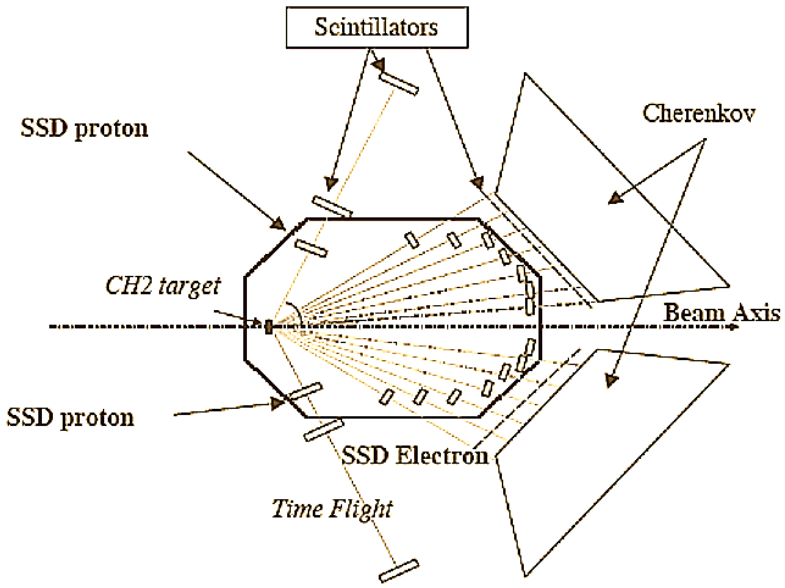

Fig. 2.4: Components of the e-P energy measurement system [32].

2.3.2 Beam Current Monitors

The Beam Current Monitors (BCM) in Hall A measure a very steady, low-noise and non-invasive beam current and are located 25 m upstream of the target [32]. The BCM consists of a parametric current transformer or an unser monitor and two RF Cavities. The calibration of the unser monitor is performed by passing a known

current through an internal wire and consequently provides an absolute reference. The RF cavities are stainless steel cylindrical high- Q waveguides that are placed on both sides of the Unser monitor and are tuned to the frequency of the beam resulting in output voltages proportional to the beam current.

The RF output is split in two, one of which goes to an AC voltmeter that gives an average beam current measurement every second. The other part of the RF signal passes through an analog- to -digital (ADC) converter followed by a voltage to frequency converter and this is counted by VME scalers during every run; providing a measurement of the total charge accumulation in a particular experimental run.

The linearity of the RMS to DC converter is preserved to within 1% for currents from 10 μA to 200 μA [31]. In order to include lower currents in this linear range, two additional amplifiers of gains 3 and 10 are added to the system [32, 35]. Thus, each BCM produces three signals that are counted by scalers in both of the HRS systems to produce an output 12 times redundant for measuring the charge in a physics run.

The LEDEX experiment, due to its nature, sometimes had very low currents. Currents as low as 1 μA were required and therefore a beam silver calorimeter was used for the calibration instead of the Unser monitor at these low current settings. This calorimeter is very reliable from a few micro amperes down to a few hundred nano amperes. In a typical calibration run, the beam enters the calorimeter and transfers its energy to the "slug" and, as a result, the temperature of the slug increases. From the temperature change, or from the amount of heat energy transfer, the beam current can be estimated to within 0.5% uncertainty [31]. A schematic of the silver calorimeter is shown in Fig.2.6.

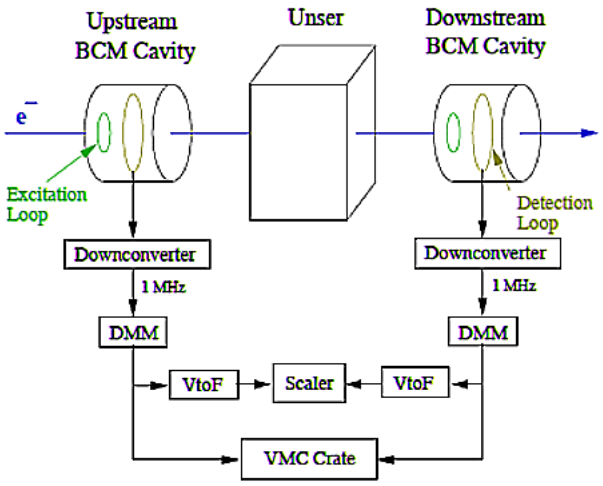

Fig. 2.5: Beam Current Monitoring System.

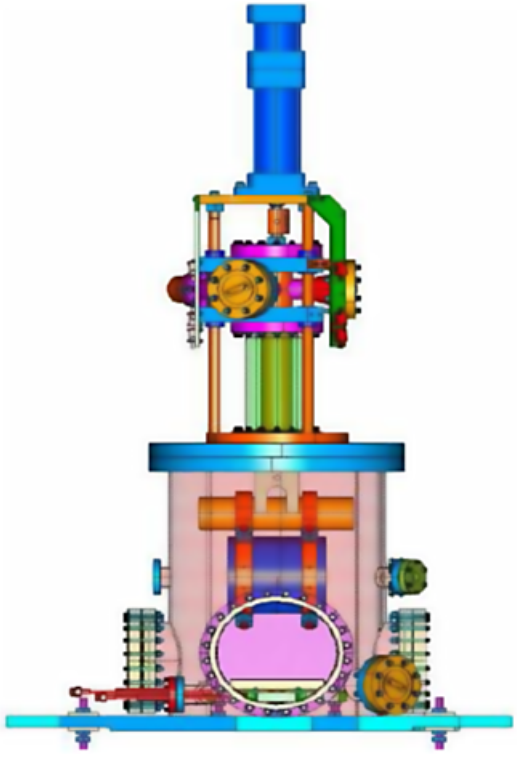

Fig. 2.6: Silver Calorimeter.

2.3.3 Beam Position Monitors

The position and direction of the beam were determined by using two Beam Position Monitors (BPMs) placed 7.524 m and 1.286 m upstream of the target [32]. Each BPM consists of a 4-wire antenna array in a cylindrical cavity parallel to the central axis of the beam. When an electron passes through the cavity, signals are generated in the wires [35]. The amplitudes of the signals are inversely proportional to the distance between the wire and the beam. The position of the beam in two dimensions can be found by combining the signals from a pair of wires.

Calibration of the BPM is obtained through the use of two superharp wire scanners. The superharps have three wires oriented vertically at $\pm 45^{\circ}$ and positioned adjacent to each BPM. The calibration is done by performing a bulls-eye scan, putting the beam at a known location. It gives the absolute positions of the wire scanners and, consequently, the absolute beam position is determined.

When the event rate is too high (e.g., with liquid targets) the BPMs are not good enough to trace the positions of each and every event [31]. In these situations a "raster" is used to sweep the beam electromagnetically in a pattern on the target in order to prevent overheating in one spot. The raster raw current, a measure of the position and direction of the raster, which is related to the beam position by a linear equation, can be used. The calibration is done by comparing the raster raw current with the beam average position from the BPM and consequently the rastered beam position of each event is extracted.

2.4 High Resolution Spectrometers

The two identical high resolution spectometers in Hall A were designed to study nuclear structure through the $(e, e'p)$ reaction. Their main characteristics are tabulated

in Table 2.1 [32].

Each HRS contains three quadrupoles and a dipole arranged sequentially (QQDQ) as illustrated in Fig.2.7. All the magnets are superconducting and are cryogenically cooled. The Quadrupoles Q1 and Q2 focus the scattered particles (i.e., produce a parallel beam). The dipole steers the charged particles to produce a 45° bend angle for the central ray and also creates a net focusing effect at its entrance and exit. The final quadrupole Q3 allows one to achieve the desired horizontal position and angular resolution.

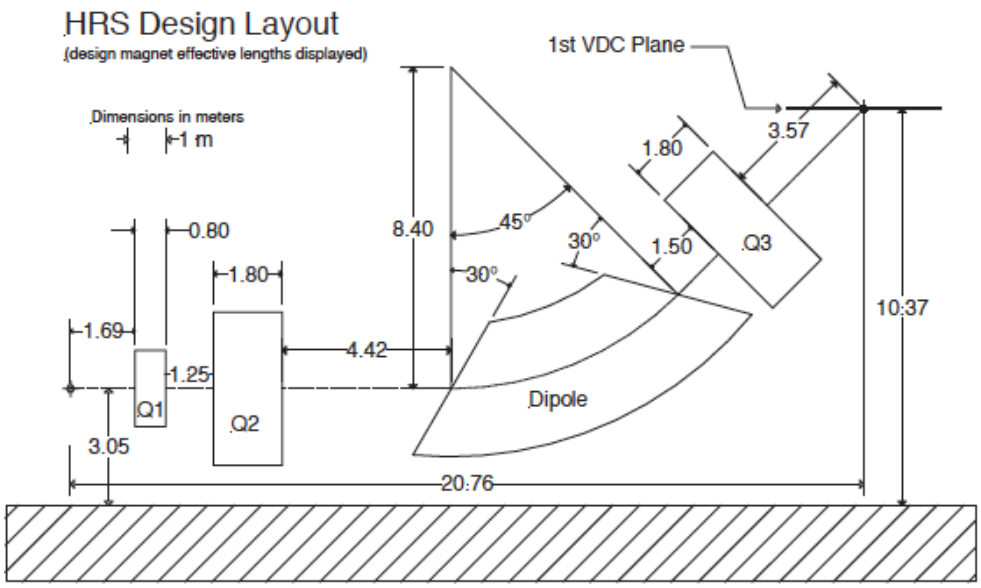

Fig. 2.7: Geometrical configuration of the HRS [32].

Table 2.1: Characteristics of the Hall A HRS [32].

Configuration	QQDQ
Bend Angle	45°
Optical Length	23.4 m
Momentum Range	0.3-4.0 Gev/c
Momentum Acceptance	$-4.5\% < \delta p/p < +4.5\%$
Momentum resolution	1×10^{-4}
Dispersion at the focus	12.4 m
Radial linear Magnification	-2.5
D/M	5.0
Angular range	
LHRS	$12.5 - 150°$
RHRS	$12.5 - 130°$
Angular acceptance	
Horizontal	±30 mrad
Vertical	±60 mrad
Angular resolution	
Horizontal	0.5 mrad
Vertical	1.0 mrad
Solid angle, $\Delta\Omega$	$\sim$ 6 msr
Transverse length Acceptance	±5 cm
Transverse Position resolution	1 mm

2.5 The Detector package

The polarities of the magnets and the detectors can be customized in such a way that they may be used for detecting either negatively or positively charged particles. The detectors are placed inside shielded huts (SH) at the top of each HRS that block the background radiation from all directions. Figure 2.8 shows a side view of the detector stack. Both detectors contain a pair of vertical drift chambers (VDC) at the front that determines the trajectory of the scattered electrons. At the back, there are scintillators, Cherenkov detectors, and pion rejectors. The scintillator produces a trigger for the VDC detector while the other detectors do the job of particle identification (PID) and can be removed or introduced easily depending on the requirements of a particular experiment [37, 38].

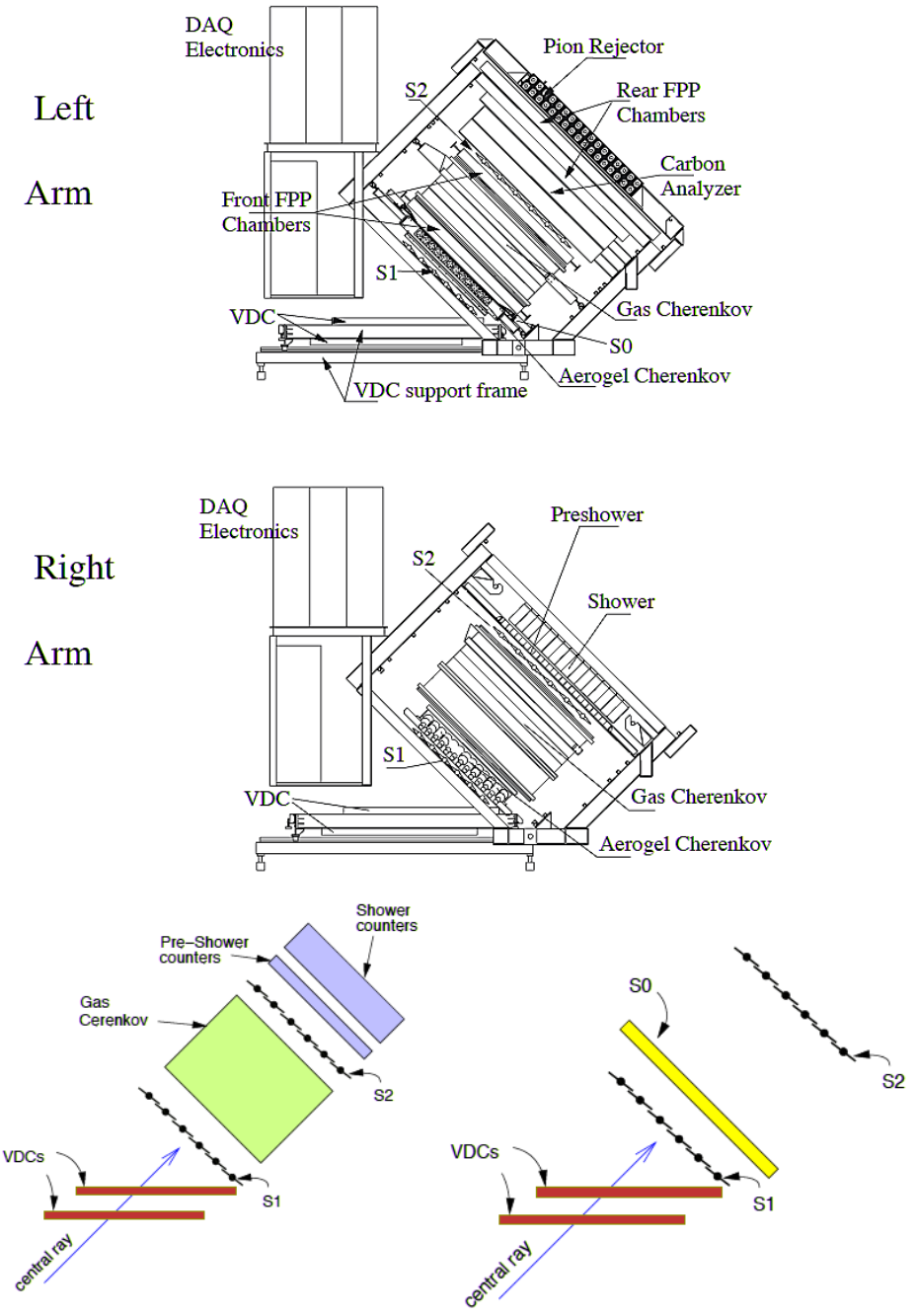

Fig. 2.8: Sideview of the detector stack [32, 38]. First/Second part of the third picture is for the LHRS/RHRS.

2.5.1 The Vertical Drift Chambers

Each of the detector packages has two VDCs with two wire planes in a typical UV configuration, as shown in Fig. 2.9. These two planes are parallel, separated by 23 cm and oriented at 45° to the central ray [38]. Each plane consists of 368 gold-plated tungsten wires, each with diameter 20 μm. The wires are placed 90° with respect to one another and 45° to the projection of the central ray onto the wire planes [32,39].

An electric field is generated by keeping the gold-plated Mylar planes at ~ -4 kV and the wires to ground; this causes the electrons to accelerate towards the wires (Fig. 2.10). The chambers are filled with gaseous argon and ethane in a 62 : 38 ratio. The argon makes the environment suitable for ionization while ethane absorbs the photons created during a ionization event. As the electrons are accelerated towards the wires, due to the potential gradient, they multiply their number by ionizing the gas, which ultimately leads to an electron avalanche. This avalanche produces a detectable electrical signal called a hit, which is then sent to a time-to-drift digital converter (TDC) after being pre-amplified.

The drift times of electrons from the original trajectory are measured by a TDC. This timing information is then converted to distance from the wire to the trajectory. The trajectory can be constructed by combining the drift distances measured by all the wires that have been hit. To improve the resolution, information from all four wire planes in each VDC pair is then combined. The resulting position and angular resolution in the focal plane are ~ 100 μm and ~ 0.5 mrad, respectively [37].

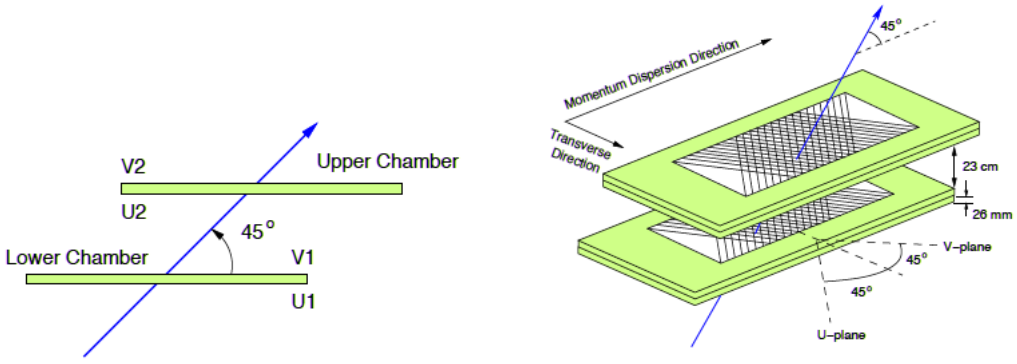

Fig. 2.9: Schematic diagram of the Hall A vertical drift chambers [38].

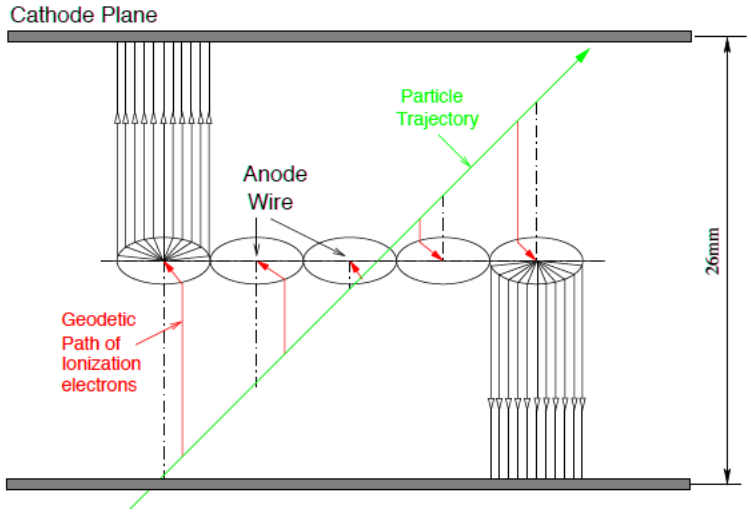

Fig. 2.10: A typical particle trajectory through the VDC. Here the five closest wires are shown to register a hit. Electrons drift along the geodetic path - the path that takes the shortest time and induces a signal in the wires [38, 39].

2.5.2 The Scintillators

Both the LHRS and the RHRS contain two planes of plastic scintillators S1 and S2, separated by 2m which form the principal trigger system for events and provide time-of-flight information (TOF) between the two arms. Each plane has six 5mm thick paddles [32]. Plane S1 has an active area of 170×35 cm^2 while S2 measures 220×54 cm^2. The ends of the paddles are viewed by two photomultiplier tubes (PMTs) with

a time resolution of about 0.3 ns [37]. The scintillator plane S0 is found only in the right HRS. It is placed behind S1 and has only one paddle of active area of 190×40 cm^2 with a 3 inch photomultiplier tubes (PMTs) at each end. The scintillators are placed perpendicular to the central ray, that is, at an angle 45° to the vertical (Fig. 2.11).

When the scattered electrons enter a paddle they ionize the material of the paddle. These secondary electrons produced through the ionization have lesser energies and cause molecular excitations inside the paddle. The excited molecules go back to their normal state quickly giving away their energy in the form of photons which are then collected by the PMTs at the ends. A detailed discussion of the different types of triggers formed from the signals will be made later (Sec. 3.7).

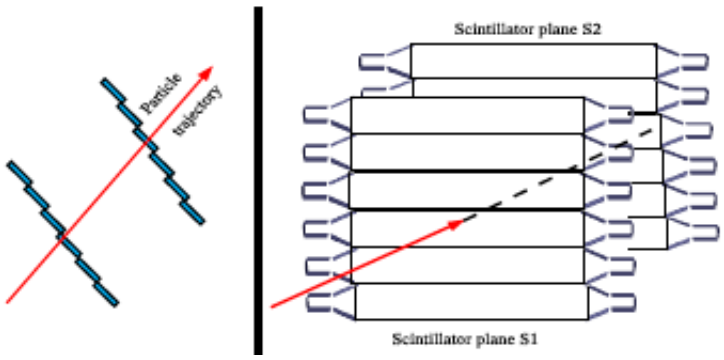

Fig. 2.11: Layout of a scintillator detector.

2.5.3 Cherenkov Detector

The gas Cherenkov detector is full of CO_2 at atmospheric pressure and is mounted between the S1 and S2 scintillators. The detector operation is based on identifying the Cherenkov light that occurs when charged particles in a dielectric medium travel faster than the phase velocity of light in that medium. Since pions are many times heavier than electrons and the Cherenkov radiation threshold is proportional to the

mass of the particle, Cherenkov light is very effective in distinguishing the electron and pion events.

The relationship between the threshold momentum of a particle of mass m in a medium whose refractive index is η is [37]

$$p_{ch} = \frac{m}{\sqrt{\eta^2 - 1}}. \tag{2.3}$$

The CO_2 inside the Cherenkov detector has a refractive index of 1.0004. Using the relation above we find the electron's Cherenkov threshold momentum is around 18 MeV, which is very low compared to that of the energy of the pions, 4.8 GeV. In this experiment, the maximum momentum for the scattered electrons were only 685 MeV so electron events could be easily separated from pion events.

There are 10 spherical mirrors in the detector, each of which directs emitted Cherenkov light to the PMTs. These light signals are then fed to an ADC and summed. This provides a measure of the amount of light produced by the particles.

2.5.4 Preshower-Shower Counters

Pair production and bremsstrahlung radiation are the two key ingredients of the preshower-shower counters. High-energy charged particles travelling inside a dense material decelerate and hence produce photons and electron-positron pairs. The pair annihilation can occur again and produce photons, and the process repeats again and again resulting in a cascade of photons that can be detected by a PMT.

The relationship between the light output from the shower and energy deposited by the incident particle is linear, which permits particle identification to be determined from the distribution of energy in the counter. Two planes of lead glass blocks compose the counters, which are referred to as the preshower and the shower counters. There are 48 lead glass blocks in the preshower with a dimension of $10 \times 10 \times 35\text{cm}^3$.

The shower counter, which is placed behind the preshower detector, consists of 80 blocks with a dimension $14.5 \times 14.5 \times 35\text{cm}^3$ (Fig.2.12).

The shower detectors are mounted at different orientations in two arms. The resolution of the right arm is better because the shower detector has a larger thickness than in left arm. The particle identification parameter, R_{sh} is defined as

$$R_{sh} = \frac{E_{\text{tot}}}{p} \times \frac{ln(E_{\text{presh}})}{ln(E_{\text{ave}})}.$$

where E_{tot} is the total energy deposited in the shower detector, p is the momentum of the particle, E_{presh}) is the energy deposited in the preshower detector and E_{ave} is the average energy deposited by an electron with momentum p. For momenta above 2 GeV, the pion supression efficiency is found to be 98%.

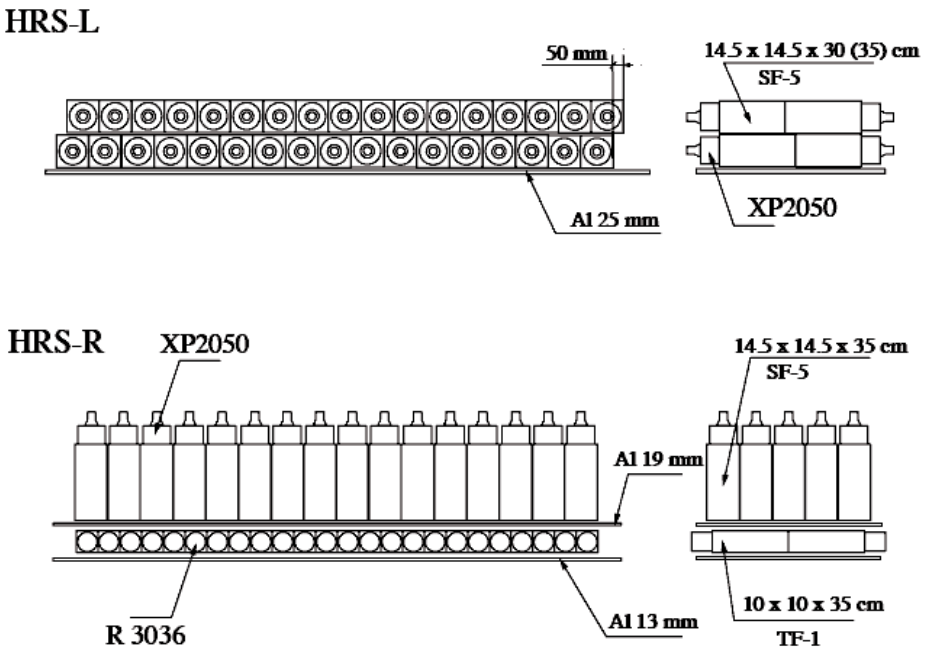

Fig. 2.12: Schematics diagram for the shower and preshower lead glass blocks used in the RHRS/LHRS [32]. These electromagnetic calorimeters were used to separate electrons from pions.

2.6 Targets

Hall A targets are contained in a stainless steel scattering chamber in a vertical assembly holding liquid cells and solid foils. This target ladder system is remotely controlled in the vertical direction to intersect any of the targets with the beam. There are three independent cryogenic target loops of liquid hydrogen (LH_2), liquid deuterium(LD_2) and gaseous deuterium. The fluids in loop 1 and 3 are changed as requested. The liquid cells are made out of aluminum and come with two different lengths, 4 cm and 10 cm. Each has a radius of curvature of 2 cm at the end. Figure 2.13 are pictures of the liquid target system and solid targets. Details of each target can be found in [32, 40].

Pressure transducers and thermal gauges were used at various positions to monitor the environment of the liquid target systems, and densities were maintained with an uncertainty of less than 0.1%. LH_2 was operated at 19K and 0.17 MPa and LD_2 was operated at 22 K and 0.15 MPa with 0.0723 g/cm^3 and 0.167 g/cm^3, respectively for densities [31]. ^{4}He and ^{3}He were kept at the same temperature (6.3 K) but at slightly different pressures, 1.4 MPa for ^{4}He and 1.1 MPa for ^{3}He. Dummy targets made of aluminum were also used to estimate the contributions from the cell windows. They were lined up aluminum planes separated by a distance of 4 cm, 10 cm, and 15 cm to match up with the liquid target cells.

Table 2.2: Cryogenic target window thickness

Target	Entrance Window ($\pm$ 0.005) (mm)	Exit Window ($\pm$ 0.005) (mm)
Loop 1 4 cm	0.127	0.149
Loop 1 10 cm	0.207	0 .230
Loop 2 4 cm	0.127	0.113
Loop 2 15 cm	0.118	0 .040
Loop 3 4 cm	0.112	0.140
Loop 3 10 cm	0.256	0 .236

A pure boron target was used in an earlier experiment at NIKHEF, but proved to be very unstable. In this experiment a compound B_4C was used instead, which is many times stronger than pure boron and is very stable against beam heating. There was also a ^{6}Li solid target. As lithium is very reactive, especially with oxygen, it was immersed in olive oil and put in the target chamber. Then, the olive oil was vacuumed off by the vacuum of the chamber.

A list of solid targets used during this experiment is tabulated with their properties in Table 2.3. The temperatures of the solid targets were maintained by the loop 2 heat exchanger.

Table 2.3: Solid target ladder

Target (Solid)	Purity (%)	Density (gm/cm^3)	Thickness (gm/cm^2)
BeO	99.00	—	0.149 ± 0.001
Ta	99.50	16.69	0.0202 ± 0.00005
C	99.95	2.26	0.083 ± 0.0001
B_4C	97.27	2.52	0.467 ± 0.00026
^6Li	95.24	0.53	0.244 ± 0.010
Slanted C	99.5	—	0.111 ± 0.010
Slanted Fe	99.5	—	0.119 ± 0.010

2.7 Data Acquisition (DAQ)

The CEBAF online data acquisition system (CODA) collects all the data during an experiment. CODA is equipped with necessary software to take raw data from the ADC, TDC, and scaler modules, build events from the information of the interactions, and record them. As mentioned earlier, amplified raw signals from the detectors are input to ADCs and TDCs. If a signal from the detector satisfies the trigger condition, the trigger supervisor opens the gate for recording it.

The Read-out Controllers (ROC), an integral part of CODA, collected the data from the ADCs and TDCs. The CODA Event Builder then constructed a single data structure by sewing together the pieces of scattering information from the ROCs. The event recorder then wrote these data to a local disk and eventually transferred the data to a Mass Storage System (MSS) to store for a long term. Information, such as, beam current, charge, positions, etc. were also sent downstream at regular intervals. A C^{++} based Hall A analyzer is the proper tool for decoding these data, which is built on top of the ROOT libraries from CERN. The analyzer produced the

necessary "ntuples" that can give diagnostic information and physics results.

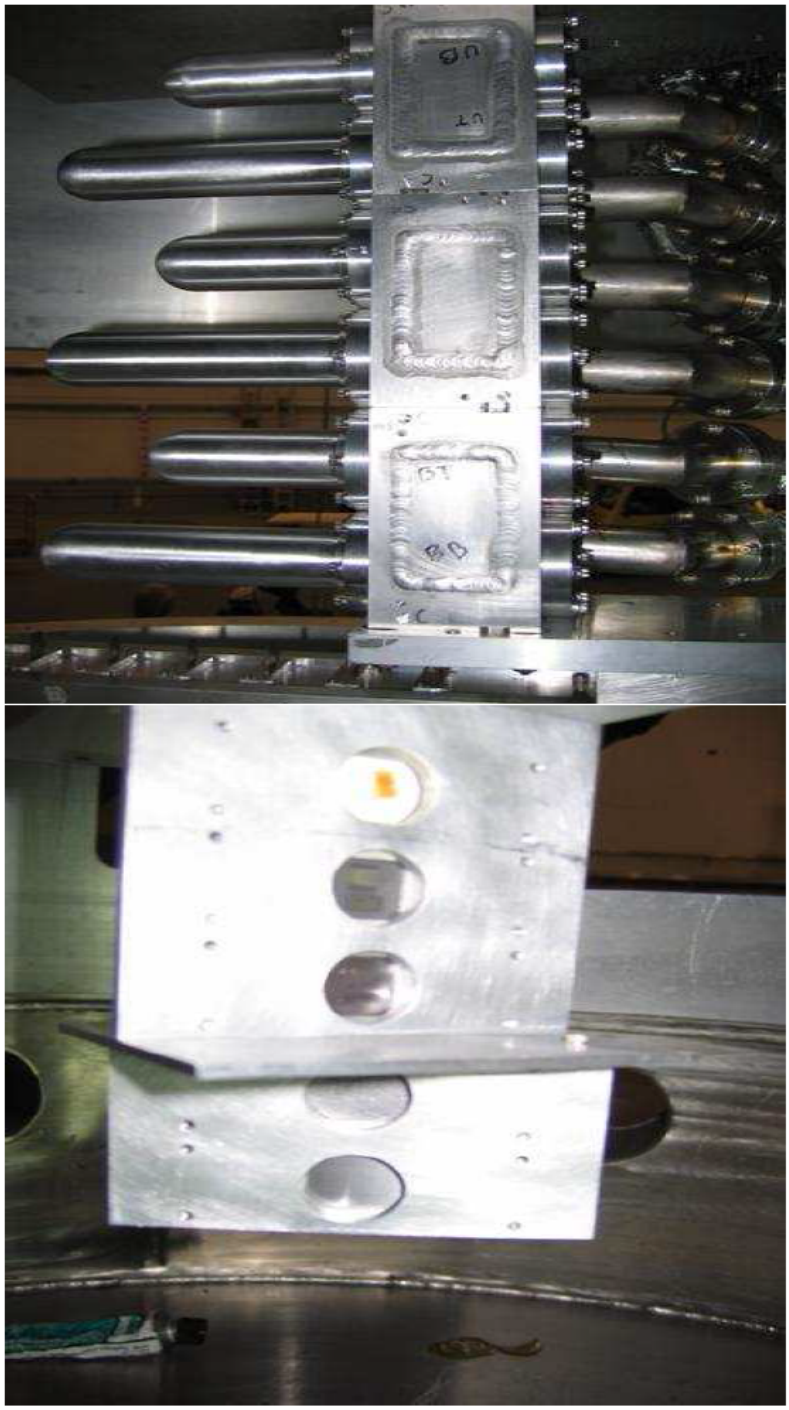

Fig. 2.13: LEDEX targets. The top panel shows liquid targets and the bottom panel shows solid targets [40].

Chapter 3

DATA ANALYSIS

In this chapter, we will discuss two important steps, spectrometer optics calibration and determination of efficiencies of various components of the experimental set up, and will emphasize their roles in the analysis procedure.

3.1 Optics Calibration

3.1.1 Coordinate system

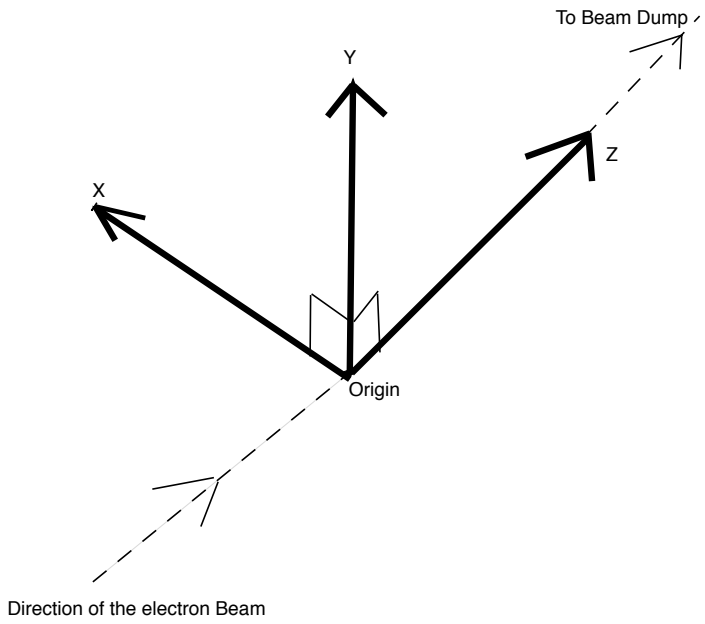

Fig. 3.1: Hall A coordinate system [31].

Figure 3.1 shows the coordinate system of Hall A, as viewed from above. The center of the hall is defined as the origin and the z-axis is along the direction of the electron beam. The y-axis points vertically upward and the x-axis is directed towards the

left of the beam direction. This forms the standard reference for all other coordiante systems.

3.1.2 Target Coordinate system

The orientaion of the z -axis (z_{tg}) in this coordinate system is perpendicular to the sieve plate of the spectrometer. The direction of x_{tg} , y_{tg} , and z_{tg}, in and out of plane angles is illustrated in Fig. 3.2 and 3.3.

The definition of in-plane and out-of-plane angles can be given as

$$\tan\theta_{tg} = \frac{dx}{dz},$$
$$\tan\phi_{tg} = \frac{dy}{dz}.$$

The central momentum of the spectrometer (p_0) is related to another target coordinate, δ_{tg}, or the deviation of momentum from the particle's central momentum by [41]

$$\delta_{tg} = \frac{p - p_0}{p_0}.$$

3.1.3 The Detector Coordinate System

The origin of this coordinate system is the intersection point between two lines drawn on VDC1, one is a perpendicular line on the 184^{th} wire of the U1 plane, and the other is the perpendicular projection of the 184^{th} wire of the V1 plane into the U1 plane (Fig. 3.4). The Z-axis (Z_{det}) is directed perpendicular to the wire planes in the VDCs, while the X and Y axes are directed to the long and the short symmetry axis of the VDCs, respectively [41] [38].

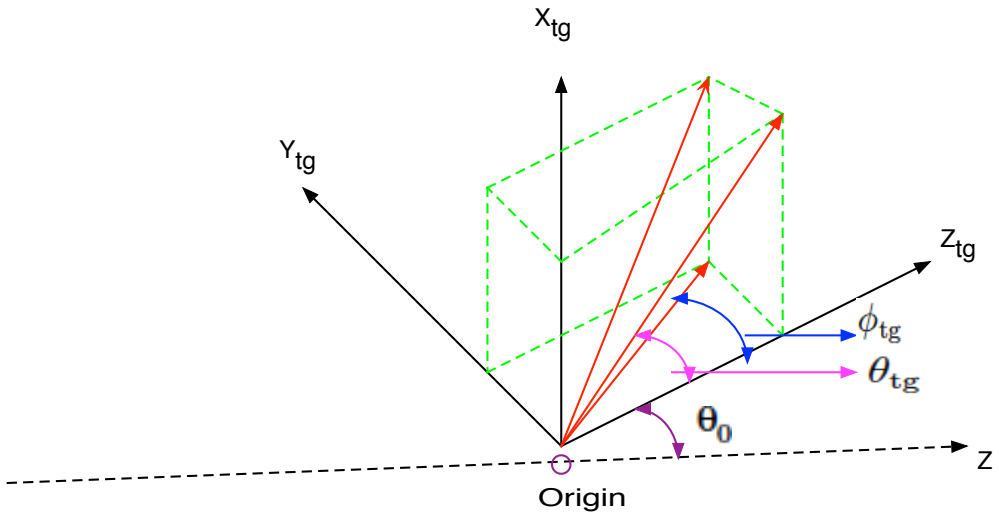

Fig. 3.2: Target Coordinate System [31].

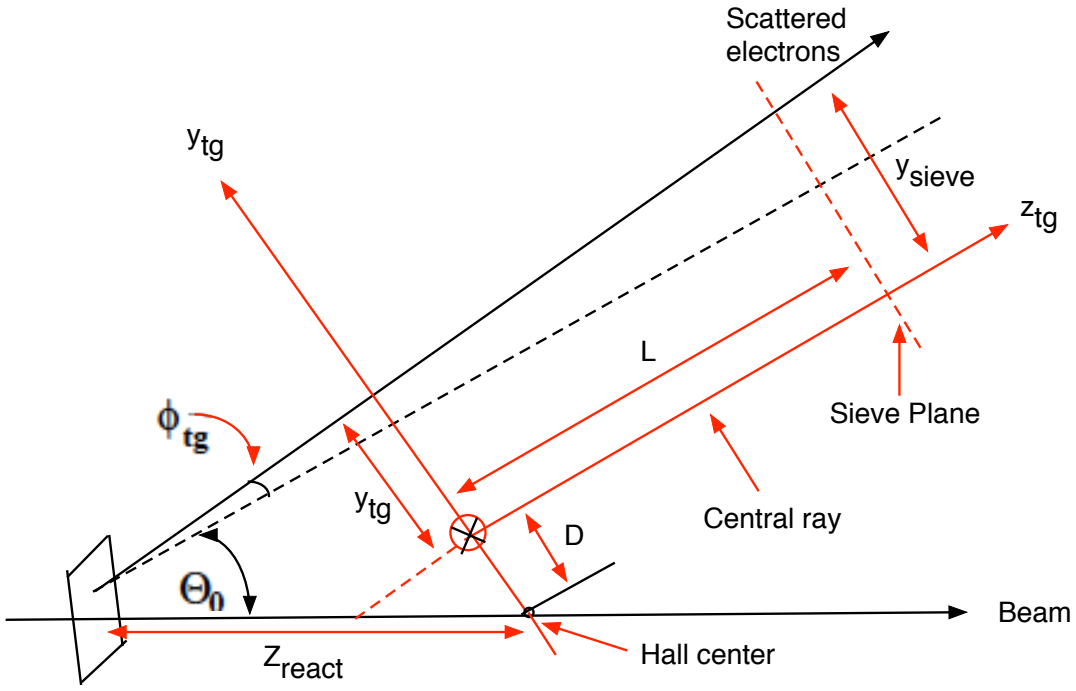

Fig. 3.3: Target Coordinate System [32].

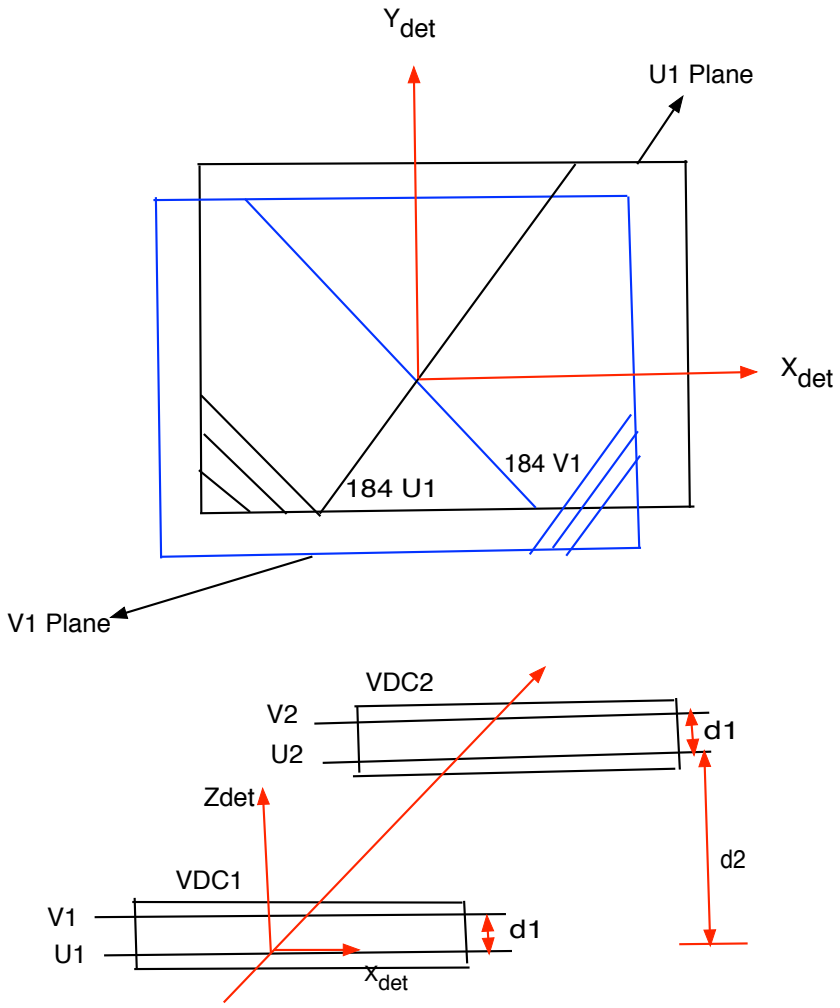

Fig. 3.4: Detector coordinate System [32].

3.1.4 Focal Plane Coordinate System

This is a rotated coordinate system, which is obtained by rotating the detector coordinate system around its Y axis by an angle ρ (Fig. 3.5), the angle between the central ray and Z_{det}. The central ray is the one that has $\theta_{tg} = \phi_{tg} = x_{tg} = y_{tg} = 0$, for the corresponding relative momentum δ_{tg}. The rotation makes the angle θ small at all points across the focal plane. This results in a faster convergence of the reconstructed vertex during the calibration process [41].

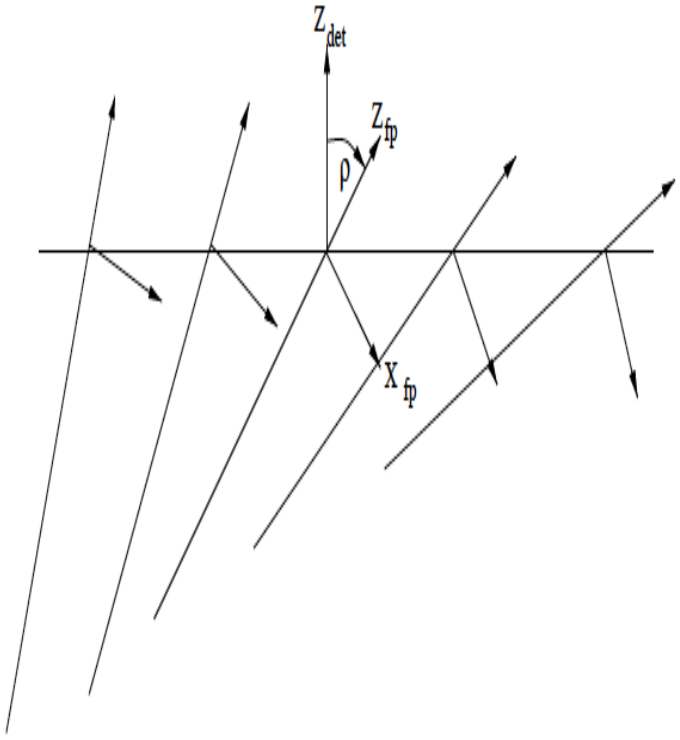

Fig. 3.5: Focal-plane coordinate system [41].

3.2 Optimization Approach

The focal plane and target coordinates are related via the following matrix equation:

$$\begin{bmatrix} x \\ \theta \\ y \\ \phi \end{bmatrix}_{tg} = \begin{bmatrix} \langle\delta|x\rangle & \langle\delta|\theta\rangle & 0 & 0 \\ \langle\theta|x\rangle & \langle\theta|\theta\rangle & 0 & 0 \\ 0 & 0 & \langle y|y\rangle & \langle y|\phi\rangle \\ 0 & 0 & \langle\phi|y\rangle & \langle\phi|\phi\rangle \end{bmatrix} \begin{bmatrix} x \\ \theta \\ y \\ \phi \end{bmatrix}_{fp} \tag{3.1}$$

There are 8 null components in the matrix equation above, which are so because of the mid-plane symmetry of the spectrometer. For each of the target variables, a

tensor exists, that limits it to the focal plane coordinates:

$$y_{tg} = \sum_{j,k,l} Y_{jkl}\theta_{fp}^{j} y_{fp}^{k} \phi_{fp}^{l}, \tag{3.2}$$

$$\theta_{tg} = \sum_{j,k,l} T_{jkl}\theta_{fp}^{j} y_{fp}^{k} \phi_{fp}^{l}, \tag{3.3}$$

$$\phi_{tg} = \sum_{j,k,l} P_{jkl}\theta_{fp}^{j} y_{fp}^{k} \phi_{fp}^{l}, \text{and} \tag{3.4}$$

$$\delta_{tg} = \sum_{j,k,l} D_{jkl}\theta_{fp}^{j} y_{fp}^{k} \phi_{fp}^{l}. \tag{3.5}$$

Again, from the symmetry considerations, $T_{jkl} = D_{jkl} = 0$ for odd $(k + l)$ and $Y_{jkl} = P_{jkl} = 0$ for even $(k + l)$.

The calibration can be simplified by using the reaction point along the beamline, Z_{react}, with the horizontal and vertical sieve slit positions, y_{sieve} and x_{sieve} [41]. These are hybrid variables, a mixture of some basic coordinates discussed in previous sections, and can be determined for a set of foil targets and sieve slits with the equations,

$$Z_{\text{react}} = -(y_{tg} + D)\frac{\cos(\phi_{tg})}{\sin(\theta_0 + \phi_{tg})} + x_{\text{beam}}\cot(\theta_0 + \phi_{tg}), \tag{3.6}$$

$$y_{\text{sieve}} = y_{tg} + L\tan\phi_{tg}, \tag{3.7}$$

$$x_{\text{sieve}} = y_{tg} + L\tan\theta_{tg}. \tag{3.8}$$

As shown in Fig. 3.3, L is the distance between the Hall A center to the sieve plane, D is the displacement of the central axis from its ideal location and θ_0 is the central angle setting of the spectrometer. The transfer tensor coefficients in the optics database $(T, D, Y, P)_{jkl}$ are calibrated by an analysis code that utilizes the χ^2 minimization of the aberration functions [41] [32] so that the events are reconstructed to the closest possible known position of the corresponding foil target or the sieve slit

hole.

$$\Delta(A) = \sum_i \left(\frac{A - A^0}{\sigma_A^i} \right)^2, \tag{3.9}$$

where, A represents the target coordinates. After the experimental survey, the nominal target positions (A^0) can be known, which are then put into comparison with the reconstructed events (A) in this procedure. The complete optimization procedure can be found in reference [41].

For this experiment, the optimization procedure was performed previously [31], and we inherited the optimized database files. However, we thoroughly checked the quality of the track reconstructions and optimizations at every kinematic setting (Figs. 3.6, 3.7, 3.8, 3.9).

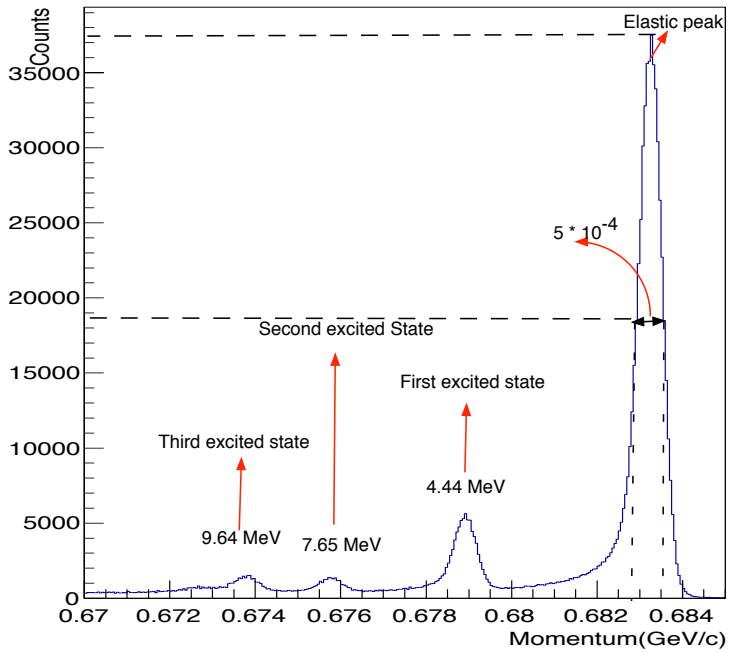

Fig. 3.6: The momentum distribution of the scattered electron in a $^{12}\mathrm{C}(e,e')$ reaction. The momentum resolution here is 5×10^{-4} (full width half maximum) at $\delta = 3\%$, for a beam energy of 685.266 MeV and at an angle of 17°, more than the design value of 1×10^{-4} [32]. The elastic and inelastic peaks are also shown, which are positioned exactly at the predicted points [30].

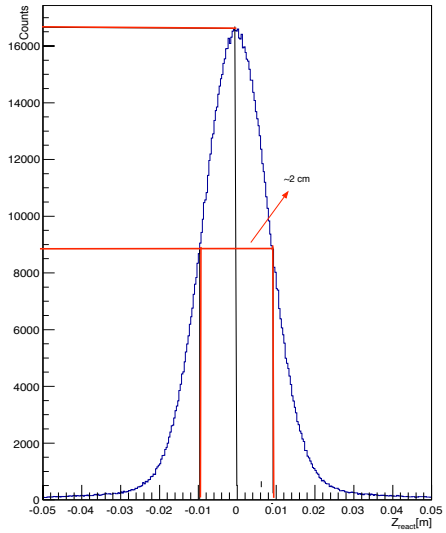

Fig. 3.7: Reconstructed position along the beam line for the same carbon run. The center of the target is at $Z_{\text{react}} = 0$ with a resolution of 2 cm, indicating a proper optical calibration.

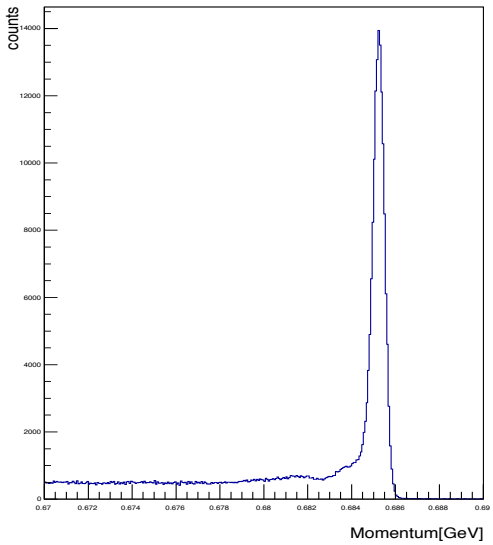

Fig. 3.8: The momentum distribution of the scattered electron in a Ta(e, e') reaction. The energy of the beam and angle of the spectrometer are the same as the carbon run (Fig. 3.6). Tantalum is a heavy nucleus and at this beam energy and angle there are no excited states, so that its elastic peak sits right at the momentum of the scattered electrons, which gives a reference for the measurement of the momentum.

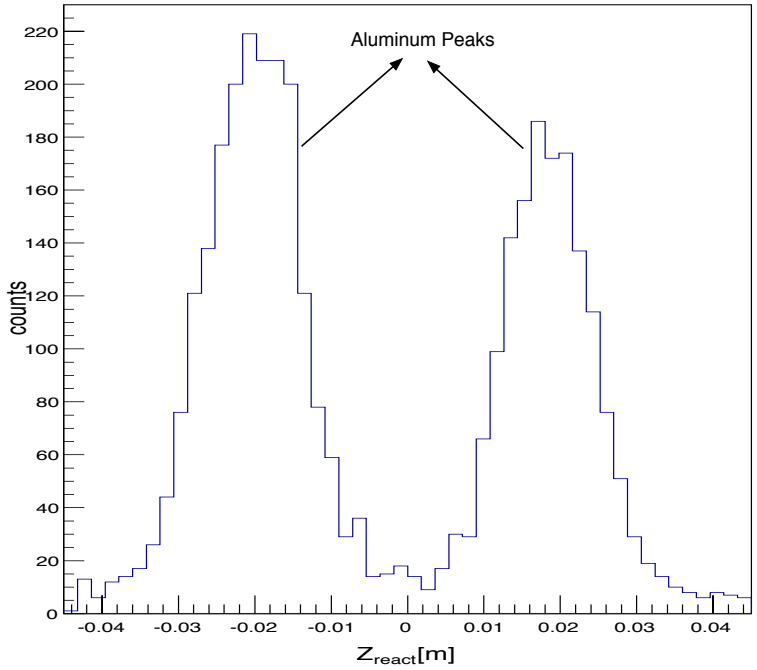

Fig. 3.9: Reconstructed position along the beam line for a 4 cm dummy cell. The cell is made out of aluminum, which gives rise to two distinctive peaks (back and front walls) with the desired resolution. It is further evidence of the proper optical calibration.

There is a 2 msr collimator added in the left arm. It has several pinholes around a large square hole at the center [Fig. 3.10]. The position of these pinholes can be known from the survey information, which in turn gives the position of the spectrometer. This is in fact a calibration check and an offset in the scattering angle is determined from this.

The top diagram of Fig. 3.16 shows the position of this collimator with sieve holes around it, which we found to be in exact agreement with the survey information.

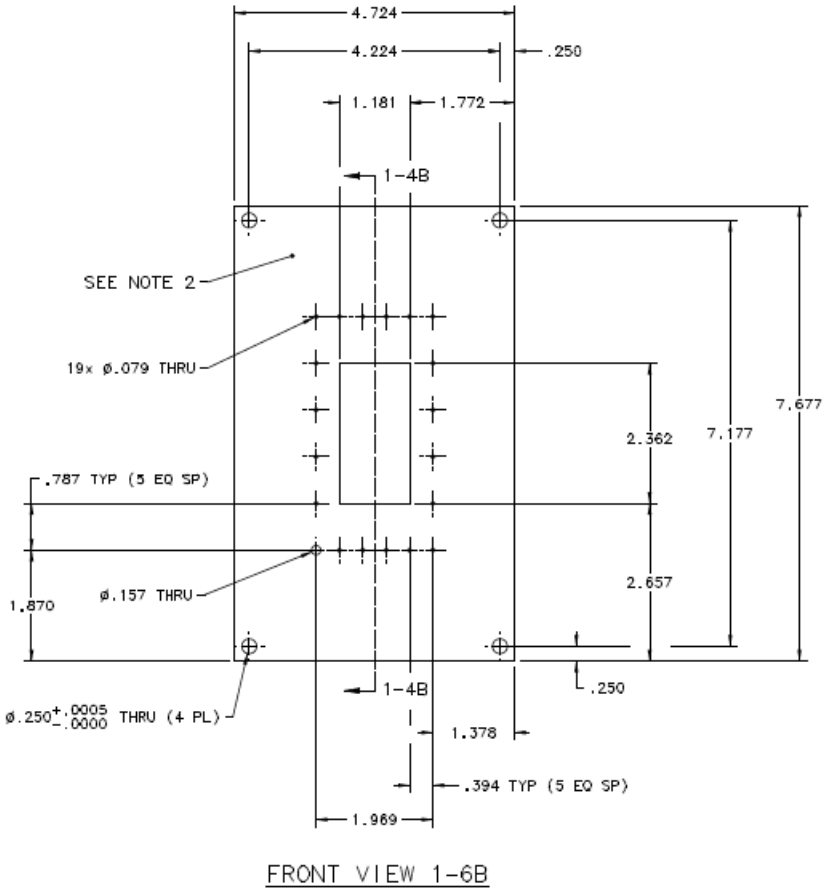

Fig. 3.10: Draft of the left-arm collimator.

3.3 BCM and BPM cuts

In this experiment there were runs where the beam was stopped momentarily. Because the target density (especially for cryogenic targets) is a function of the beam current, the target density uncertain for a long periods of time. Therefore, it is necessary to select stable beam regions for this kind of run by putting cuts on BCM and BPM.

During our study there were numerous runs for each angle of the spectrometer setting, so we were always able to find a run that was stable all the time [Fig. 3.11]. By only selecting the stable runs (continuous beam current and uniform distribution

of beam all the time) we avoided putting any cuts on BCM or BPM.

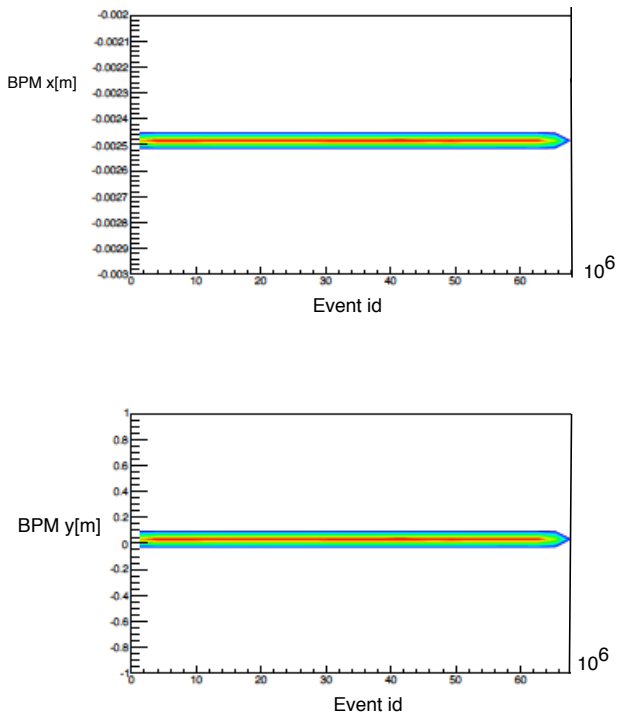

Fig. 3.11: Contour plot of BPM x and BPM y of a stable run

3.4 Cherenkov Sum Cut

The pions also can generate events, the majority of which can be eliminated by the gas Cherenkov particle identification (PID). The efficiency of the Cherenkov detector used in this experiment was more than 99.6% [31]. At least 4.8 Gev/c is required for a π^- to produce Cherenkov light in this detector. The maximum available beam energy during this experiment is only 0.686 GeV; hence, pion events should be negligible here, which we found to be true in all the runs we analyzed, especially at lower angles where the Cherenkov events were almost zero (Fig. 3.12, 3.13).

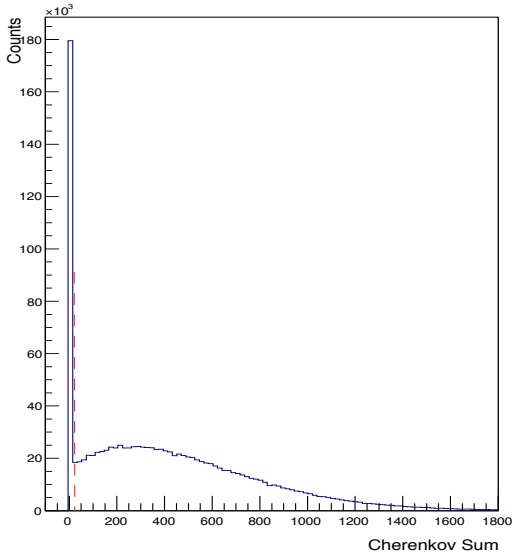

Fig. 3.12: A distribution from Chrenkov sum. The red line shows the position of the cut.

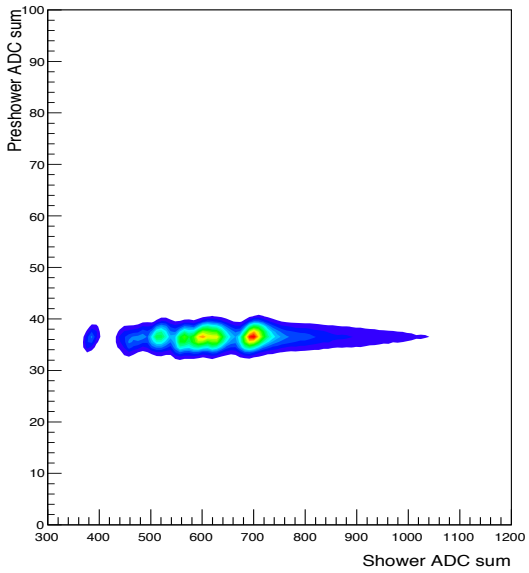

Fig. 3.13: A contour plot of the deposited energy on the shower and preshower counters. It shows the absence of pion events.

3.5 Good event cuts

Good events were obtained by applying good track cuts on vdc wire chambers. Abandoned events could be recovered at the time of cross-section calculations by introducing the tracking and triggering efficiencies.

"Good" track cuts means to consider events that have a single track, with one cluster per plane and numbers of hits between 3-6, and events from trigger 3(1) for the left(right) arm.

3.6 Acceptance cuts

It was observed that there were events present outside the physical acceptance of the spectrometer even with the calibrated data sets. These events were excluded by applying cuts on the geometry of the targets or on θ, ϕ, y_{tg}, and δ (Figs. 3.15, 3.16). The cuts were chosen to limit the data away from the region (edges of the acceptances) where the distribution of these parameters varies rapidly.

We found from a "white spectrum" study that the acceptance of the spectrometer is $\pm 3.9\%$ as shown in Fig. 3.14, which is lower than the expected value of $\pm 4.5\%$. A tight cut of $\pm 3.9\%$ was applied on the momentum acceptance during the yield calculations.

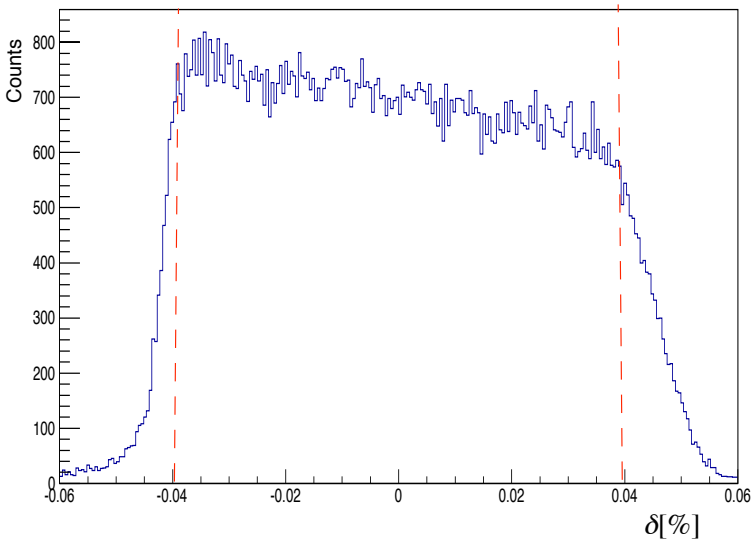

Fig. 3.14: δ distribution from a white spectrum. Momentum acceptance cuts are shown by the two red vertical lines.

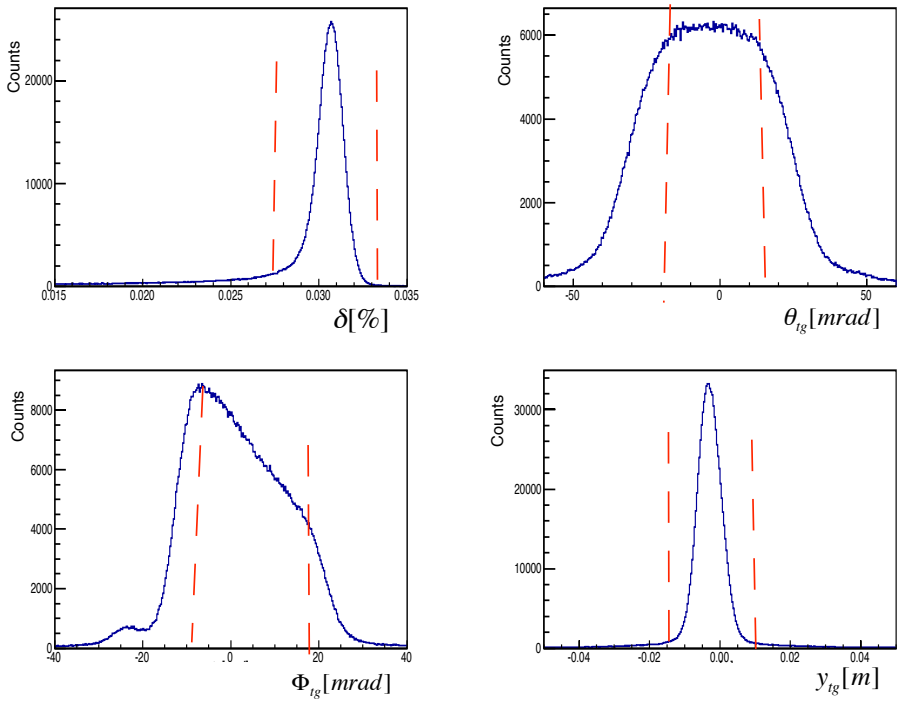

Fig. 3.15: Plot of the acceptance variables. The cuts are shown by the vertical red lines except for the lower cut on δ. This lower cut is for the selection of the elastic peak.

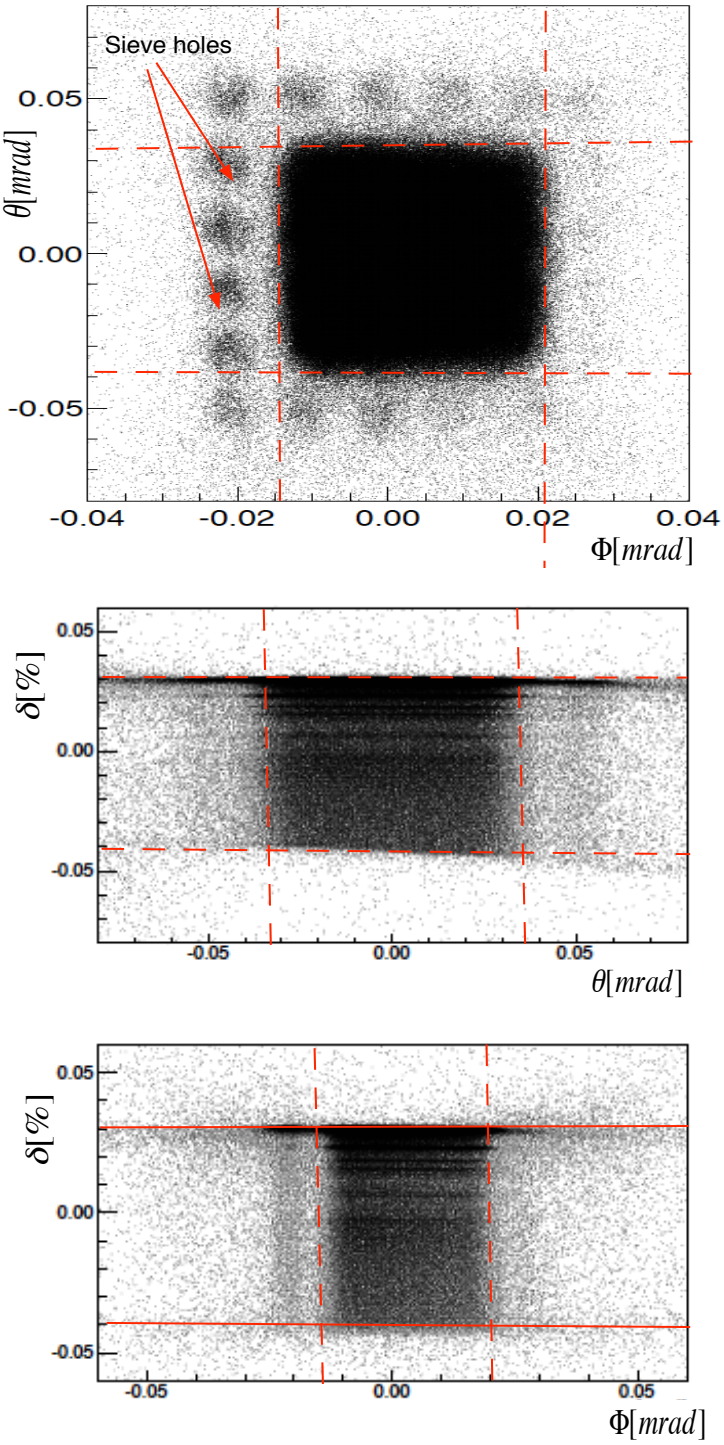

Fig. 3.16: Selection of geometric cuts (θ, ϕ, δ). Either from the $\theta - \phi$ or from $\delta - \phi(\theta)$ plots the cuts can be selected, but we used the $\delta - \phi(\theta)$ for all the runs.

3.7 Efficiency Calculations

3.7.1 Trigger Efficiency

A trigger happens in a scintillator when a charged particle passes through, and it plays the role of vertical drift chamber (vdc) event tracking. Trigger efficiency is a measurement of how well the scintillator and its associated electronics can generate an event. Inefficient photomultiplier tubes, low scintillation light transmission along the scintillator bars or loss of energy of the charged particles during their passage, all can contribute to the trigger inefficiency.

The trigger logic classifies the type of events that come to the HRS. The following important triggering events were produced during this experiment:

T1 = Coincidence of two or three hits among S1, S2 scintillator plane and the gas Cherenkov in the right HRS.

T2 = Trigger for the right HRS between either S1 and S0 or S2 and S0 but not S1 and S2.

T3 = Coincidence of two or three hits among S1, S2 and the gas Cherenkov in the left HRS.

T4 = Trigger for the left HRS between either S1 and S0 or S2 and S0 but not S1 and S2.

T5 = An event trigger happens in both left and right HRS, defined as T1 and T3.

T1 and T3 are the primary triggering events in the HRS produced by the scattered electrons passing through the detector's alignment. The T2 and T4 triggers are auxillary events generated in random directions by the particles other than electron (e.g., cosmic rays) or might be from scattered electrons, which were not detected by

scintillators. The trigger efficiencies for the left- and right - hand spectrometers can be found as

$$e_l = \frac{T3 + T5}{T3 + T4 + T5}, \tag{3.10}$$

$$e_p = \frac{T1 + T5}{T1 + T2 + T5}. \tag{3.11}$$

Triggering numbers can be found in the Hall A logbook for each of the runs we analyzed. The minimum triggering efficiency we found during our study was more than 99%.

3.7.2 Tracking Efficiency

The probability that the VDC senses a scattered electron and that the relevant tracking software constructs its trajectory successfully, is the tracking efficiency. By counting the events that a particular wire did not fire, but the nearest neighbors did, we can find the efficiency of that wire. At low trigger rates (several tens of KHz) the wire efficiency of the Hall A VDC is almost 100% [32], which is verified in various other experiments [37].

In the yield calculations, we always select the events in the "golden track", the best fitted track through all four wire planes of each VDC pair. This allows us to combine all kinds of track efficiencies (e.g., VDC, software, etc.) into one efficiency number, $e_{e(p)}$, defined as:

$$\epsilon_{L(R)} = \frac{N_{\rm cut}}{N}, \tag{3.12}$$

where, N is the number of type 3(1) events, and $N_{\rm cut}$ is the number of events that survive after good track and acceptance cuts. The subscripts L(R) on ϵ stand for left(right) HRS.

Ideally an electron should have only one track inside the detector, but the wire chamber can be interfered with by several other particles (due to delta or cosmic rays) at the same time and/or by noisy wires, so multitrack events are plausible. In these scenarios, the track algorithm reconstructs more than one possible trajectory.

In this experiment most of the runs had low trigger rates, but some of them with cryogenic targets had rates greater than 100 KHz. At these high trigger rates, it is possible that more than one electron reaches the wire chamber simultaneously and gives rise to multitrack events, and makes it very difficult to distinguish between good and bad events. Correction of the tracking efficiency due to multitrack events will be discussed in the next chapter.

3.7.3 Dead Time

There can be two types of dead time: electronic deadtime and computer dead time. If the electronics of the system requires a time to process an event (the "dead time") that is greater than the time difference between two consecutive events, there will be a pile-up of events waiting to be registered by the system, and consequently some of the events will be lost. If the dead time of the electronics is τ, which is $\sim 100 \times 10^{-9}$ for the Hall A DAQ [42], then the efficiency of the electronic system can be found as [43],

$$\epsilon_{DE} = \exp(-R\tau). \tag{3.13}$$

The maximum event rate for this experiment was around 200 kHz, so that the minimum interval between two events was 5×10^{-6}, which is 50 times greater than the electronic deadtime. So, we can confidently ignore this for our purposes.

The other dead time, the computer deadtime, arises due to the inabilty to record information to the computer hard drive from subsequent events. The efficiency of the

DAQ recording sustem can be calculated from

$$\epsilon_{DC} = 1 - DT_i = \frac{PS_i.N_i}{N^i_{trg}}, \tag{3.14}$$

where, N_i is the number of events recorded by the DAQ, N^i_{trg} is the number of events triggered of a particular type i, and PS_i is the corresponding pre-scale factor. The pre-scale factor reduces the load of data on the DAQ. For example, if the pre-scale factor is 10 and the trigger rate is 200 kHz, the DAQ has to record the data at the rate of 20 kHz. During this experiment the pre-scale factors were set to keep the dead time smaller than 10%.

Chapter 4

DATA ANALYSIS II

4.1 Overview

The working formula to extract the elastic cross section from the experimental data is

$$\frac{d\sigma}{d\Omega} = \frac{P_S \times N_{\text{net}}}{L \times t \times \Delta\Omega \times \Pi_i \epsilon_i} \times R, \tag{4.1}$$

where, P_S is the pre-scale factor, N_{net} is the net counts found by subtracting the dummy and background runs from a calibrated run and after applying necessary acceptance and particle identification cuts. L is the luminosity of the beam, t is the duration of a run, the ϵ_is are efficiencies, $\Delta\Omega$ is the phase space factor and R is the radiation correction factor.

For the colliding beam experiments one calculates the charge integrated luminosity, but for the cases where the target is fixed, like in the LEDEX experiment, we need to calculate the fixed target luminosity (L). The fixed target luminosity accounts for both the properties of the incoming beam and the stationary target. It is related to the interaction rate and cross-section as:

$$\frac{dR}{dt} = L\sigma, \tag{4.2}$$

$L = (N_e/s)d_T l$ and its units are $\text{cm}^{-2}s^{-1}$. The term N_e/s is the incident particle flux or number of incoming particles per second, d_T is the density of the target, and l is the target thickness.

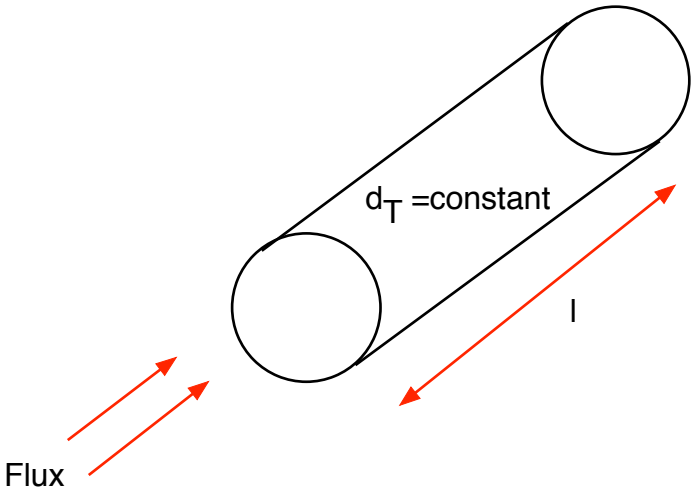

Fig. 4.1: Schematic view of a fixed target collision.

The radiation correction factor, R, can not be evaluated experimentally and hence we use a simulation code, called MCEEP (Monte Carlo for $(e, e'p)$) to determine that. We also use this simulation package to calculate the phase space factors. A brief description of MCEEP and the procedure for finding the above-mentioned quantities will be discussed in the next section.

In the previous chapter, we discussed the process for finding the efficiencies and the role of the pre-scale factors during a high event rate run. In this chapter we will focus on the procedure for finding the net run, correction to the tracking efficiency due to multitrack events at high trigger rates, and at the end of the chapter, we will present a section on error analysis.

4.2 MCEEP

The MCEEP code is a very well-documented simulation program, initially written by Paul Ulmer [44], keeping the $(e, e'p)$ reaction in mind. It has been siignificantly modified since then with contributions from many other people. With proper physics routines assimilated, it can now describe any single hadron emission experiment.

MCEEP allows users to choose many options (e.g., target position, target density, energy loss) specific to an experiment, ensuring that the simulation would be appropriate for a specific experimental set-up.

In MCEEP, a uniform random sampling method is used to simulate an event within the experimental acceptance, which keeps track of the weight of a corresponding observable (e.g, cross section, polarization) that are computed by the user for a selected model. A true Monte Carlo technique, on the other hand, generates events with a predefined weight factor, which requires lesser number dimensions to describe an experiment, but, on the downside, would also require an overhelmingly large number of events to obtain a statistically meaningful result [44]. For simulating a scattering environment in hall A, the MCCEP simulation proved to be very efficient with a high degree of accuracy.

By an event, we mean a combination of variables (there are seven in total), that perfectly describe a reaction in the laboratory. For elastic scattering, only nominal in-plane angle (ϕ_{en}) and out-of-plane angle (θ_{en}) variables are sampled, and all other quantities can be found from them. A corresponding vector is produced in the laboratory to coordinate the system for each of these events, which is then modified to become a vector in the spectrometer reference frame. The pre-resolution of the spectrometer is obtained by applying necessary actions on this vector. This vector is then transformed into the focal plane reference system by the use of a transfer function. Simulation of the position resolution of the VDC is done by a track reconstruction matrix. Finally, the vector is transferred back to the target frame via an inverse transfer function. The details of the simulation procedure can be found in ref. [44].

MCEEP is capable of producing results by performing multidimensional integration for elastic, bound or continuum scattering. For elastic scattering, it is designed to carry out a two-dimensional integral over the electron solid angle, $d\Omega = cos\theta d\theta d\phi$.

Elastic scattering in MCEEP can be simulated either considering the recoil nucleus recoiling into the hadron arm, or it can be left kinemetically unrestricted as a single arm for an elastic scattering experiment.

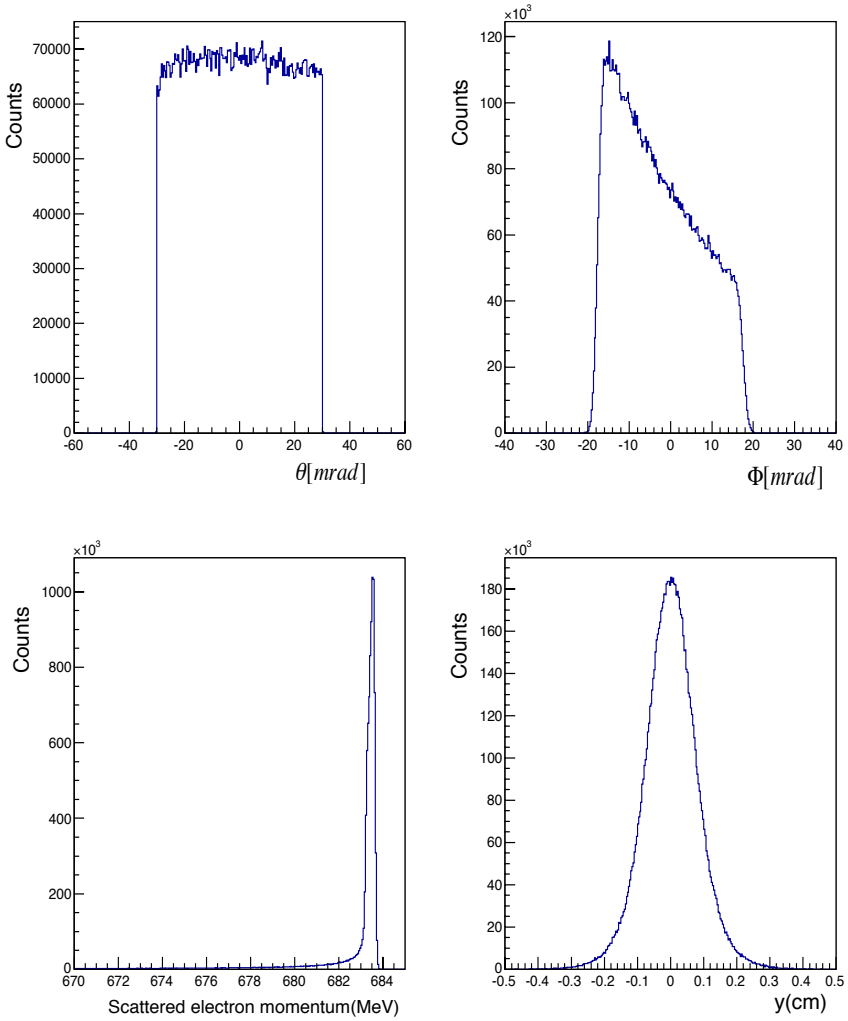

Fig. 4.2: MCEEP Simulated variables for a particular run.

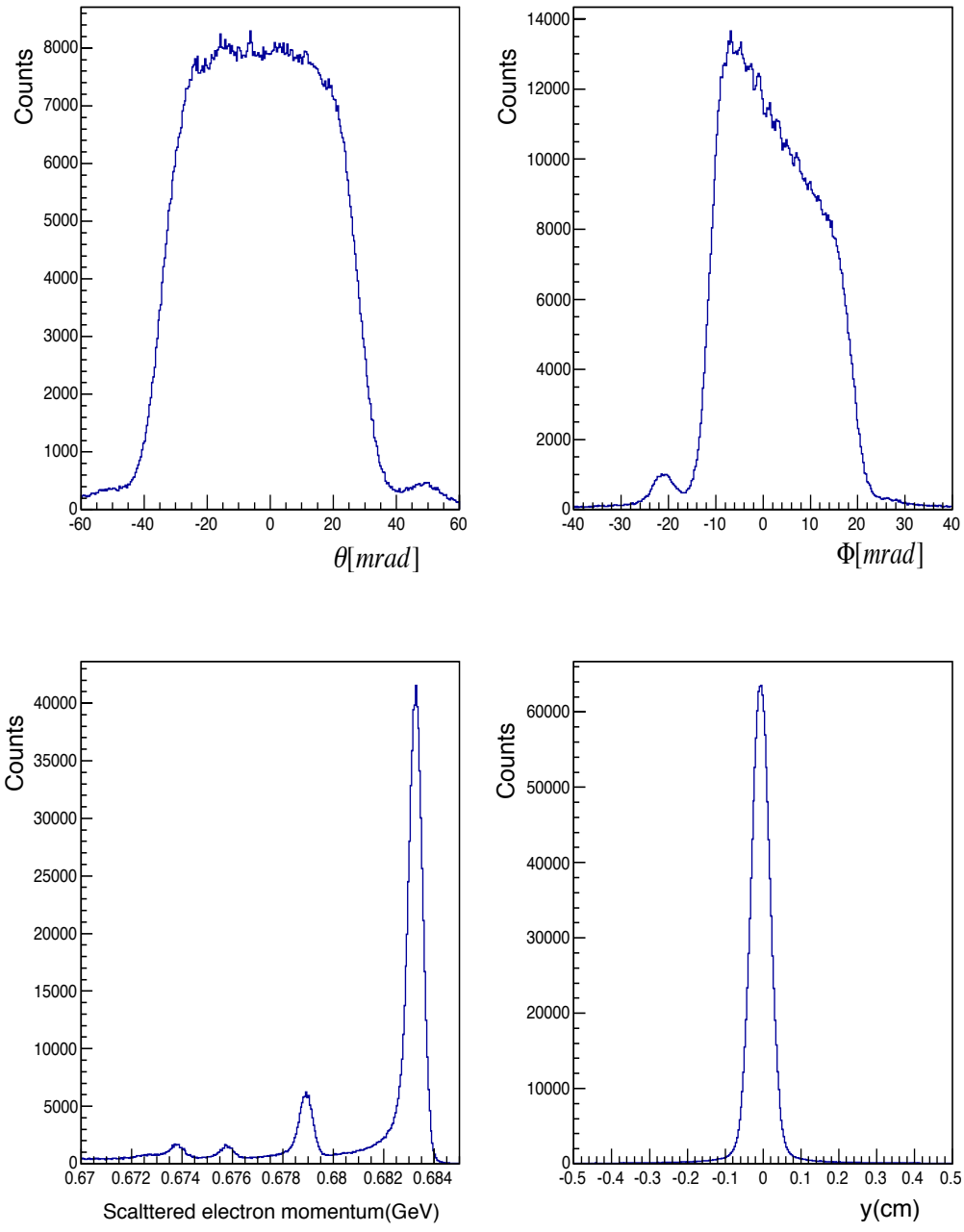

Fig. 4.3: Variables for the same kinematics but for real run. These are compared with the MCEEP counterpart, shown in Fig. 4.2.

4.2.1 Radiative Corrections

The electron scattering formula is derived (e.g., Eq. 1.10) from the Born approximation (one photon exchange). However, in reality, both the incoming and scattered electrons will radiate real and virtual photons during their passage, which will eventually change the value of cross-section to some extent from its bare value. The theoretical calculations do not consider these effects, and so, to compare the experimental result with theory, the experimental data must be unfolded radiatively.

There exists no direct way to measure radiation effects. Although, the MCEEP code can calculate the radiation algorithm for the carbon, hydrogen and deuteron targets. We have taken that advantage to undress the radiation effects for these three targets, and we use this calculation to correct for the loss of events in the radiation tails for these targets. MCEEP considers both internal and external sources of radiation. The internal radiation comes from the interaction of the particles among themselves, whereas, the external radiation is generated by the other target nuclei.

4.2.2 Internal Radiations

Both real and virtual photon can contribute to internal radiation loss. The real photon can be further categorized into soft or hard, depending on the energy of the photons. If the energy of a photon is less than 0.35 MeV, it is called a soft photon, and a photon with energy higher than 0.35 MeV is called a hard photon. Here, the energy reference or the cut-off energy is taken as the experimental energy resolution.

The virtual and soft photons are taken into account in the Schwinger [45] term, found by the Penner calculation [46],

$$C_{\text{schwing}} = e^{-\delta_r}(1 - \delta_v), \tag{4.3}$$

where $\delta_{r(v)}$ is the real(virtual) photon contribution. The emission of a hard photon creates Bremsstrahlung and gives rise to the radiative tail. A hard photon can be emitted in any direction, but the peaking approximation is used here, which assumes that the photons are radiated in the direction of the incident and scattered electrons. The elastic radiative tail has been calculated from a prescription by Mo and Tsai [47].

4.2.3 External Radiation

When a charged particle passes through matter, it suffers multiple collisions with the atomic electrons and its average energy loss can be calculated using the Bethe-Bloch formula [48]. However, the amount of energy loss has a distribution because of statistical fluctuations in the number of collisions and the energy lost in each collision. The energy loss distribution (straggling) is approximated by either Landau, Vavilov or Gaussian distributions [49], depending on the ratio between the mean energy loss and the maximum energy transfer possible in a single collision.

When the charged particle is affected by the Coulomb field of nuclei beside the target nuclei, external bremsstrahlung occurs. Energy is lost and is dependent on the length of the material traversed or the radiation length. This is treated using the Bremmstrahlung interaction function [49].

When traversing a medium, if an electron is deflected at a small angle at the beginning, it could then suffer multiple scattering. The Moliere [50] formula is used in MCEEP to describe this process.

4.2.4 Method of Finding the Radiation Correction Factor

At each kinematic setting, we simulated the q^2 distribution in two ways through MCEEP, one without the radiation loss and the other with the radiation loss. We then found the value of the correction factor bin by bin by taking the ratio of these

two. The distribution of a real run with same interval and bin is multiplied by this factor to get the new radiatively unfolded distribution. Figures, 4.4, and 4.5 illustrate this procedure.

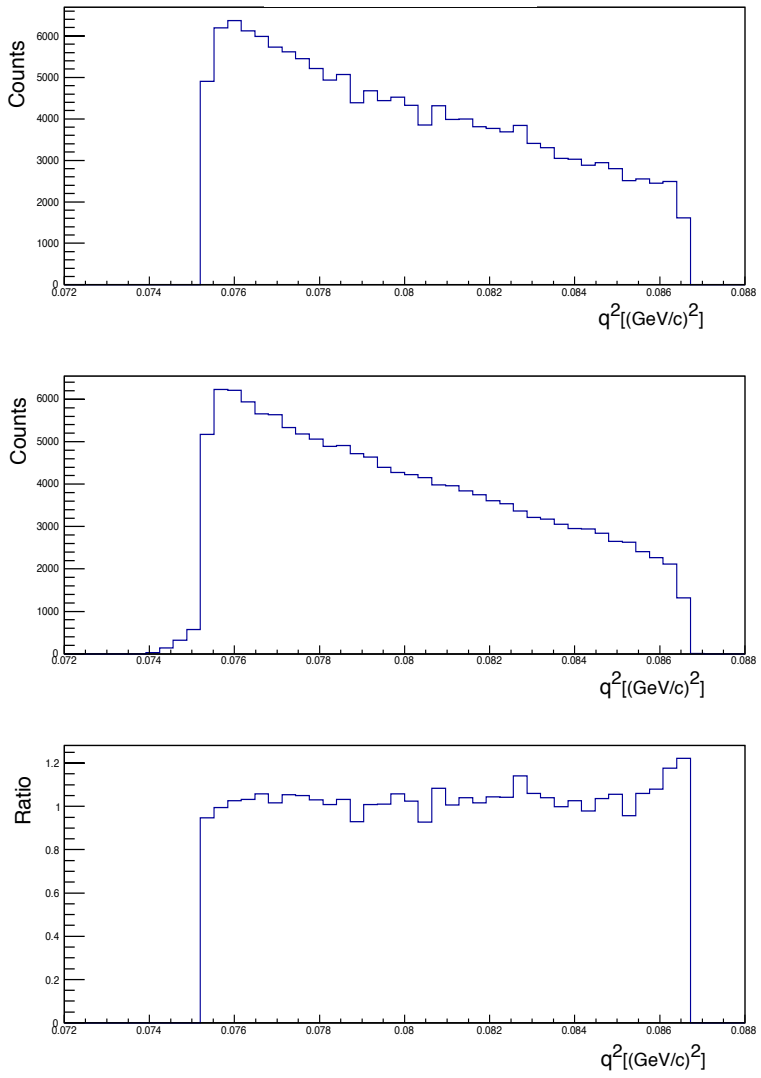

Fig. 4.4: The top panel is the MCEEP simulated q^2 distribution with radiation loss turned off, the middle panel shows the same distribution with radiation loss turned on, and the bottom panel shows the ratio, R.

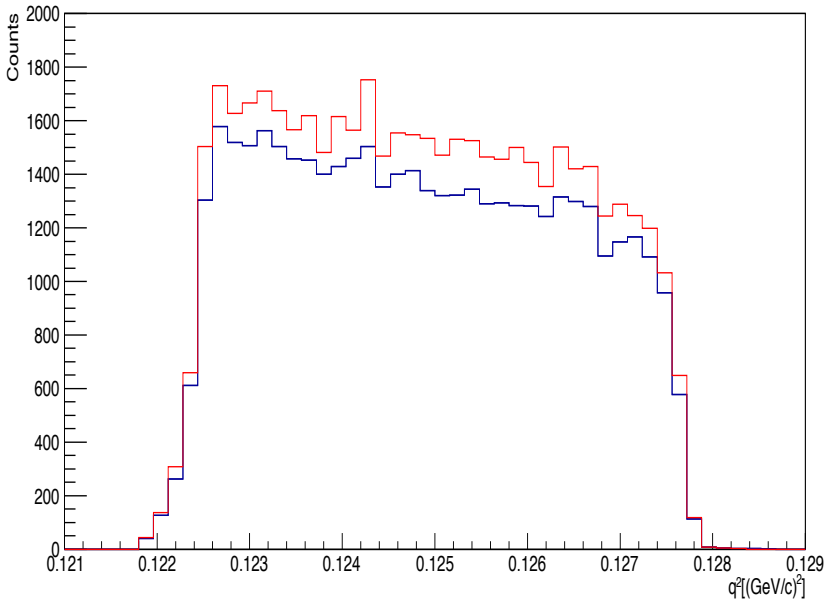

Fig. 4.5: The blue line shows the uncorrected data and the red line shows the data after applying the radiation correction factor.

4.3 Background and Dummy Subtractions

Whenever any experiment is performed, it is important to keep in mind that there will be always some sort of background radiation. The actual source of the background radiation is un important, but we always have to subtract the resulting counts due to this background radiation from the counts from the actual run. In this experiment, the event rate is normally very high so, the background events, which are taken at every angle setting of the spectrometer as cosmic ray runs, are very small compared to the actual events. Figure 4.6 shows an example of background subtraction.

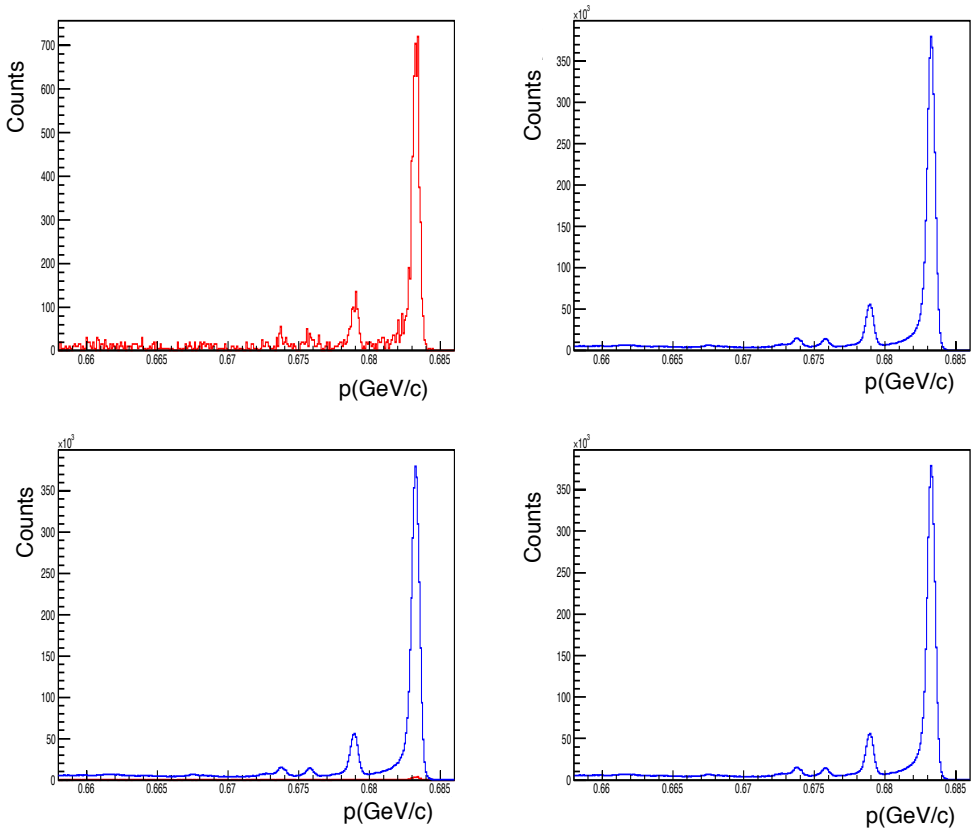

Fig. 4.6: The top left diagram is for a cosmic ray run taken with the same spectrometer setting as the actual run on top right. In the bottom left diagram both the cosmic and actual runs are drawn, and is evident that in this case, the cosmic contribution is negligible. The fourth diagram is the net count after the cosmic contribution being subtracted. We found that there was a very little beam charge accumulation in the BCM. This means that the beam currents were not exactly zero during the cosmic runs, which gave rise to the carbon elastic and inelastic peaks in the spectrum.

The cryogenic targets used during this experiment were kept in aluminum cells. Therefore, the electrons that came to the spectrometer had two different origins, some scattered from the liquid target and some from the aluminum container. It is very possible to eliminate the contributions from the aluminum by putting a tight cut on the reaction position, which works very well for the 15 cm loops; however, for the 4cm loops, this would result in a loss of too many events to preserve good statistics.

For each kinematic setting of the experiment, scattering from the dummy cells of same length (4 cm and 15 cm) wes measured. If these counts are subtracted from those from a cryogenic target, we obtain the contribution solely due to hydrogen or deuterium. The dummy subtraction procedure is bit more complicated than the background subtraction, since,the window thickness of the dummy cells (0.96mm) is different than tat of the cryogenic cells (0.13 mm), which is done deliberately to increase the event rate from the dummy targets.

The difference in window thickness is dealt with by introducing an efficiency factor, ϵ_{dummy} calculated as,

$$\epsilon_{\text{dummy}} = \frac{n_d}{n_l}, \tag{4.4}$$

where n_d is the number of events from the dummy run and n_l is the number of events from the liquid target run. This factor, ϵ_{dummy} is then used to normalize the dummy spectrum for a variable say, Q^2, for the dummy run to get normalized dummy (Fig.4.7). This normalized dummy run is then subtracted from the liquid target run bin by bin. The liquid cell, dummy, and substracted Q^2 spectra are shown in Fig. 4.7 for a typical run.

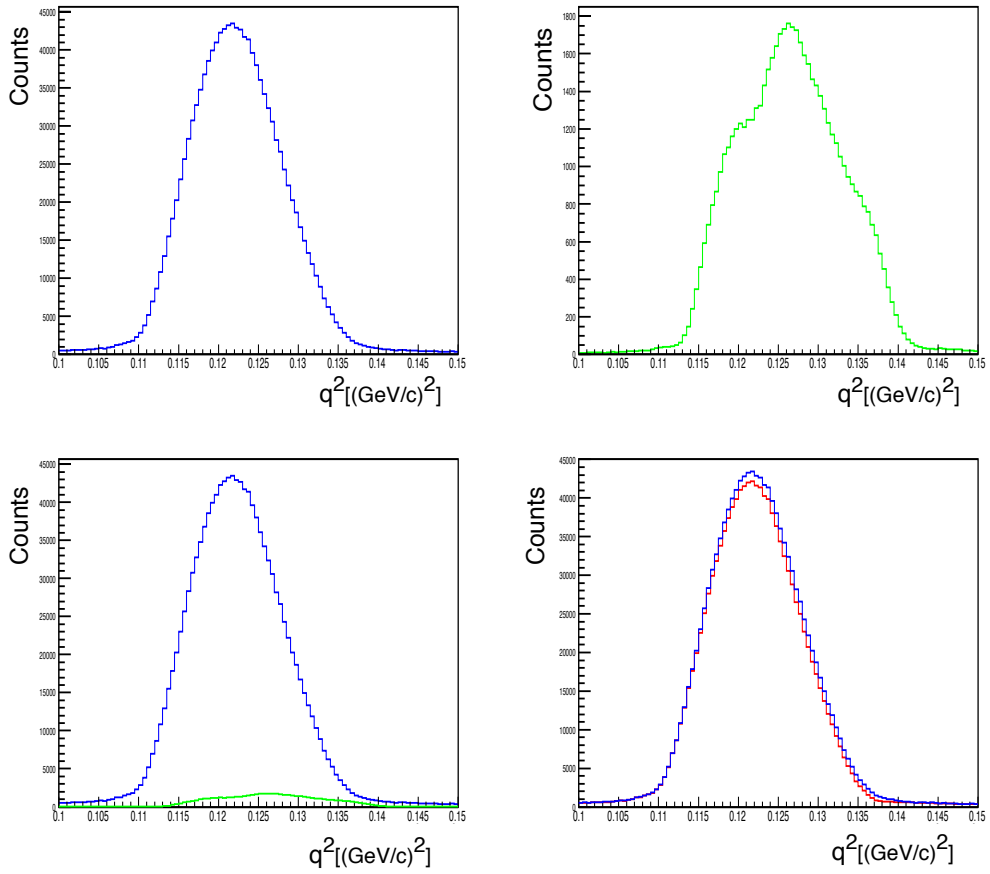

Fig. 4.7: The top left (right) is a q^2 distribution from a ^{1}H cryo-target cell (normalized dummy). In the bottom left panel is a quantitative comparison between these two, where the blue curve represents the cryotarget and green is the dummy target. The red curve in the fourth diagram is after dummy subtraction and the blue curve is before subtraction.

4.4 Target Density Correction

When a beam of electrons passes through the liquid target, the beam transfers some of its energy to the neighboring liquid, which results in a change in the density of the target known as the boiling effect. Hence, the density of the target, which is assumed to be constant for a particular target in the cross-section determination, is

not actually constant, rather it is linearly related to the beam current. So, at the higher beam currents the boiling effect will be more prominent. Our main purpose here is to find the charge radius of the nuclei, and runs at the low angle settings are more important. At the low angles, the beam currents are normally low, which makes the boiling study less important. However, the boiling effect has been studied thoroughly by Byungwuek Lee [31] for this experiment. His analysis reveals that at low currents($\sim 5\ \mu A$) the the density variation is less than .25% and at the highest current settings ($\sim 30\ \mu A$) this variation is less than 2%. We used his boiling study results in the systematic uncertainty calculations.

4.5 Correction to the Tracking Efficiency at High Trigger Rate

As discussed earlier, in most of the runs we analyzed, the multi-track events are rare. However, during the very high trigger rate scenarios the multi-track events spike to 10-12% and the tracking efficiency has to be corrected for multi-track events for these situations. Table. 4.1 shows the change in the number of multi-track events with event rate, and Fig. 4.8 shows the contribution of multi-track events in the total events.

Table 4.1: Multi-track event ratio at high rate runs

Target	Angle [°]	Event Rate [kHz]	Ratio [%]
^{1}H	14.5	166.7	11.9
	17	79	7.5
	21	61	4.7
	24	24.6	2.3
^{2}D	14.5	188.6	12.3
	17	92.5	9
	21	60.5	5.7
	24	25.2	3.4

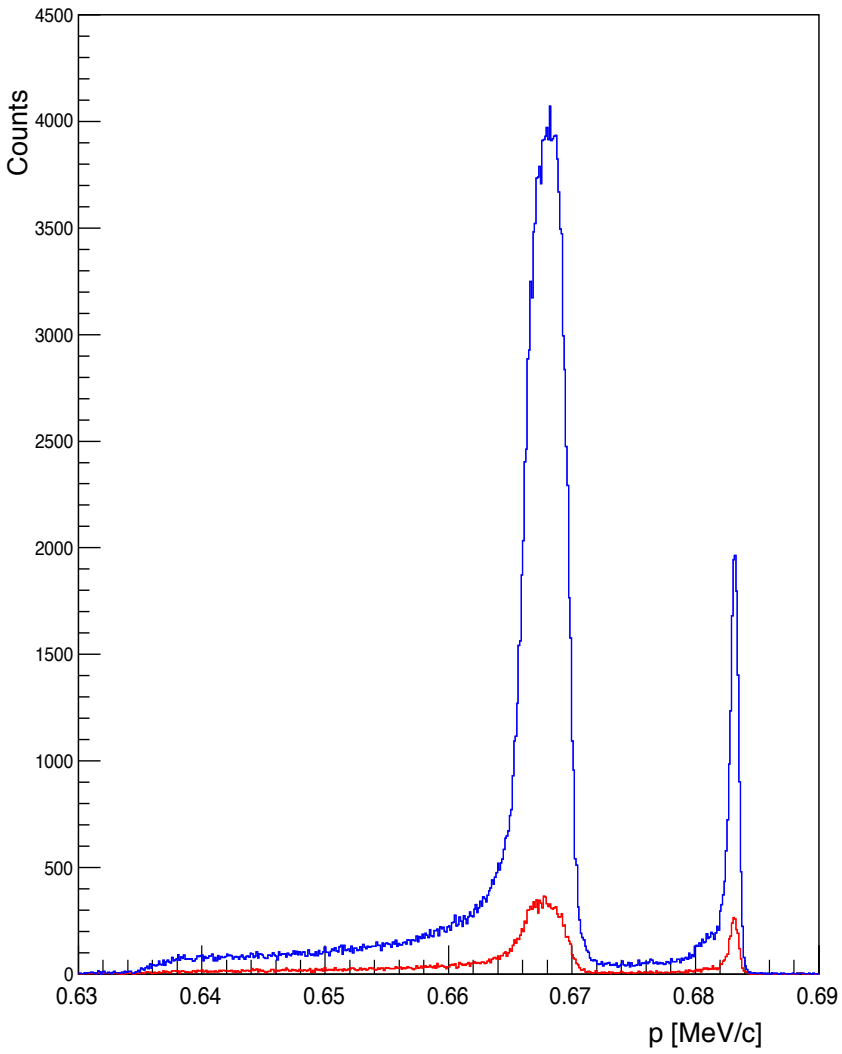

Fig. 4.8: A momentum distribution of all events (blue) and from multi-track events only (red) at the highest trigger rate for hydrogen.

Ideally an electron event should produce a single track. However, multi-track events can be generated from electronic noise, errors in the tracking algorithm, or importantly, when multiple electrons pass simultaneously through the wire chamber. When these multi-tracks are attributed to good electrons, a correction must be applied. In theory, multi-tracks can be generated from more than two good electrons,

but the chance of that happening is very low. Therefore, in our multi-track efficiency study, we focused on events that have two real electron tracks only.

The LHRS is equipped with two layers of Cherenkov detectors, the preshower and the shower, whose main purpose is to differentiate between electron and pion events by finding the energy deposited by the passing particles. However, it is also true that whether an event is from one electron or two electrons, it leaves a trail in the shower/preshower energy distribution, a two-electron event would deposit twice as much energy as that of a one-electron event [31]. Figure 4.9 shows the energy deposited by electrons in a high event rate run. There are two distinctive peaks, one around 350 MeV and the other around 700 MeV, which corresponds to one- and two-electron events, respectively. Also, the ratio of the area under the two different curves gives an estimate of the ratio of two-electron events to one-electron events.

After the multi-track events are identified, the multi-track efficiency is then calculated by the following procedure:

1. One-track efficiency, ϵ_1, is found from the usual prescription given in the previous chapter.

2. Contribution from the two-track events are found and weight factors ω_1 for one-track and ω_2 for two-track events are assigned.

3.The tracking efficiency, ϵ_1, for the two-track events is found the same way as for the one-track efficiency but with the conditions on the event type 3 that an event should have two-electrons, each wire plane has two clusters, and each cluster hits 3 to 6 numbers of wires. The spectra are then corrected for the two-electron event probabilty as determined from the peak area in Fig. 4.9. The resulting correction is shown in Fig. 4.10.

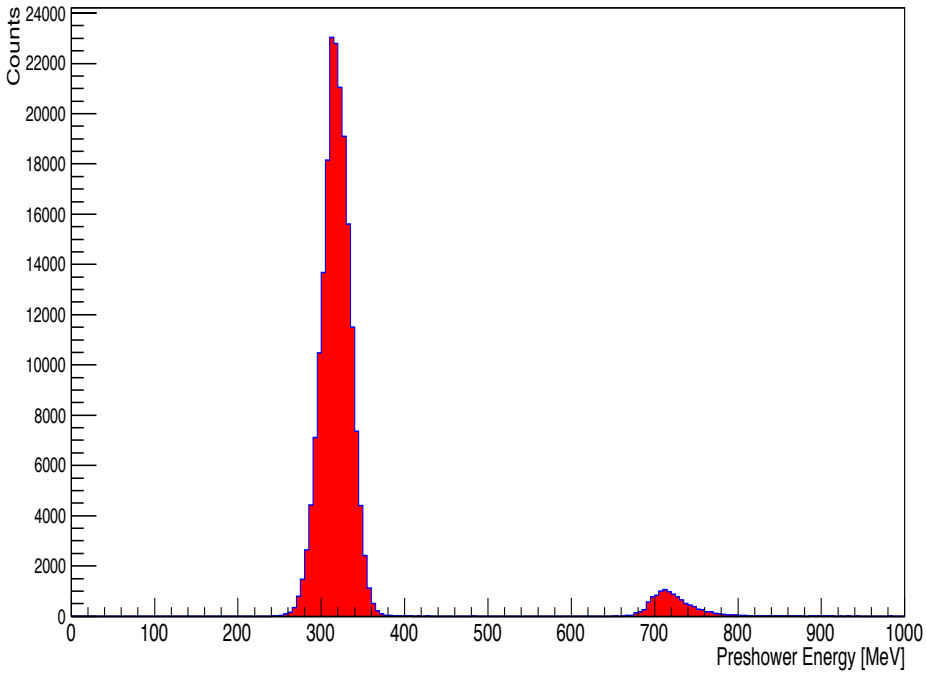

Fig. 4.9: Pre-shower energy distribution with multi-track events.

Table 4.2: Ratio of two-electron to one-lectron events.

Target	Angle [°]	Event Rate [kHz]	Ratio of two electrons [%]
^{1}H	14.5	166.7	5.1
	17	79	1.3
	21	61	0.8
	24	24.6	0.2
^{2}D	14.5	188.6	4.2
	17	92.5	2
	21	60.5	0.95
	24	25.2	0.4

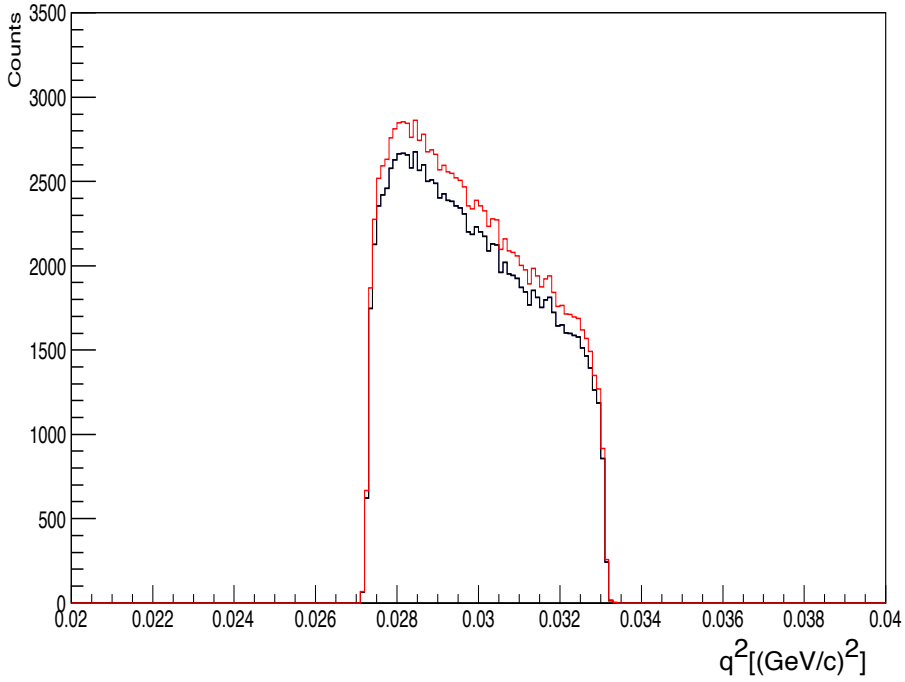

Fig. 4.10: q^2 distribution of a ^{2}D run at the highest trigger rate. The black line is before the multi-track correction and the red line is after the correction.

4.6 Uncertainty analysis

There are two basic sources of uncertainities involved in measurements during an experiment; the statistical uncertainty and the systematic uncertainty. Statistical uncertainties result from the random fluctuations in a measurement due to the stochastic nature of numerically sampling the same measurement over and over again. The fractional statistical uncertainty can be estimated as

$$stat = \frac{\sqrt{n}}{n}, \tag{4.5}$$

where, n is the number of observations. As the number of observations increases, this error decreases. In our study, cross sections of boron carbide and lithium have been

determined with respect to carbon. In such cases, the statistical error for carbon will also be propagated into the error for boron carbide/lithium in the following manner,

$$stat = \sqrt{\left(\frac{\sqrt{n_1}}{n_1}\right)^2 + \left(\frac{\sqrt{n_2}}{n_2}\right)^2} \tag{4.6}$$

Systematic uncertainties, on the other hand, arise from imperfect and/or from inaccurate measuring instruments. For a specific error of this type, error always occurs in the same direction and will accumulate. Unlike statistical uncertainty, increasing the number of mesurements does not reduce the systematic uncertainty.

The biggest source of systematic uncertainty in this experiment comes from the solid angle and luminosity measurements. We know that the in (out) plane angle can be measured within $\pm$ 2(6) msr [41]. So to estimate the uncertainty in the cross-section due to solid angle measurements, we observerd the change in the results produced by changing the in- and out-plane angle information within its accuracy limit in the MCEEP simulation code. On the other hand, the luminosity is proportional to the beam current, target thickness, and the density of the target. Thus, in the calculation of uncertainty in luminosity, each of these terms will contribute. We found from the beam current calibration that the maximum normalization error coming from the beam current is 0.5% [31].

The liquid target cells have 2 mm curvature at the back, which creates a change in the effective target length. However, this curvature effect is small and generates a maximum change of 0.2% in target length [31].

None of the targets are 100% pure and, in addition, the target densities are affected by heating of the beam and varied with beam intesity. Both of these effects altered the effective density of the target during the experiment. The impurity in the target is typically very low (less than 0.5%) [51], but in high current situations, the density changes by approximately 2% due to boiling in the liquid target.

In most cases, the efficiency of the measuring components is very high and the uncertainty in measuring the efficiencies is less than a percent. However, at the higher trigger rates, the tracking efficiency (one track) falls as low as 66% and it was necessary to consider multitrack events attributed to be good electron events. It is not straightforward to tell which electron events (multitrack) are really good and which are not. Thus, the efficiency corrections becomes complicated in these situations and induce larger uncertainties.

There are also contributions to the systematic errors from the radiation correction factor [38], selection of the elastic peaks, and from the background subtraction [23]. All components of the systematic error are presented in Table 4.3.

Table 4.3: Systematic Uncertainties

Quantity	Normalization [%]	Random [%]
Beam Current	0.5	—
Solid Angle	1.0	—
Composition	0.05	—
Target thickness	0.6	—
Efficiency	—	1.0
Radiation correction	1.0	—
Background subtraction	—-	1.0
Overall	1.53	1.41

As mentioned earlier, for a few of the targets, the cross section was determined by the ratio method. For example, the cross section of boron obtained from using a

B_4C target, was calculated with the following formula,

$$\sigma_B = \frac{\sigma_C}{4}\left(\frac{\sigma_{B_4C}}{\sigma_C} - 1\right). \tag{4.7}$$

Many of the terms (e.g., luminosity, solid angle, radiation correction factor) cancel in the ratio $\frac{\sigma_{B_4C}}{\sigma_C}$, but, the error for carbon will be added quadratically for the uncertainty calculation of σ_{B_4C} or boron. That means, in the ratio method, nothing can be measured more accurately than carbon. It can also be predicted from the equation above that, at low event rates (higher scattering angles), the statistical uncertainty could be very high for the boron cross section due to the four-fold reduction of statistics in both B_4C and carbon.

Chapter 5

RESULTS FOR THE CROSS SECTION

5.1 Overview

The previous two chapters discussed the procedures for obtaining the scattering cross section from the raw data. In this chapter we will present our cross-section results both quantitively and graphically.

The internal structure of a nucleus can be better predicted from its form factor, which can be found from the ratio of the cross section to the Mott cross section. For example, quantities such as the charge density and charge radius can be extracted from information in the form factor. In the next chapter, we will discuss about the parametrization of the form factor and the techniques for finding the charge density distribution function and charge radius.

5.2 Cross-section results for Carbon, Deuterium and Hydrogen

Data for these targets were measured in late 2006. The beam energy during these runs was 685 MeV and we have analyzed the runs in the scattering angle range from 14.5° to 50.5°. Tables 5.1, 5.2 present the cross sections for these runs at various angles.

The coss section is measured over an acceptance region of the spectrometer; however, at the edges of the acceptance the result becomes very unpredictable and unreliable (Fig. 5.1). To avoid this, we always take the result at the middle point of the acceptance and call it the scattering cross section and denote it by σ. Note that, σ here does not mean total cross section.

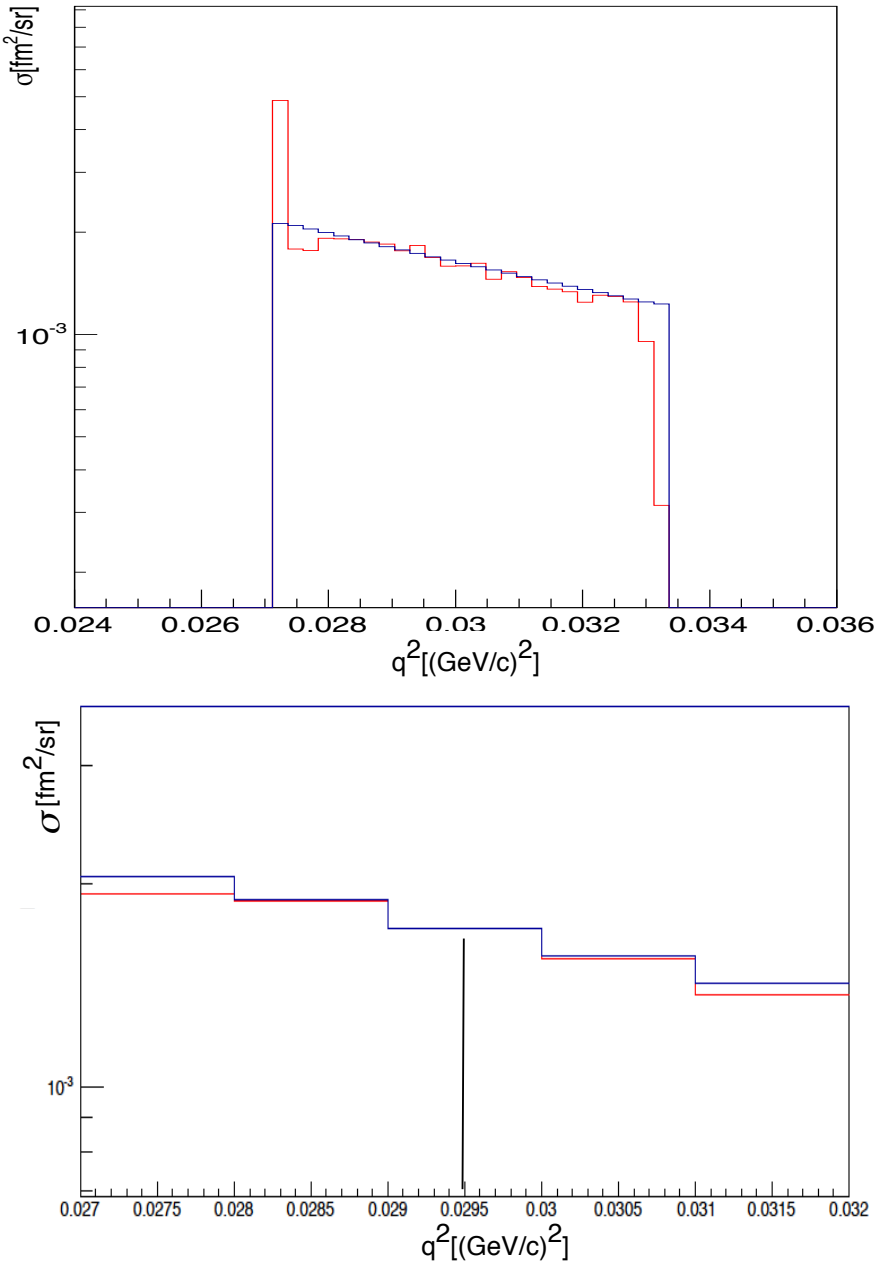

Fig. 5.1: Cross-section determination. The top diagram shows the entire acceptance range and the bottom diagram is drawn within the meaningful acceptance region. The blue line represents the MCEEP simulated result and the red line represents the result found from the experiment. The vertical black line shows the position of the most reliable position value for the cross section.

Table 5.1: Cross-section results for Carbon, Deuterium, and Hydrogen at 14.5° to 30.5°.

Angle [°]	Target	t [mins]	I [μA]	q [fm^{-1}]	R	σ [fm^2/sr]	Sys [%]	Stat [%]
	^{12}C	15.80	2.18	0.87	1.10	3.14×10^{-2}	2.0	0.19
14.5	^{2}D	15.00	2.06	0.87	1.10	1.72×10^{-3}	2.7	0.27
	^{1}H	16.70	2.01	0.87	1.13	3.62×10^{-3}	2.7	0.40
	^{12}C	12.03	2.81	1.05	1.10	6.82×10^{-3}	2.0	0.18
17.0	^{2}D	12.10	2.82	1.02	1.10	6.86×10^{-4}	2.6	0.34
	^{1}H	17.07	2.07	1.03	1.20	1.74×10^{-3}	2.6	0.20
	^{12}C	16.80	4.67	1.27	1.13	9.30×10^{-4}	2.2	0.32
21	^{2}D	15.12	4.76	1.26	1.10	1.67×10^{-4}	2.1	0.34
	^{1}H	14.22	4.93	1.25	1.15	6.45×10^{-4}	2.1	0.19
	^{12}C	12.25	7.30	1.47	1.14	1.26×10^{-4}	2.2	0.47
24.0	^{2}D	9.59	4.63	1.44	1.12	6.72×10^{-5}	2.1	0.36
	^{1}H	13.71	3.80	1.43	1.17	3.5×10^{-4}	2.0	0.27
	^{12}C	27.44	9.10	1.82	1.10	2.35×10^{-7}	2.4	4.24
30.5	^{2}D	26.89	1.76	1.78	1.11	1.17×10^{-5}	2.1	0.31
	^{1}H	18.89	1.59	1.76	1.11	1.27×10^{-4}	2.1	0.26

Table 5.2: Cross-section results for Carbon, Deuterium, and Hydrogen at 40°, 45°, and 50.5°.

Angle [°]	Target	t [mins]	I [μA]	q [fm^{-1}]	R	σ [fm^2/sr]	Sys [%]	Stat [%]
40.0	^{12}C	25.00	18.46	2.34	1.12	5.70×10^{-7}	2.2	2.35
	^{2}D	36.80	4.35	2.28	1.12	1.13×10^{-6}	2.1	0.40
	^{1}H	18.55	4.16	2.2	1.12	2.60×10^{-5}	2.1	0.35
45.0	^{12}C	116.17	23.40	2.63	1.13	1.37×10^{-7}	2.2	1.96
	^{2}D	35.98	10.10	2.51	1.12	4.23×10^{-7}	2.3	0.65
	^{1}H	16.31	6.07	2.42	1.12	1.44×10^{-5}	2.2	0.33
50.5	^{2}D	42.63	20.46	2.79	1.12	1.03×10^{-7}	2.5	1.10
	^{1}H	18.33	19.86	2.64	1.12	1.072×10^{-5}	2.5	0.50

In tables 5.1, 5.2, we have used R for radiation correction factor, Sys. for systematic uncertainty and Stat. for the statistical uncertainty.

Figures 5.2,5.3,5.4 show our extracted cross sections for carbon, deuterium, and hydrogen, respectively. The experimental cross section results for carbon are compared with the Offerman's Fourier-Bessel parametrization model [52] while hydrogen results are compared with results found from Monte-Carlo simulation [44]. On the other hand, we compare our cross section results for deuteron with the results from

previous independent anlyses done by Byungwuek Lee [31] on the same data sets as ours. It is to be noted that these diagrams are drawn in logarithmic scale, and the error bars are hidden within the geometric shape of the markers.

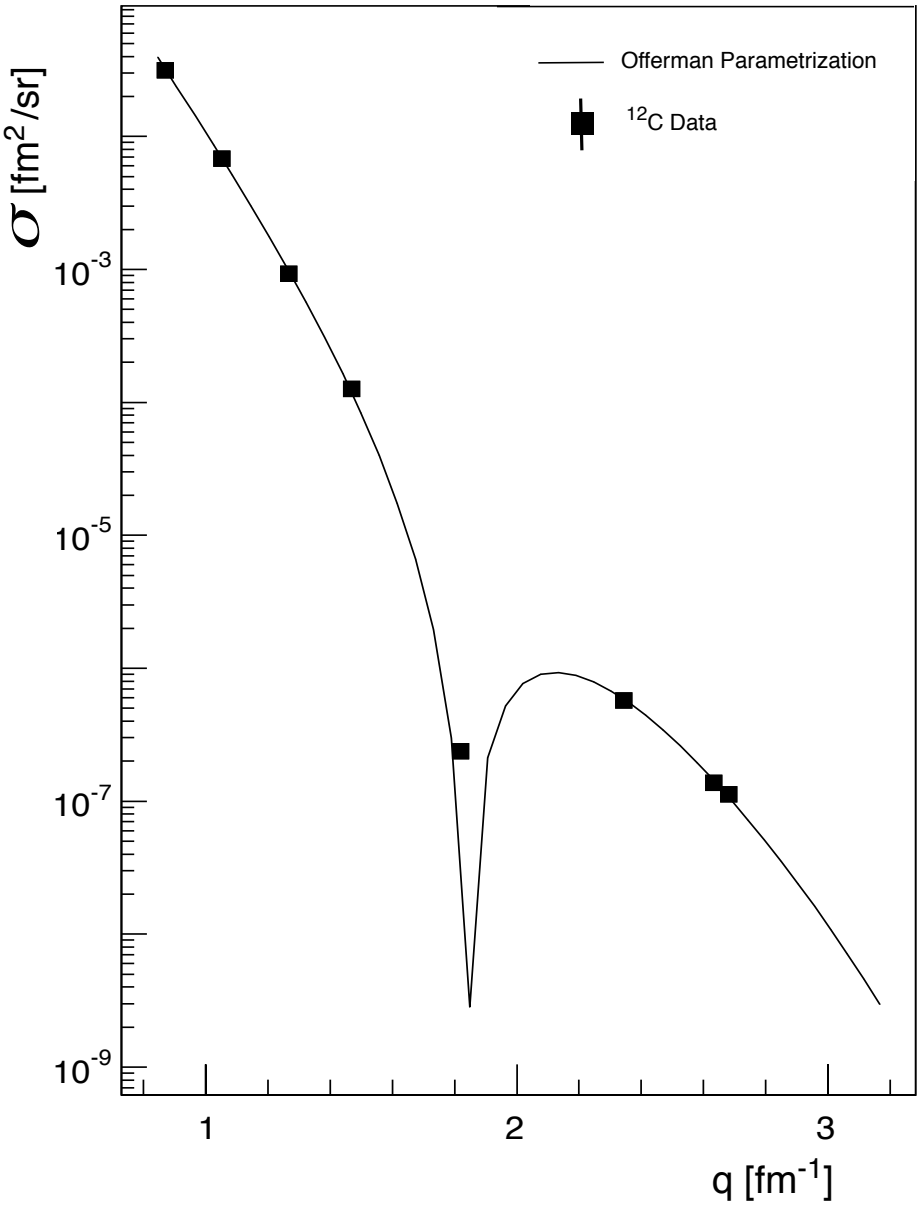

Fig. 5.2: Carbon cross section. The curve corresponds to the Offerman parametrization model [52].

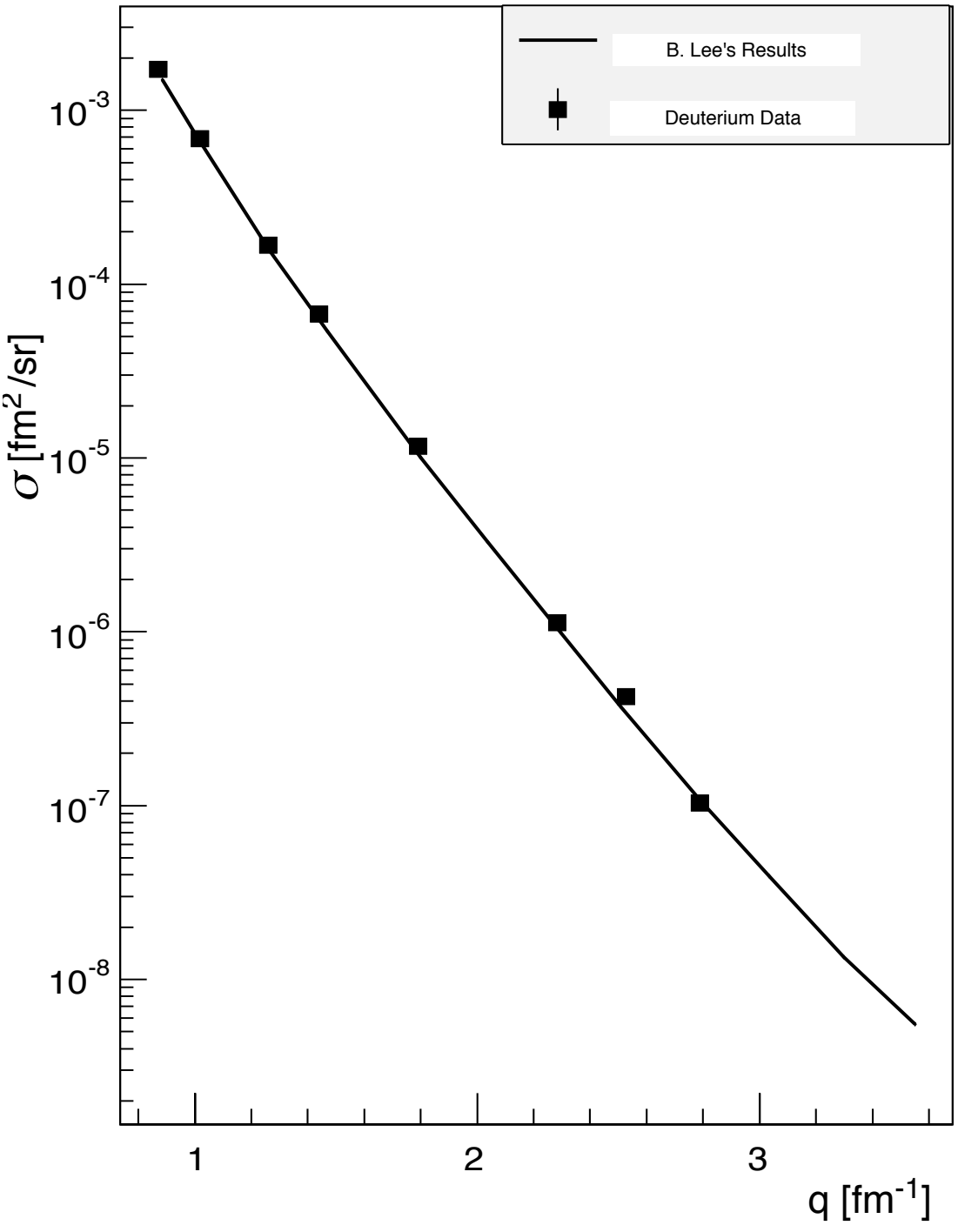

Fig. 5.3: Deuterium cross section. Our cross-section results are compared with the experimental results obtained by Beyong Lee on the same experiment [31].

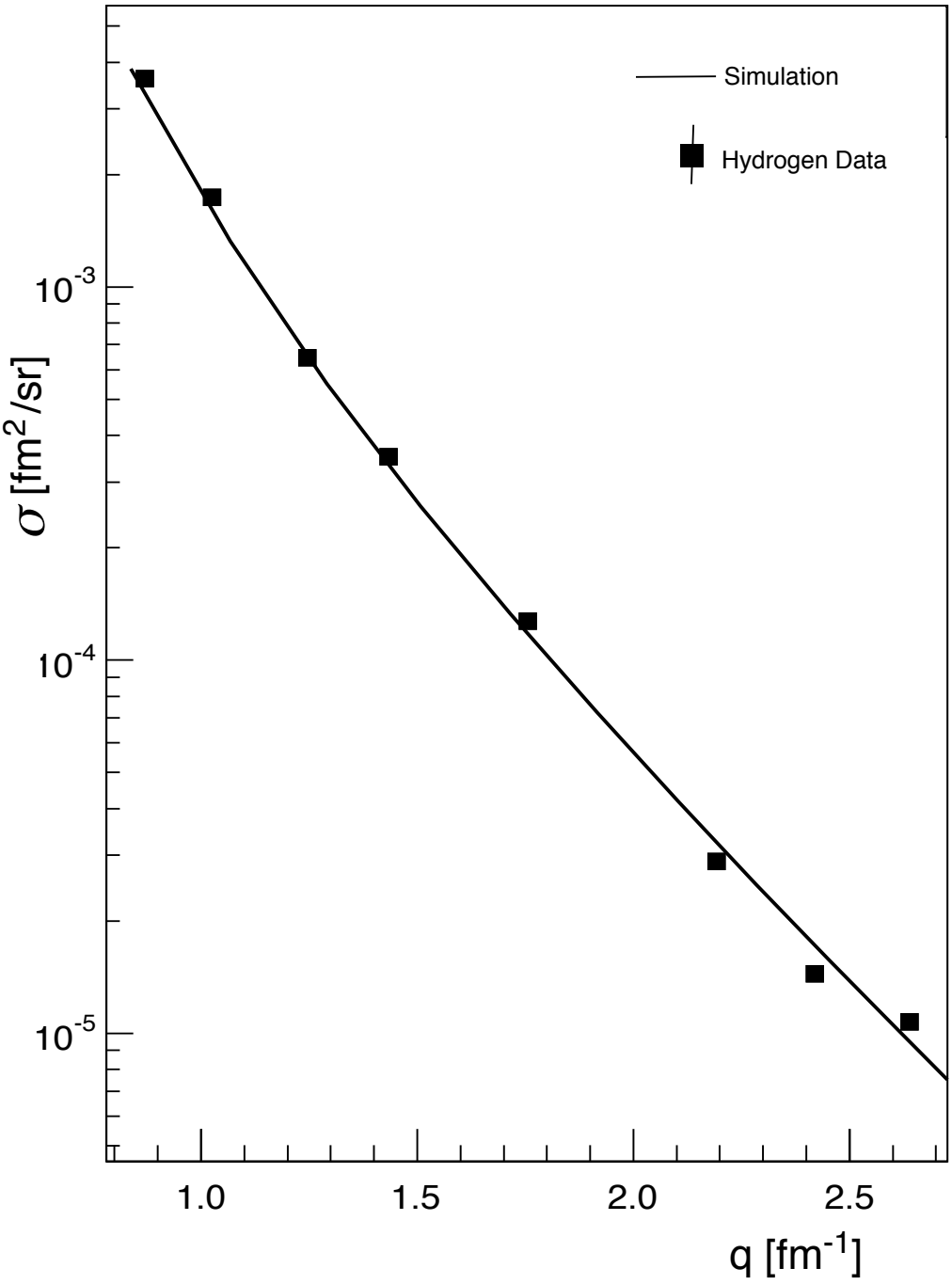

Fig. 5.4: Hydrogen cross section. Simulation curve is generated from MCEEP simulation results [44].

5.2.1 Cross-section results for Carbon, Lithium, and Boron

These data were taken in early 2007 and the beam energy during these runs was 362.4 MeV. Tables 5.3, 5.4, 5.5 show the cross-section results for carbon, boron carbide, boron, and lithium.

The working formula for determining the elastic scattering cross section is,

$$\sigma = \frac{N \times R}{L \times t \times \Delta\Omega \times \Pi_i \epsilon_i}. \tag{5.1}$$

It can be seen from this equation that the scattering cross-section is proportional to the number of events (N) in the elastic peak and inversely proportional to the luminosity (L). At a particular angle, if we keep the acceptances the same and consider the fact that at low event rates the efficiencies remain the same in the cross-section measurements of two different targets, then several terms cancel in the ratio of cross sections and take the form,

$$\frac{\sigma_1}{\sigma_2} = \frac{N_1 \times L_2 \times t_2}{N_2 \times L_1 \times t_1}. \tag{5.2}$$

Thus, for the same kinematics, if we know the cross section for one of the targets, the cross-section of the other can be determined by using the Eq. 5.2. For lithium and boron carbide, it is straightforward. To calculate the corss section for Boron, we subtract the carbon cross section from boron carbide and then we divide by 4.

Table 5.3: Cross-section results for Carbon, Lithium, and Boron at 12.5° to 26°.

Angle [^{0}]	Target	t [mins]	I [μA]	$q_{eff}[fm^{-1}]$	R	σ [fm^2/sr]	Sys [%]	Stat [%]
12.5	^{12}C	3.08	0.272	0.41	1.10	0.622	1.9	0.63
	B_4C	12.00	0.221	0.41	1.10	2.404	2.5	0.64
	^{10}B	12.00	0.221	0.41	1.10	0.445	3.1	0.69
	^{6}Li	12.84	0.477	0.41	1.1 0	0.157	2.5	0.78
14.1	^{12}C	16.80	0.346	0.45	1.10	0.414	1.9	0.25
	B_4C	16.42	0.330	0.45	1.10	1.546	2.5	0.65
	^{10}B	16.42	0.330	0.45	1.10	0.283	3.1	0.90
	^{6}Li	16.32	0.345	0.45	1.10	0.106	2.5	0.60
18.0	^{12}C	14.32	0.164	0.58	1.12	0.109	2.0	0.20
	B_4C	15.00	0.159	0.58	1.12	.0437	2.6	0.45
	^{10}B	15.00	0.159	0.58	1.12	.082	3.3	0.84
	^{6}Li	15.6	0.164	0.58	1.12	0.0291	2.6	0.42
26	^{12}C	17.08	0.500	0.82	1.11	0.0135	2	0.30
	B_4C	16.98	0.218	0.82	1.11	0.054	3.4	0.50
	^{10}B	16.98	0.218	0.82	1.11	0.0101	3.3	1.25
	^{6}Li	17.52	0.220	0.82	1.11	0.00325	2.6	0.70

Table 5.4: Cross-section results for carbon, lithium, and boron at 30° to 55.5°

Angle [^{0}]	Target	t [mins]	I [μA]	$q_{eff}[fm^{-1}]$	R	σ [fm^2/sr]	Sys [%]	Stat [%]
30	^{12}C	30.58	0.491	0.95	1.13	4.24×10^{-3}	2.0	0.30
	B_4C	19.38	0.218	0.95	1.13	1.91×10^{-2}	2.6	0.58
	^{10}B	19.38	0.218	0.95	1.13	3.71×10^{-3}	3.3	1.16
	^{6}Li	27.40	0.219	0.95	1.13	1.20×10^{-3}	2.6	0.85
39	^{12}C	20.58	3.228	1.24	1.13	2.95×10^{-4}	2.0	0.40
	B_4C	17.88	1.225	1.24	1.13	1.73×10^{-3}	2.7	0.51
	^{10}B	17.88	1.225	1.24	1.13	3.58×10^{-4}	3.4	1.47
	^{6}Li	18.31	2.110	1.24	1.13	1.31×10^{-4}	2.7	1.04
46	^{12}C	24.97	19.49	1.44	1.08	3.43×10^{-5}	2.0	0.40
	B_4C	19.13	4.75	1.44	1.08	3.19×10^{-4}	2.8	0.78
	^{10}B	19.13	4.75	1.44	1.08	7.13×10^{-5}	3.4	1.59
	^{6}Li	17.17	2.73	1.44	1.08	2.71×10^{-5}	2.8	0.92
55.5	^{12}C	56.80	9.94	1.70	1.11	6.08×10^{-7}	2.0	3.00
	B_4C	57.12	3.38	1.70	1.10	3.29×10^{-5}	2.8	5.80
	^{10}B	57.12	3.38	1.70	1.11	8.9×10^{-6}	3.5	12.0
	^{6}Li	59.94	3.97	1.70	1.11	3.67×10^{-6}	2.8	4.50

Table 5.5: Cross-section results for Carbon, Lithium, and Boron at 61° and 66°.

Angle [^{0}]	Target	t [mins]	I [μA]	$q_{eff}[fm^{-1}]$	R	σ [fm^2/sr]	Sys [%]	Stat [%]
61	^{12}C	49.92	9.82	1.85	1.1	3.26×10^{-8}	3.5	7.7
	^{6}Li	44.22	3.99	1.85	1.1	9.62×10^{-7}	3.1	9.7
66	^{12}C	46.5	10.02	2.01	1.12	1.33×10^{-7}	3.5	5.1
	B_4C	40.54	4.00	2.01	1.12	4.93×10^{-6}	4.4	7.0
	^{10}B	40.54	4.00	2.01	1.12	1.20×10^{-6}	3.5	15.8

In Fig. 5.5 we present the cross sections for these three targets along with a previous parametrization of carbon data by Offerman [52].

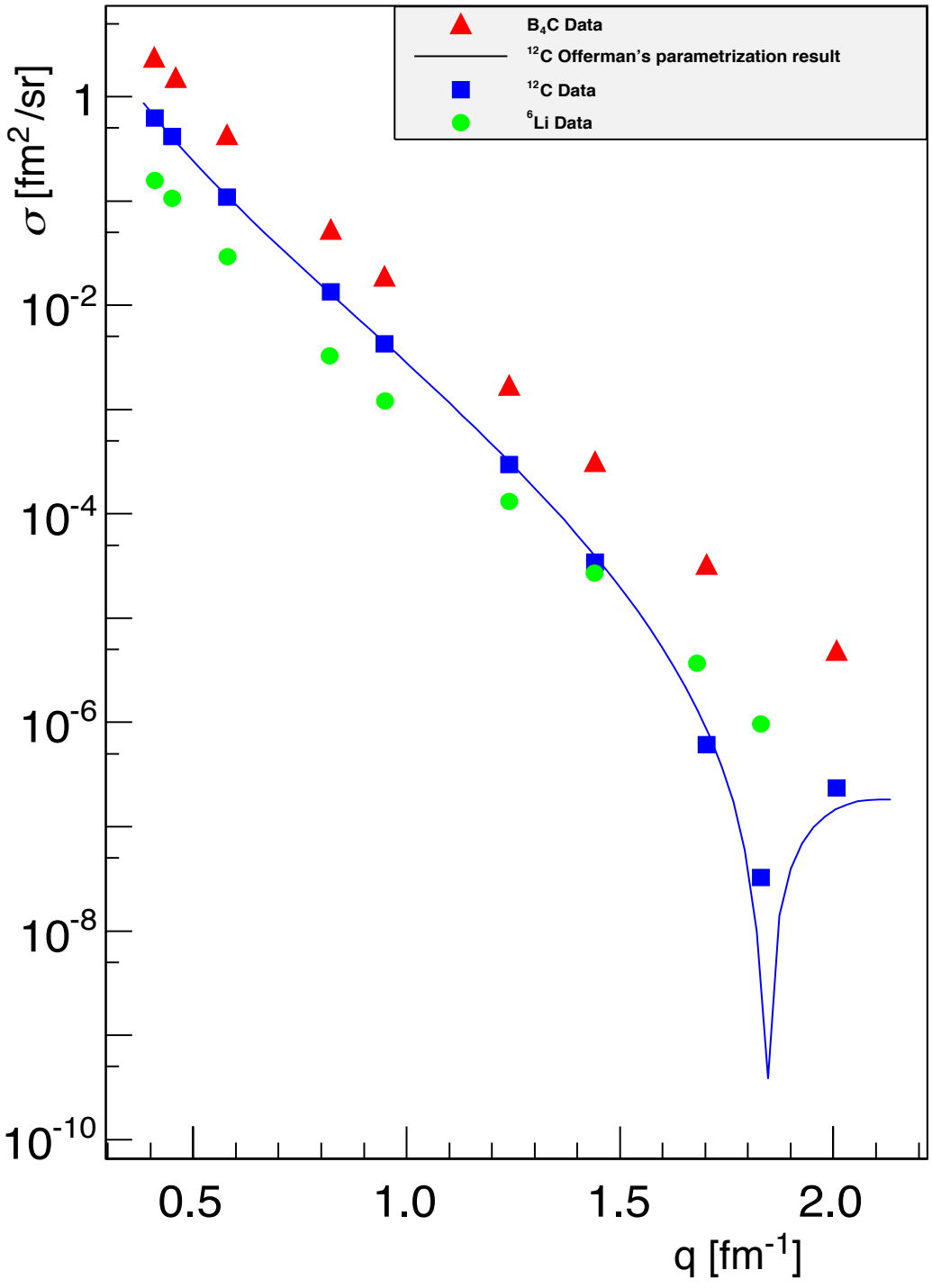

Fig. 5.5: Cross-section results for Carbon, Boron and Lithium.

Chapter 6

FORM FACTORS, PARAMETRIZATION, AND CHARGE RADII

6.1 Fourier-Bessel Parametrization Technique and Charge Radii

As mentioned in Section 1.4, in the Born approximation, the square of the form factor for a spin-zero nucleus is equal to the ratio of the differential scattering cross section to the Mott cross section. We know also that, at low momentum transfer, the form factor can be written as a Fourier transform of the charge distribution function, as in equation 1.9. Now, if we consider the fact that a realistic charge distribution will vanish aftera certain point in space, or at the cut-off radius (R), Eq. 1.9 can be rewritten as,

$$F(q) = \frac{1}{Z}\int_0^R \rho(r)\frac{\sin(q.r)}{qr}4\pi r^2 dr. \tag{6.1}$$

Again, a realistic nuclear charge distribution should be single valued, continuous, square integrable, and should have a finite no. of maxima and minma (Dirichlet conditions). So, the charge distribution function can be expanded as a sum of the zeroth-order spherical Bessel Function of the first kind [53] [54]:

$$\rho(r) = \begin{cases} \sum_{\nu=1}^{\infty} a_\nu j_0(q_\nu r), & \text{if } r \leq R, \\ 0, & \text{for } r \geq R, \end{cases} \tag{6.2}$$

where, $j_0(q_\nu r) = \frac{\sin(\frac{\nu\pi r}{R})}{\frac{\nu\pi r}{R}}$. At $r = R$, we have the νth root of this spherical Bessel function.

If we insert this expansion of ρ into Eq. 6.1, we can find the coefficients a_ν, given

by [53] ,

$$a_\nu = \frac{q_\nu^2}{2\pi R} F(q_\nu). \tag{6.3}$$

The number of coefficients that one can determine depends on the range of momentum transfers available the experimental cross section and the choice of cut-off radius [52, 54], and goes as,

$$\nu_{\max} = \frac{R q_{\max}}{\pi}. \tag{6.4}$$

For example, if we have data in the momentum transfer range 0.7-3.2 fm^{-1}, we will be able to find only four coefficients with a cut-off radius $R = 8$ fm. However, it can be found in the literature [52–54] that considering a particular form of the form factor outside the experimental range, more coefficients can be found as follows,

$$F(q) \leq c q^{-4} F_p(q), \tag{6.5}$$

where $F_p(q) = exp(-q^2\langle r^2\rangle/6)$, is the folded proton form factor, with $\langle r^2\rangle^{1/2} = 0.86$ being the proton charge radius. And, the constant "c" can be found by matching the envelope of $F(q)$ to the last measured maximum of the form factor.

In our study, we found that the values of the form factor we obtain from this approximation do not match well with the existing world data set. We, therefore, avoid doing approximations of the form factor values as much as possible, and made use of the results from other experiments instead to extend the momentum transfer range.

We verified that this method of finding the coefficients, using Eq. 6.3, works very well in the cases where the form factors are known exactly at the root of the Bessel function. However, in practical situations, the form factors might not be known at these specific locations, which is exactly the case for our experimental points;

therefore, we adopted an alternative approach. In our technique, the form factors do not have to be known exactly at the roots, the knowledge of the values around the root is good enough.

We observed that if we substituted the expression for ρ into Eq. 6.1 and considered the cut-off radius, $R = 8$ fm, we obtained,

$$\begin{aligned} F(q) &= \frac{1}{Z}\int_0^8 \sum_{\nu=1}^{\infty} a_\nu \frac{\sin(\frac{\nu\pi r}{8})}{\frac{\nu\pi r}{8}} \frac{\sin(q.r)}{qr} 4\pi r^2 dr \\ &= \frac{32}{Zq}\sum_{\nu=1}^{\infty}\frac{a_\nu}{\nu}\int_0^8 \sin(\frac{\nu\pi r}{8})\sin(qr)dr \\ &= \frac{32}{Zq}\sum_{\nu=1}^{\infty}\frac{a_\nu}{\nu}[-8\frac{[-8qcos(8q)\sin(\nu\pi)+\nu\pi cos(\nu\pi)\sin(8q)]}{\nu^2\pi^2-64q^2}] \\ &= \frac{256\pi}{Zq}\sin(8q)[\frac{a_1}{\pi^2-64q^2}-\frac{a_2}{4\pi^2-64q^2}+\frac{a_3}{9\pi^2-64q^2}-\frac{a_4}{16\pi^2-64q^2}+...]. \end{aligned} \tag{6.6}$$

From the final expression of the form factor above, we can see that if we know the values of $F(q)$ for n different values of q (around the roots), a system of linear equations can be formed. We have solved such a system of equations numerically to find the value of these expansion coefficients. These coefficients in turn allow us to find the charge distribution and the form factors explicitly.

$$\begin{aligned} F(q) &= \frac{1}{Z}\int_0^R \rho(r)\frac{1}{qr}[qr-\frac{(qr)^3}{3!}+\frac{(qr)^5}{5!}]d^3r \\ &= \frac{1}{Z}\int_0^R \rho(r)d^3r - \frac{q^2}{6Z}\int_0^R \rho(r)r^2 d^3r + ... \\ &= 1-\frac{q^2}{6}\langle r^2_{rms}\rangle + ... \\ \therefore \langle r^2_{rms}\rangle &= -6\frac{dF(q)}{dq^2}|_{q\to 0}, \end{aligned} \tag{6.7}$$

here, $\int_0^R \rho(r) d^3r = Z$, and,

$$\frac{1}{Z}\int_0^R \rho(r) r^2 d^3r = \langle r_{rms}^2 \rangle \tag{6.8}$$

.

Since we know the functional form of the form factor and the charge distribution explicitly, the charge radius can be found either by finding the slope of the form factor at $q \to 0$ in accordance with Eq. 6.7, or by taking the second moment of the rms radius in the normalized charge density function Eq. 6.8.

6.1.1 Results for carbon

The cut-off radius for Carbon is choosen to be 8 fm, in accordance with references [52], [53], [54]. The range of momentum transfer available from the LEDEX experiment is, 0.4 to 2.64 fm^{-1}; so, we can determine the first six Fourier-Bessel coefficients with our experimental data. However, we also made use of the available results from previous experiments [52], [55], to find a total of 10 coefficients. Table 6.1 lists all these coefficients with their respective uncertainties.

In determining the coefficients, we allowed values of the form factors to vary randomly, guided by the experimental uncertainties for them. This gives equal footing to all allowable form factors, and guaranties all possible combinations between them. Considering the form factors in this fashion, gives "N" different combinations of coefficients, each coefficient appears N times, after solving the set of linearly independent equations. Then, we find the mean and the standard deviation for each of them.

For carbon, we used the effective momentum transfer in the calculations instead of the momentum transfer; a first order correction to Born approximation [55], expressed as, $q_{eff} = q[1 + \frac{4}{3}\frac{Z\alpha}{E\langle r_{rms}\rangle}]$ and known as the Coloumb correction. The partial-wave analysis that considers coloumb corrections to all order, the plane wave Born

approximation (PWBA) can also be improved. However, this was not implemented here, considering the smallness of the coupling constant, $\alpha \sim 1/137$, which makes the higher-order corrections progressively smaller. It has also been verified before [56] that other than at the diffraction minima, the plane wave approximation does pretty well.

Table 6.1: F-B coefficients for carbon

ν	a_ν	δa_ν
1	0.015846	0.000128
2	0.038330	0.000215
3	0.034325	0.000148
4	0.012775	0.000055
5	−0.004543	0.000051
6	−0.010036	0.000068
7	−0.006306	0.000021
8	−0.002565	0.000062
9	−0.000503	0.000042
10	0.000065	4.9×10^{-7}

As shown in Figs. 6.1 and 6.2 , our parametrizations do remarkably well in describing the cross sections and reduced cross section (σ/σ_{mott}) except at the diffraction minima.

The PWBA predicts diffraction (Fraunhofer type) zeros, the first one being at,

$$qr_{rms} \sim 4.5. \tag{6.9}$$

where, r_{rms} is the root-mean-square value of the radius of the charge distribution. This diffraction phenomena is similar to the scattering of an object with a sharp surface. In reality, we get a diffraction minimum rather than a zero, since the real electron wave is distorted. From Eq. 6.9, it is also clear that the knowledge of the location of the diffraction minimum also tells us the approximate size of the scattering nucleus [30]. In our analysis we find a diffraction minimum at $q(q_{eff}) \sim 1.82(1.84)\text{fm}^{-1}$, and so for the carbon nucleus we obtain a radius of 2.47 fm.

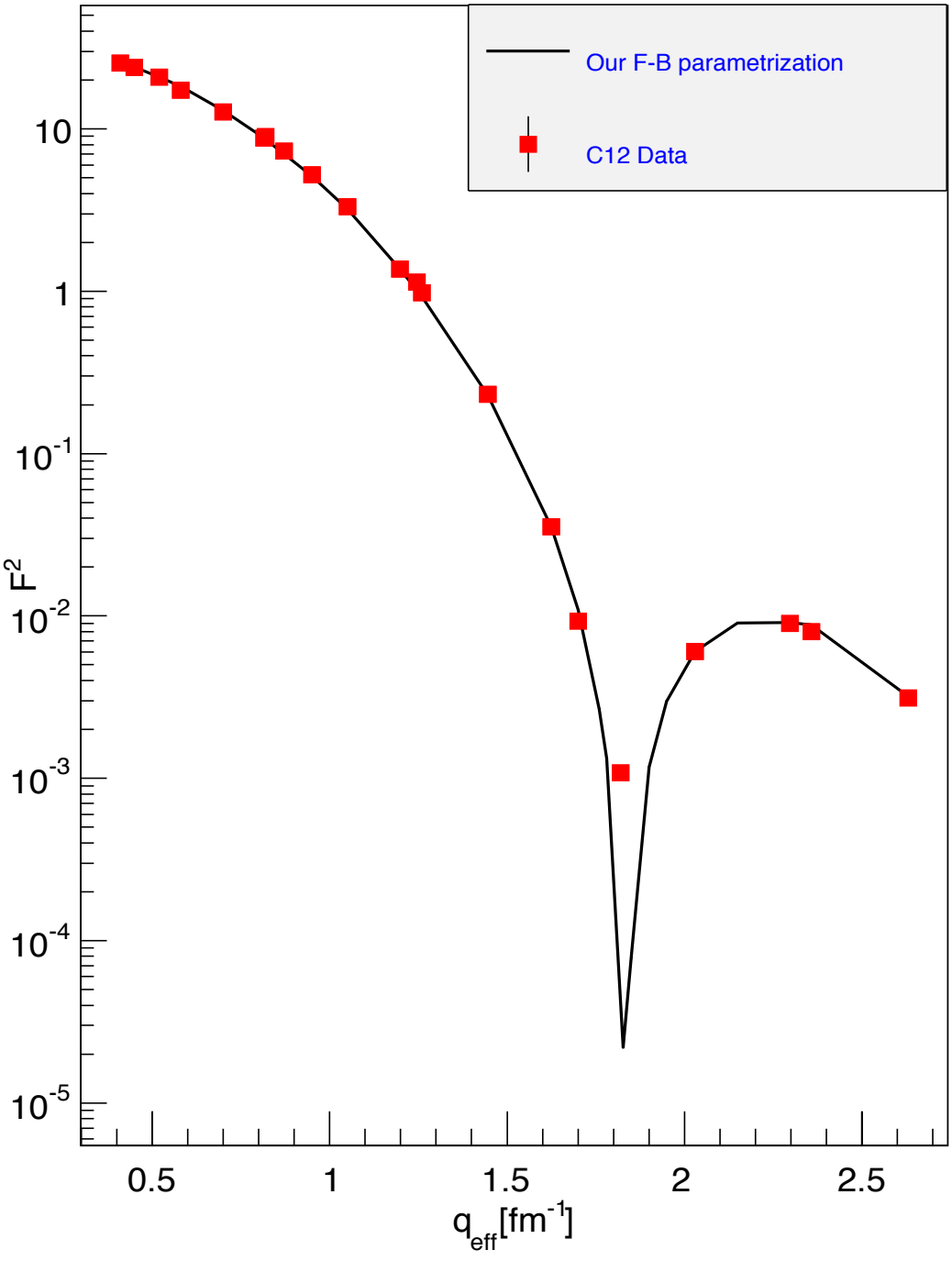

Fig. 6.1: Comparison between the experimental values of reduced cross section and the results obtained via the Fourier-Bessel analysis.

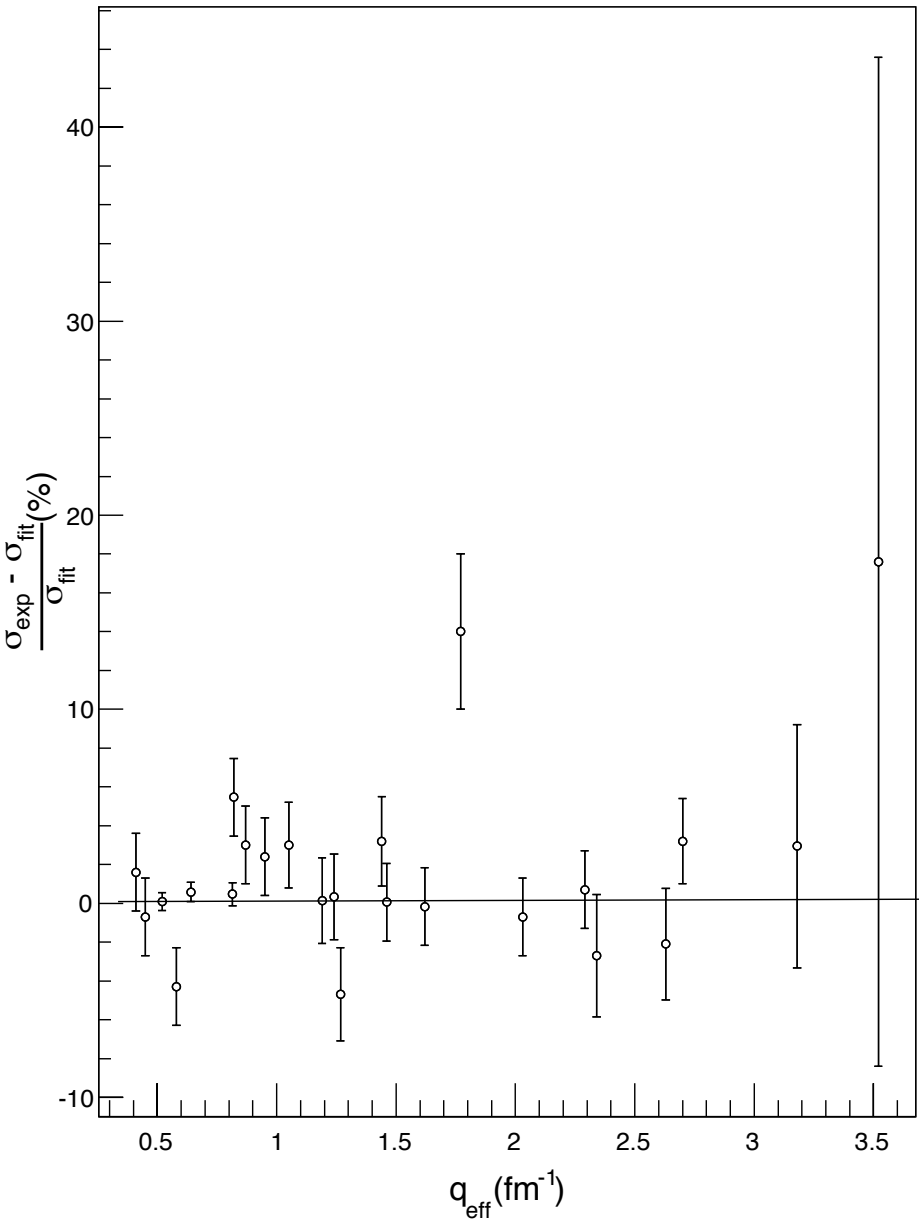

Fig. 6.2: The percentage deviation between the experimental cross section and the fit results. Avoiding the points around the diffraction minima we get, $\frac{\chi^2}{N} = 1.12$.

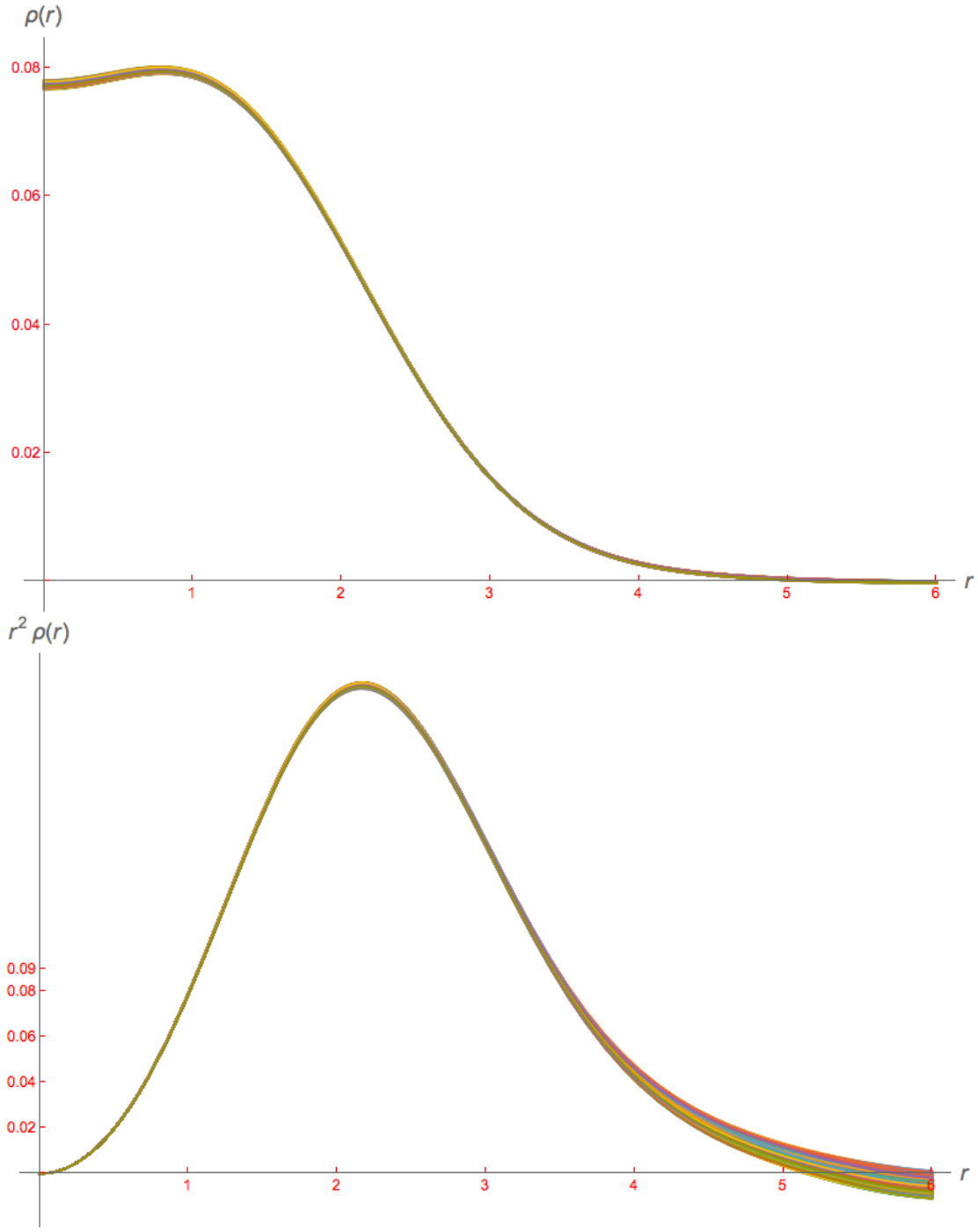

Fig. 6.3: Charge distribution for ^{12}C. In the second picture a factor of r^2 is multiplied with the charge density to emphasize the nuclear surface and tail region.

Figure 6.3 shows the charge distrbution of the carbon nucleus. Different colors of

the diagram corresponds to N different sets of coefficients we evaluated by a random number generation technique. The shape of the charge distribution tells us a few features about the carbon nucleus. The dip at the centre and buldge at the surface says that the nucleons reside more on the surface than at the center. The shape of the carbon nucleus is not a perfect sphere with uniform density.

In determining the charge radius we use the definition of charge radius in Eq. 6.8. We have found the charge radius with all sets of coefficients, which is then averaged to find the mean and standard deviation. The reulting charge radius for carbon is,

$$\langle r_{rms} \rangle = 2.45 \pm 0.09\text{fm}.$$

The result is illustrated in Fig. 6.4 . The error on our result looks large compared to the established result for carbon; hence, we put our method of finding the error to a test by considering the uncertainties from the best (every quantity was meticulously measured, calibrated and controlled) elastic scattering experiment ever done, by Larry Cardman *et al.*, at the National Bureau of Standards Linac Facility [57]. With our technique, we get within 20% of the uncertainty quoted in their paper. This discrepency can be explained by considering the difference between our and Cardman's method for determining the error. Cardman considers the nominal and the values at the systematic extremes of the form factors and finds the charge radius for each case, and consequently sees the spread in the charge radius value. We, on the other hand, use the nominal and extremum values and consider also the intermediate values between the extremum as well.

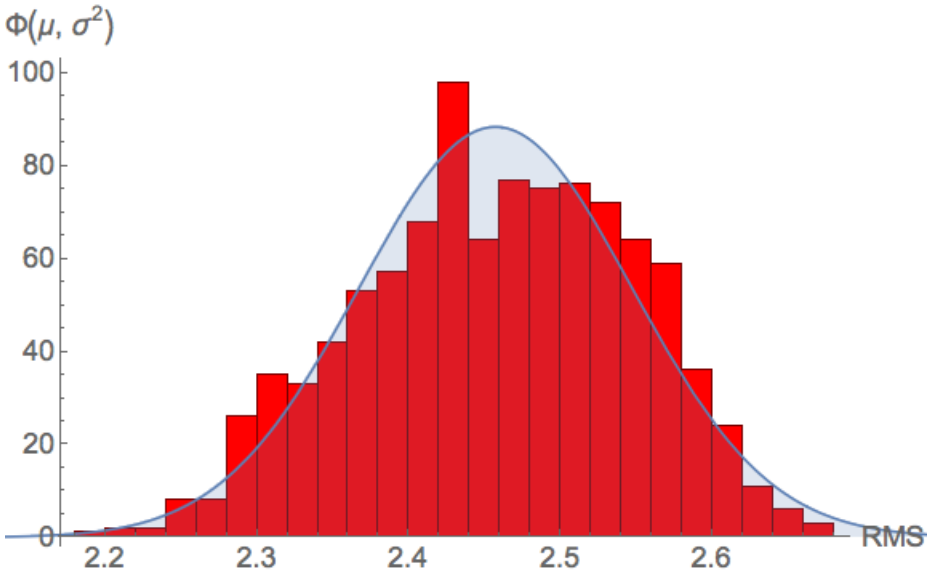

Fig. 6.4: Distribution of the charge radius for carbon.

6.1.2 F-B Parametrization of the Form Factor and Charge Radius Result for Boron (^{10}B)

The nuclear spin of ^{10}B is 3 and the formula for the differential elastic scattering cross-section is given by [21],

$$\sigma = \sigma_{\text{Mott}}[F_{ch}^2(q) + \frac{1}{2}(1 + 2\tan^2\frac{\theta}{2})F_{mag}^2]. \tag{6.10}$$

Thus, the cross-section formulation has both magnetic and charge contributions. The usual method of finding the magnetic contribution is to perform the experiment at very large angles (e.g., 180°) and vary the beam energy so that all contributions in Eq. 6.10 become entirely magnetic, but at the same momentum transfer as its low angle counterpart. Since there is no such set-up in our experiment, we cannot find the magnetic contribution explicitly from the experimental data. However, here we have estimated the magnetic contribution by calculating the ratio of the strength of

the magnetic to the electric interaction using,

$$(\frac{q\mu}{eZ})^2 = (\frac{q}{2m}\frac{\mu/\mu_N}{Z})^2, \tag{6.11}$$

which is argued to be very good estimate in ref. [58]. Here, Z is the nuclear charge, μ is the magnetic moment,and μ_N is the nuclear magneton. In table 6.2 esimates of magnetic contribution to the total scattering cross-section for boron is given.

Table 6.2: Approximation for the magnetic scattering contribution.

q_{eff} [fm^{-1}]	σ_{observed}[fm^2/sr]	$(\frac{q\mu}{eZ})^2$	$\sigma_{\text{corrected}}$[fm^2/sr]	F_E^2	Syst. (%)	Stat. (%)
0 .41	0.445	0.00024	0.4448	18.16	3.1	0.69
0.45	0.283	0.00029	0.2829	16.17	3.1	0.90
0.58	0.082	0.00048	0.0819	13.25	3.3	0.84
0.82	0.0101	0.00096	0.0100	6.83	3.3	1.25
0.95	3.71×10^{-3}	0.00129	3.705×10^{-3}	4.50	3.3	1.16
1.24	3.58×10^{-4}	0.00220	3.57×10^{-4}	1.28	3.4	1.47
1.44	7.13×10^{-5}	0.00290	7.10×10^{-5}	0.492	3.4	1.59
1.71	8.90×10^{-6}	0.00414	8.60×10^{-6}	0.134	3.5	12.00
2.0	1.20×10^{-6}	0.00574	1.20×10^{-6}	0.0377	3.5	15.81

As can be seen from Table 6.2, the magnetic correction for boron is very small and can be safely neglected. To calculate the Fourier Bessel coefficients we have

used the high momentum transfer results (where we do not have any data from our experiment) at first from [21]. But, uncertainties in the form factors quoted at these points were found to be high and using these results to calculate the F-B coefficients ended up with unwanted oscillations at the tail of the charge density function. Next, the form factor values were approximated from Eq. 6.5 at high momentum transfers and a new set of F-B coefficients are evaluated (table 6.3). This latter treatment seems to stabilize the tails; hence, we stick to this approximation. In total we calculated nine F-B coefficients and the cut-off radius is taken to be 8 fm for this particular target.

Table 6.3: F-B coefficients for Boron

ν	a_ν	δa_ν
1	0.0133	8.53×10^{-5}
2	0.0336	3.03×10^{-4}
3	0.0358	2.53×10^{-4}
4	0.0254	5.44×10^{-4}
5	0.0155	4.63×10^{-4}
6	0.0090	3.823×10^{-5}
7	0.0052	8.52×10^{-5}
8	0.0030	5.67×10^{-6}
9	0.0017	9.38×10^{-6}

Figs. 6.5 and 6.6 show the comparison between the experimental results with the results obtained from the F-B analysis. The reduced χ^2 value in our experimental

range is 0.73.

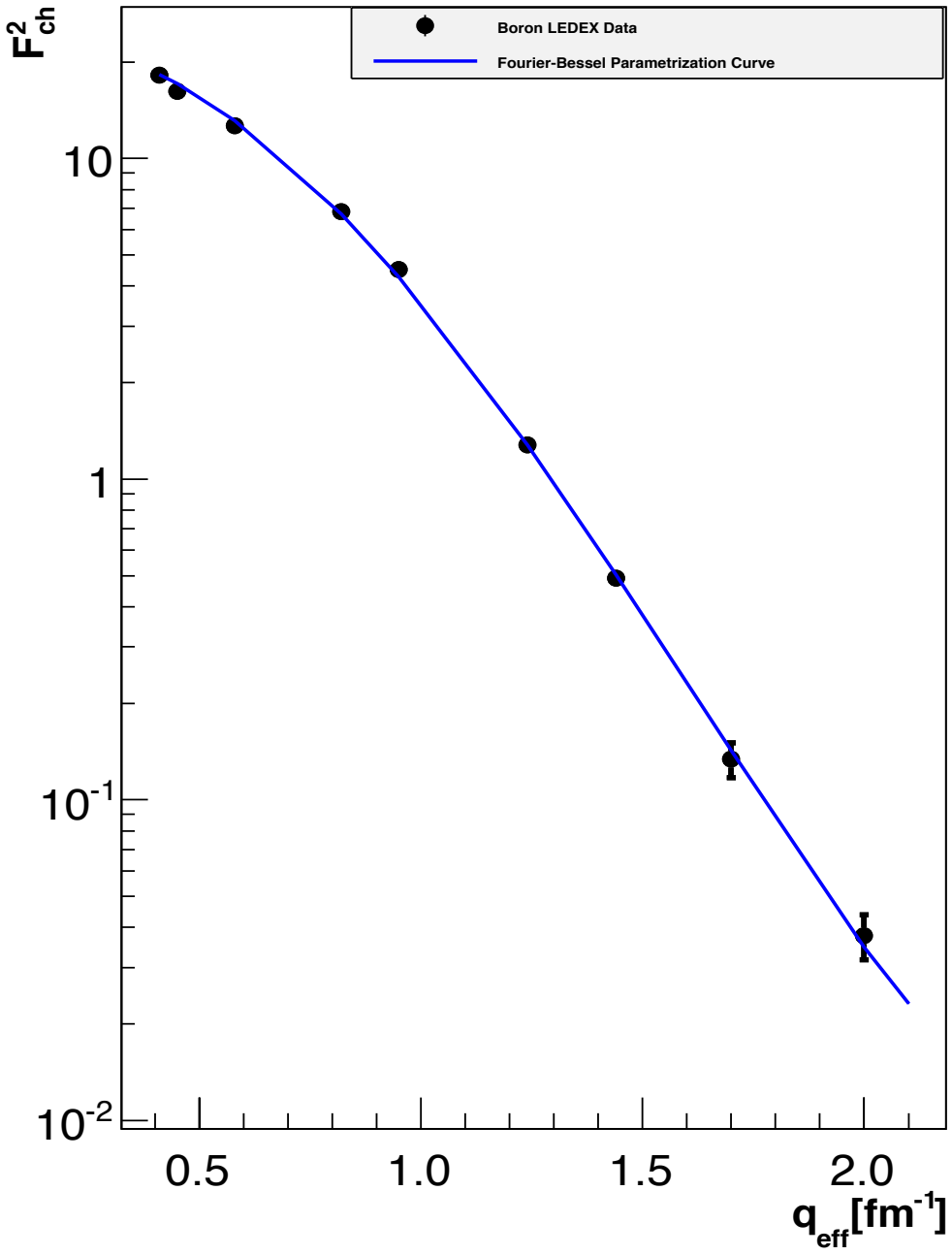

Fig. 6.5: F-B parametrization results for the form factors of boron.

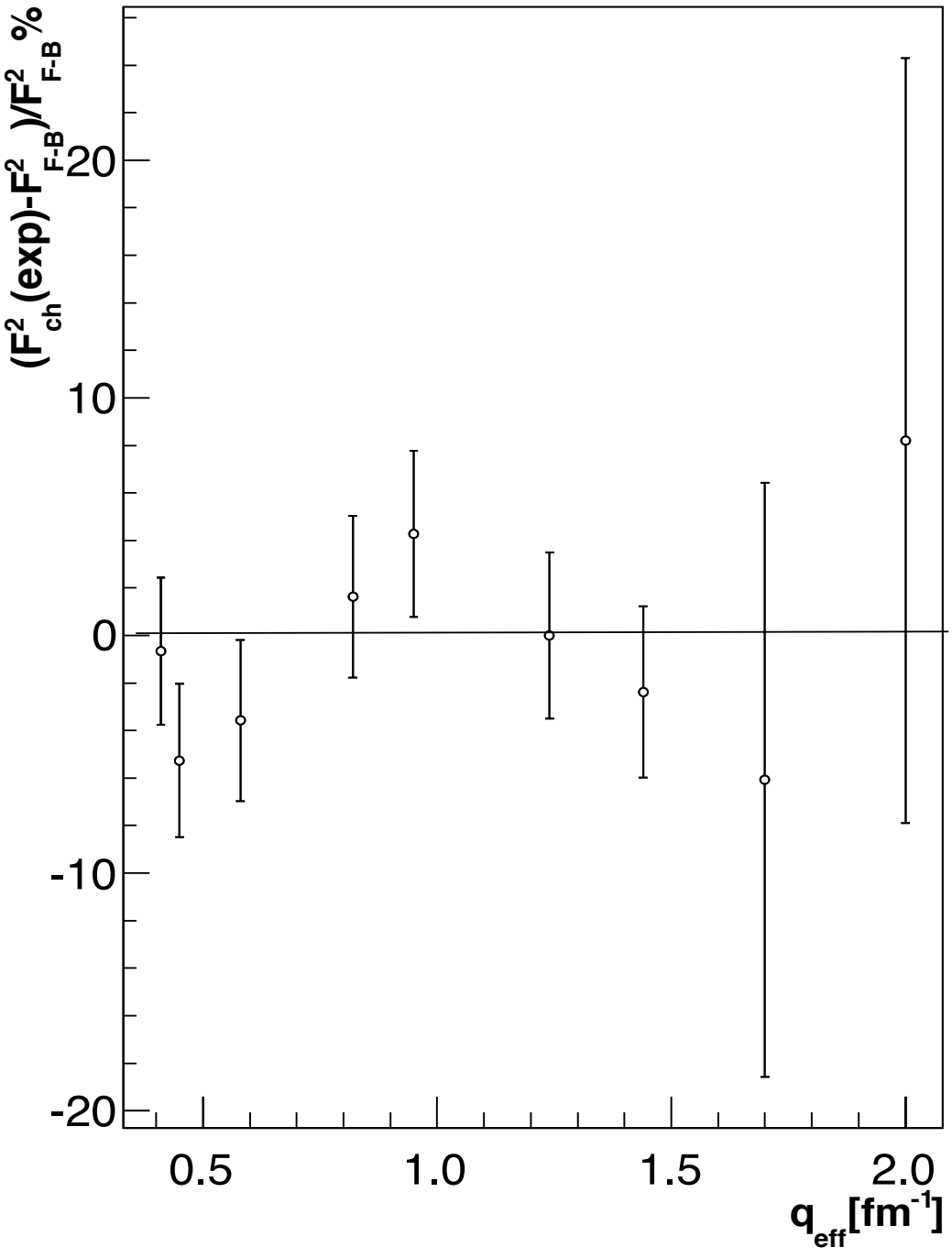

Fig. 6.6: Percentage deviation of the experimental form factors from the F-B parametrization results for boron.

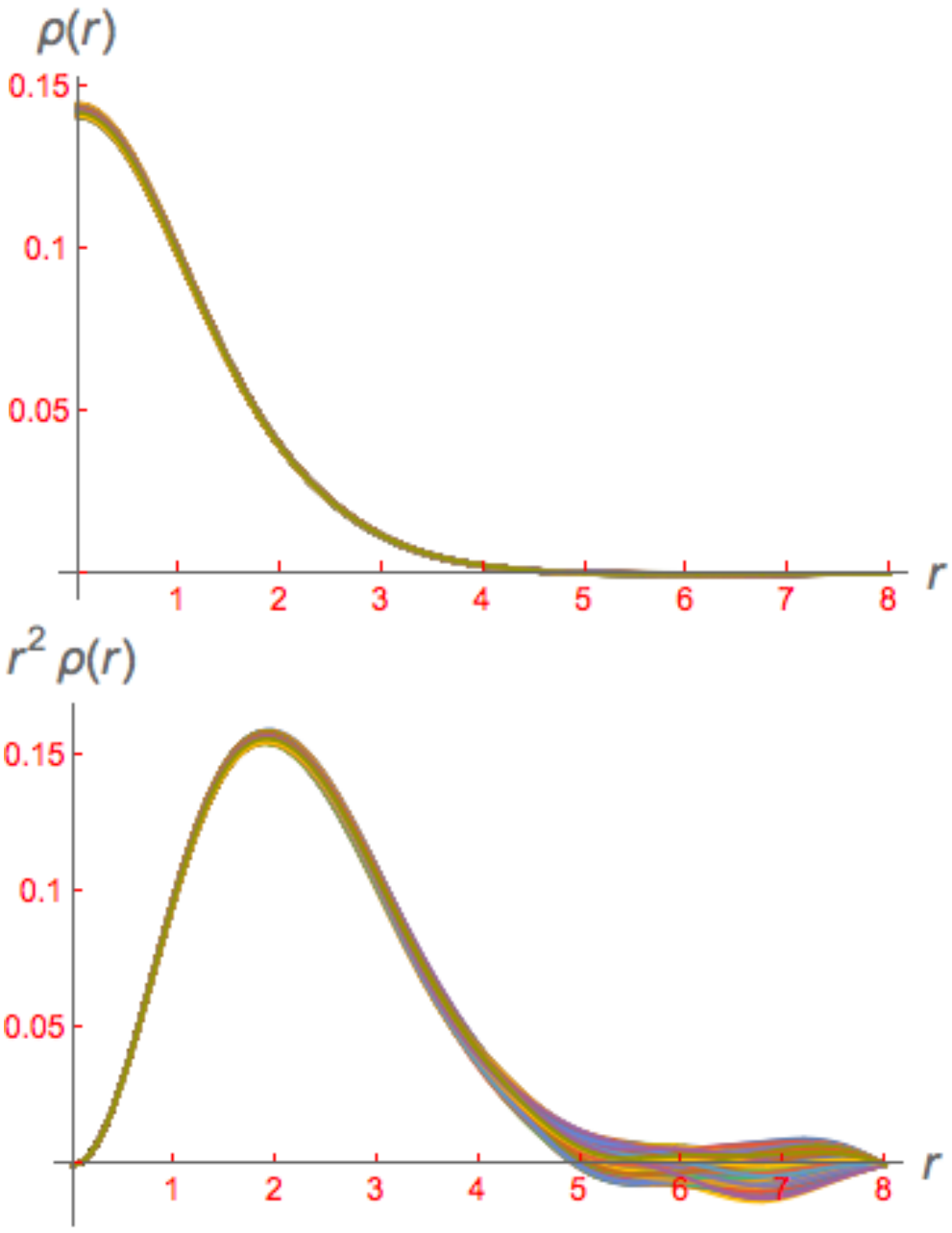

Fig. 6.7: The charge distribution function for boron, obtained from F-B analysis. r^2 is multiplied with the charge density in the bottom picture to emphasize the nuclear surface and tail region

The charge density has small oscillations at the tail, but these oscillations average to zero, as can be seen in Fig. 6.7. We found that changing the cut-off radius does not change the normalization and the charge radius very much, but it changes the

uncertainty in the result (Table 6.4). This is expected as the higher cut-off radius keeps larger variations in the outcomes of the results.

Table 6.4: Cut-off dependence of charge radius for boron.

R_{cut} [fm^{-1}]	$\int_0^{R_{cut}} \rho(r) d^3r$	$\langle r_{rms} \rangle$ [fm]	$\delta\langle r_{rms} \rangle$ [fm]
5	5.051	2.444	0.014
5.5	5.066	2.456	0.026
6	5.065	2.455	0.042
7	5.043	2.418	0.087
8	5.047	2.425	0.122

Using the full cut off radius $R_{cut} = 8$ fm, the charge radius of boron is,

$$\langle r_{rms} \rangle = 2.425 \pm 0.122\text{fm}$$

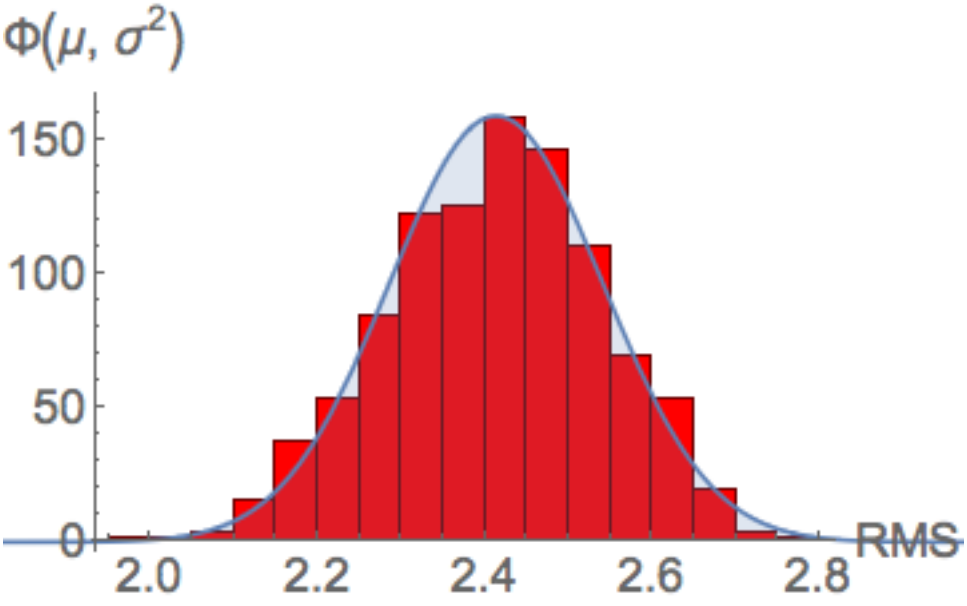

Fig. 6.8: Distribution of boron's charge radius.

6.1.3 F-B Parametrization of the Form Factor and Charge Radius Result for Lithium(^{6} Li)

The elastic scattering cross section for lithium is

$$\frac{\sigma}{\sigma_{mott}} = [A(q) + B(q)tan^2\frac{\theta}{2}], \tag{6.12}$$

where, $A(q) = G_C^2 + \frac{2}{3}\tau G_M^2 + \frac{8}{9}\tau^2 G_Q^2$ and $B(q) = \frac{4}{3}\tau(1+\tau)G_M^2$; thus, the cross section has contributions from charge monopole, magnetic dipole, and electric quadrupole terms. From Eq. 6.11, we find that the highest magnetic contribution in this experimental set up is ∼0.3% , but since we have an experimental uncertainty of ∼10% at this point, we have ignored the magnetic contribution for lithium in our study. The quadrupole contribution is also expected to be negligible [22], so we consider the total reduced cross section to extract the charge form factor here. Table 6.5 summarizes the results for the lithium cross sections and form factors.

Table 6.5: Experimental form-factor results for ^{6}Li.

q_{eff} [fm^{-1}]	σ[fm^2/sr]	F_{ch}^2	Syst. (%)	Stat. (%)
0.41	1.57×10^{-1}	6.41	2.5	0.78
0.45	1.06×10^{-1}	6.07	2.5	0.60
0.58	2.91×10^{-2}	4.49	2.6	0.42
0.82	3.25×10^{-3}	2.22	2.6	0.70
0.95	1.20×10^{-3}	1.46	2.6	0.85
1.24	1.31×10^{-4}	0.47	2.7	1.04
1.44	2.71×10^{-5}	0.188	2.8	1.04
1.68	3.67×10^{-6}	0.0557	2.8	4.50
1.83	9.62×10^{-7}	0.0217	3.1	9.70

For lithium. we have form-factor values up to 1.83 fm^{-1} of momentum transfer. The form factor values beyond 1.83 fm^{-1} is taken from [22], to calculate a complete set of F-B coefficients. The cut-off radius for lithium is taken at 6 fm and a total of 7 coefficients are found, which are shown in Table 6.6. One of the pitfalls of taking the form-factor values at the higher momentum transfers from this reference is that the uncertainties on the cross section values are many times higher than the typical uncertainty of the 'LEDEX' experiment, which eventually increases the uncertainty on the charge radius result. However, the the first few coefficients ($a_1 ... a_4$) that are associated with the low-momentum transfer are most dominant (these set up the scale) in the Fourier-Bessel series. So, the charge radius value and its error are not impacted greatly by these higher-order coefficients.

Table 6.6: F-B coefficients for lithium

ν	a_ν	δa_ν
1	0.01635	0.00015
2	0.02960	0.00025
3	0.02081	0.00025
4	0.00727	0.00025
5	0.00048	0.00022
6	−0.00088	0.00008
7	0.00114	0.00004

Figures 6.9 and 6.10 compare the experimental results with the fits obtained from the F-B analysis. The reduced χ^2 value in our experimental range is 1.16.

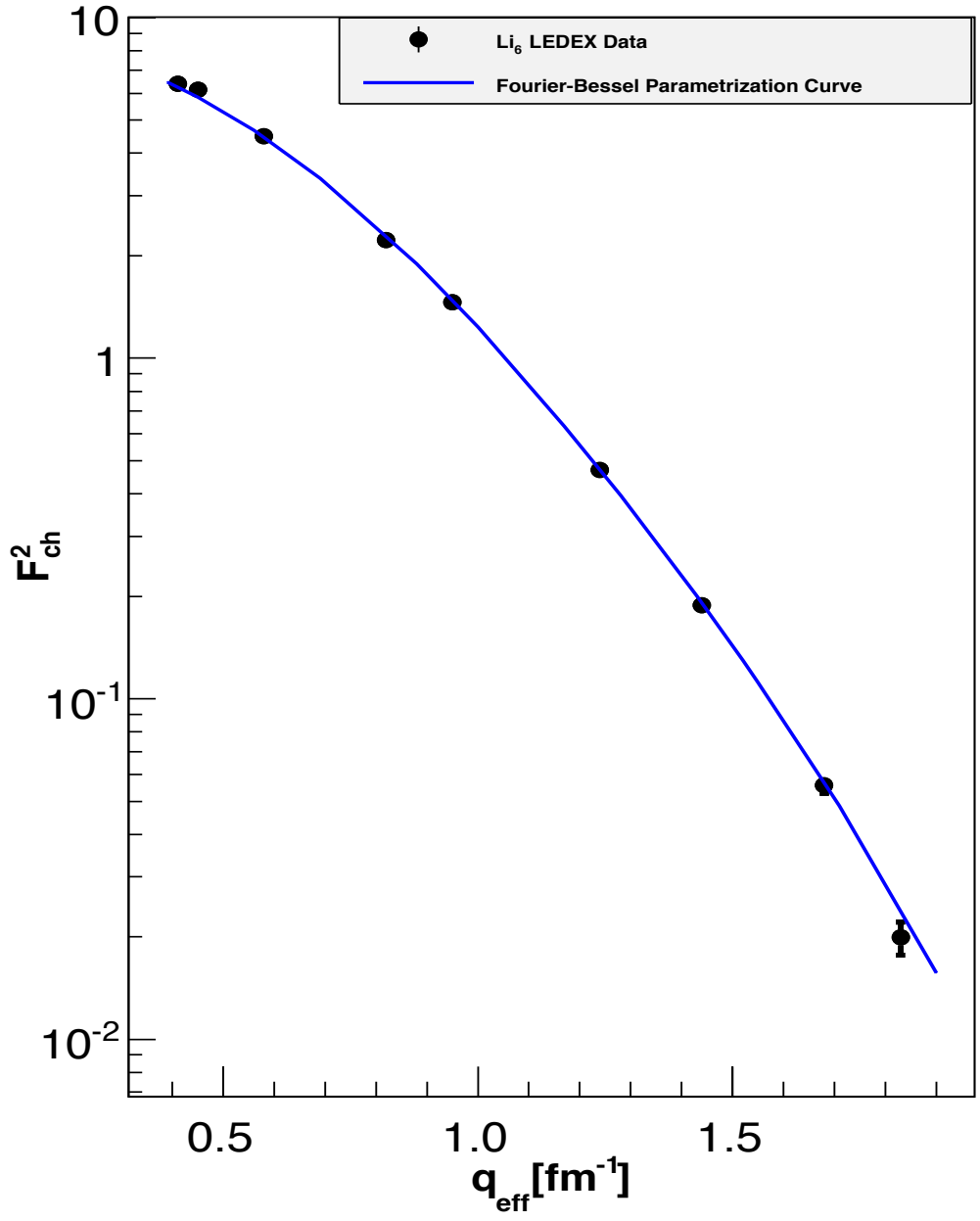

Fig. 6.9: F-B parametrization for the form factors of lithium.

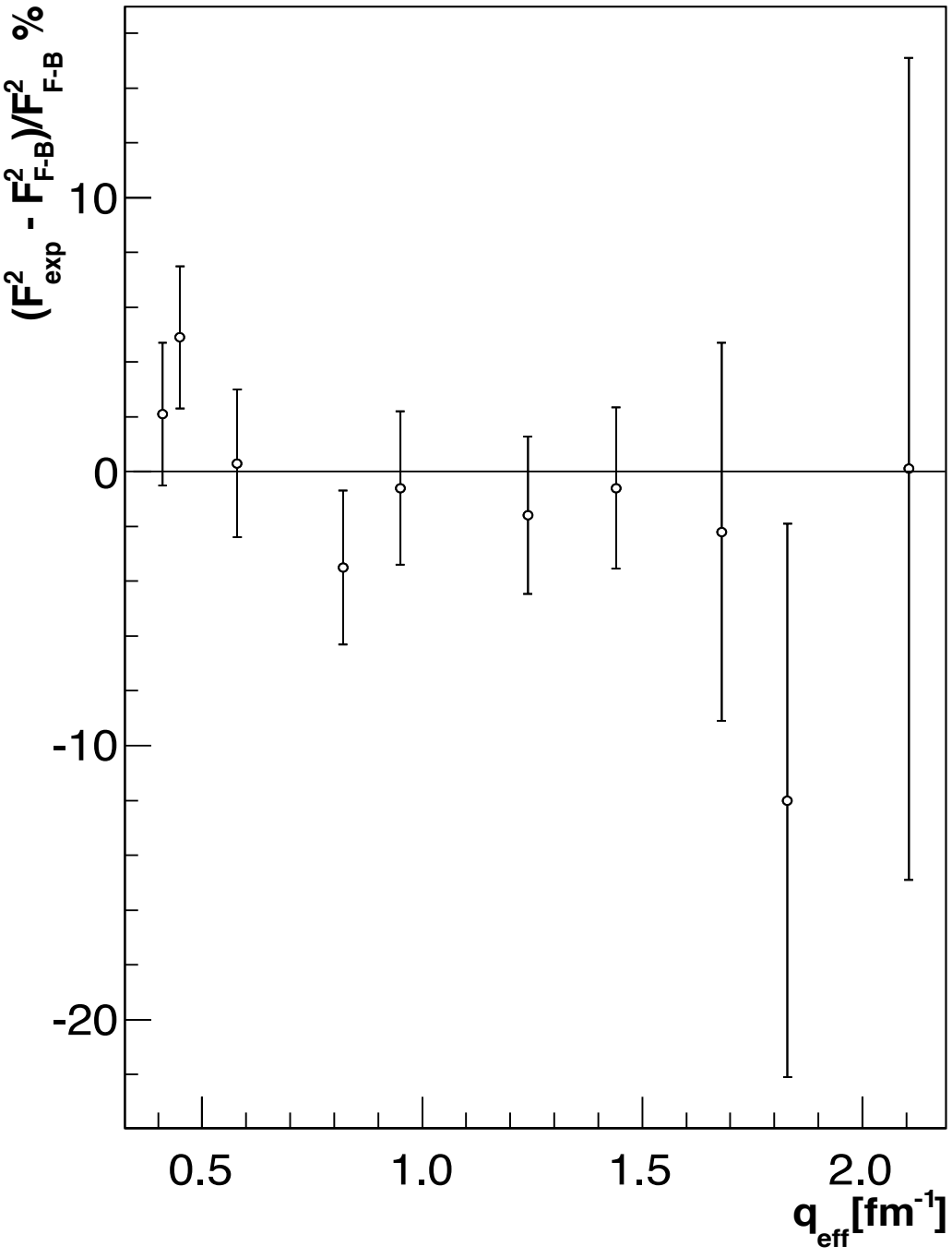

Fig. 6.10: Percentage deviation of the experimental form factors from the F-B parametrization results for lithium.

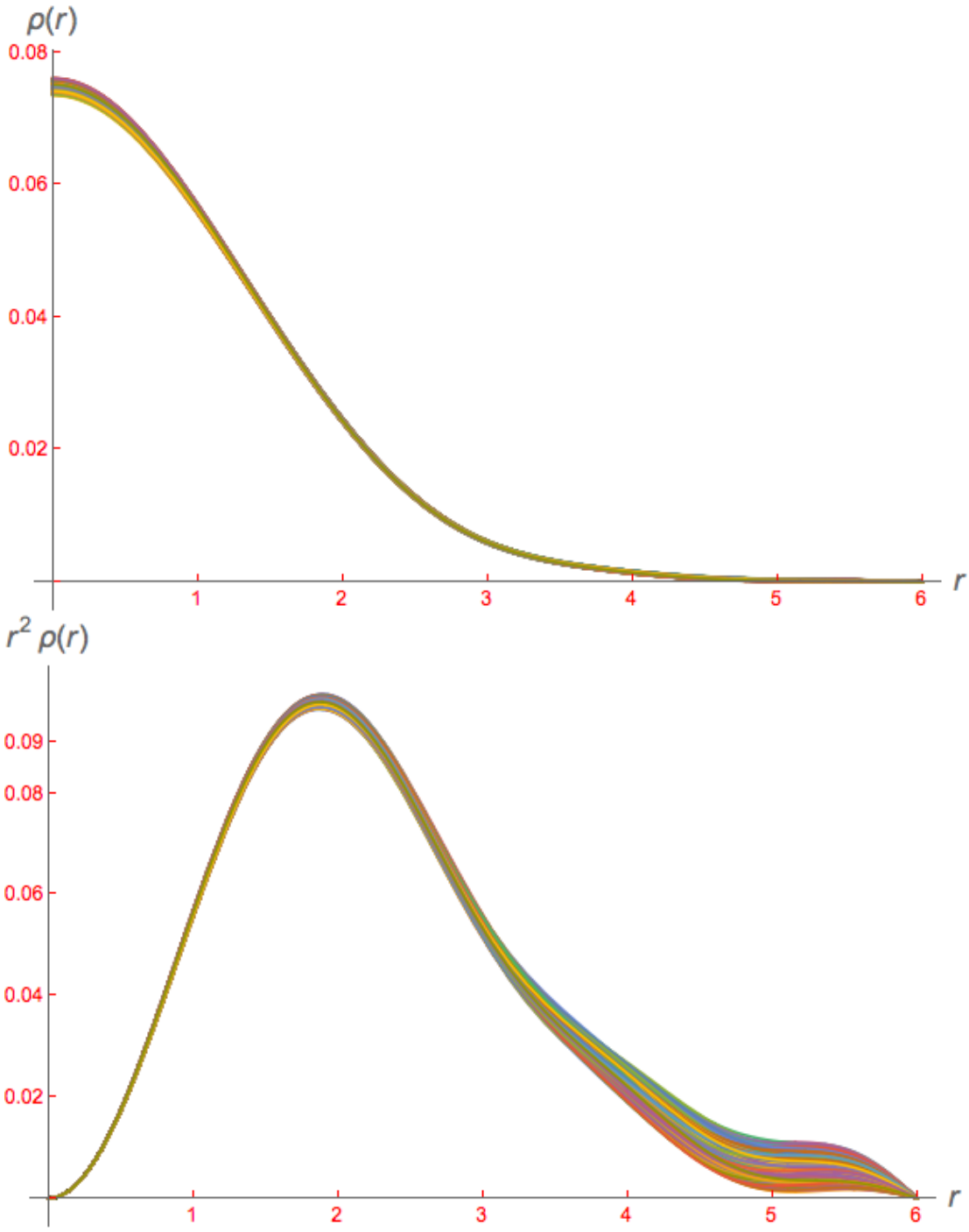

Fig. 6.11: Top diagram is for lithium's charge distribution obtained from F-B analysis. r^2 is multiplied with the charge density in the bottom picture to emphasize the nuclear surface and tail region

The charge density distribution function (Fig. 6.11) for lithium was found to be very stable (no tail oscillation) and it resembles a perfect gaussian distribution. Using this charge density function and Eq. 6.8, we found the charge radius of lithium to be

$$\langle r_{rms} \rangle = 2.519 \pm 0.048\,\text{fm}.$$

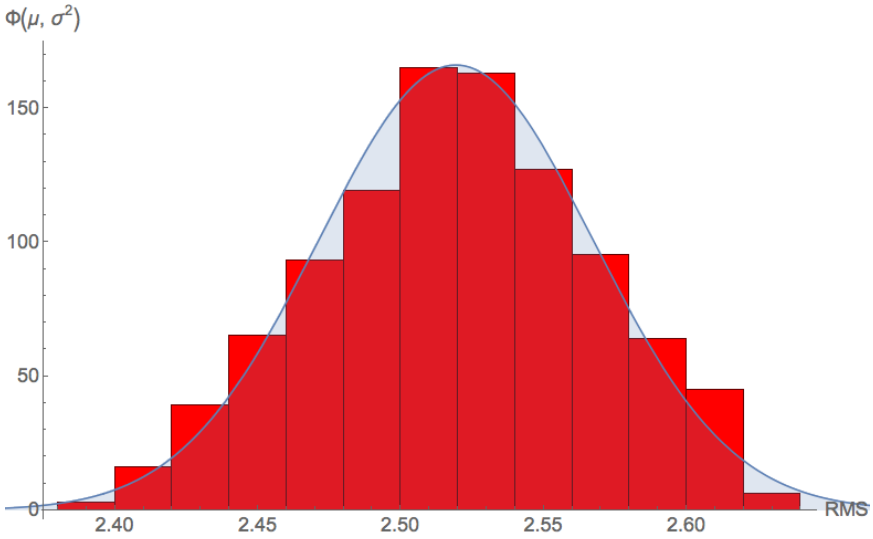

Fig. 6.12: Distribution of lithium's charge radius.

6.1.4 Deuterium Results

The nuclear spin of deuterium is one, so the formula for its differential scatteriing cross section is same as for lithium. Here, we call the charge monopole and quadrupole terms combined as the electric form factor (F_E). It is customary to separate the quadrupole term and the monopole term, but, it was not done here for two reasons. The quadrupole term is coupled to the monopole term by τ^2, with a maximum value of 0.000475 in this experimental set-up. Hence, this separation, which is very complicated for these unpolarized measurements, is avoided.

On the other hand, the magnetic contribution is coupled via τ in $A(q)$. Thus, its contribution will be many times higher than the quadrupole term. However, the

main objective of this experiment is to determine the $A(q)$ structure function, so the experiment was performed at smaller angles only, such that the term $B(q)$ becomes insignificant because of its coupling with the $\tan^2\frac{\theta}{2}$ factor; we do not have 180° measurements that could determine the magnetic contributions. So, we again have estimated the magnetic contribution using Eq. 6.11.

It can be seen from Table 6.7 that the magnetic contribution to the cross section increases with momentum transfer and rises as much as 6% at the highest angle setting.

Table 6.7: Approximation for the magnetic scattering contribution .

q	$\sigma_{\text{observed}}[\text{fm}^2/\text{sr}]$	$(\frac{q\mu}{eZ})^2$	$\sigma_{\text{corrected}}[\text{fm}^2/\text{sr}]$	F_E
0 .87	$(1.72 \pm 0.05) \times 10^{-3}$	0.0061	$(1.71 \pm 0.05) \times 10^{-3}$	0.630 ± 0.008
1.02	$(6.86 \pm 0.18) \times 10^{-4}$	0.0084	$(6.80 \pm 0.180) \times 10^{-4}$	0.548 ± 0.007
1.26	$(1.67 \pm 0.04) \times 10^{-4}$	0.0128	$(1.65 \pm 0.035) \times 10^{-4}$	0.420 ± 0.005
1.44	$(6.72 \pm 0.15) \times 10^{-5}$	0.0168	$(6.60 \pm 0.142) \times 10^{-5}$	0.35 ± 0.004
1.78	$(1.16 \pm 0.03) \times 10^{-5}$	0.0257	$(1.13 \pm 0.025) \times 10^{-5}$	$0.225 \pm .003$
2.28	$(1.13 \pm 0.02) \times 10^{-6}$	0.0422	$(1.076 \pm 0.023) \times 10^{-6}$	0.123 ± 0.001
2.51	$(4.23 \pm 0.10) \times 10^{-7}$	0.0511	$(4.01 \pm 0.092) \times 10^{-7}$	0.094 ± 0.001
2.79	$(1.03 \pm 0.03) \times 10^{-7}$	0.0630	$(0.97 \pm 0.025) \times 10^{-7}$	0.060 ± 0.001

Having found the electric form factors for deuteron, we then parametrize these by the Fourier-Bessel technique. The cut-off radius for this case is taken as 6 fm and

a total of seven Fourier-Bessel coefficients was determined. The choice of the cut-off radius forced us to pick three form factor values from [59] and [60]. The values of the coefficients (a_ν) and their respective uncertainties (δa_ν) is tabulated in Table 6.8:

Table 6.8: F-B coefficients for deuterium

ν	a_ν	δa_ν
1	5.96×10^{-3}	2.2×10^{-5}
2	1.56×10^{-2}	8.1×10^{-5}
3	1.93×10^{-2}	1.1×10^{-4}
4	1.72×10^{-2}	7.2×10^{-5}
5	1.49×10^{-2}	1.1×10^{-4}
6	1.08×10^{-2}	1.1×10^{-4}
7	8.49×10^{-3}	8.8×10^{-5}

The next diagram [Fig.6.15] shows the resulting nuclear charge distribution function for the deuteron. The shape of the charge distribution function is gaussian like, with a few oscillations at the tail. However, this osclillation is very small and noticeable only when it is superficially enlarged by multiplying $\rho(r)$ by a r^2 factor. Also, this oscillation does not disrupt the charge radius extraction process.

Figures 6.13 and 6.14 show how well our parametrization model describes the experimental electric form factor values In Fig. 6.14, three additional points, one at

the very begining and two at the end, from previous experiments were utilized to find the full set of Fourier-Bessel coefficients. The reduced χ^2 value with these points is 1.93. The departure from the ideal value of unity is mostly dominated by our last experimental point (at 2.79 fm^{-1}). If we exclude this point, the χ^2 value immediately drops closer to 1.

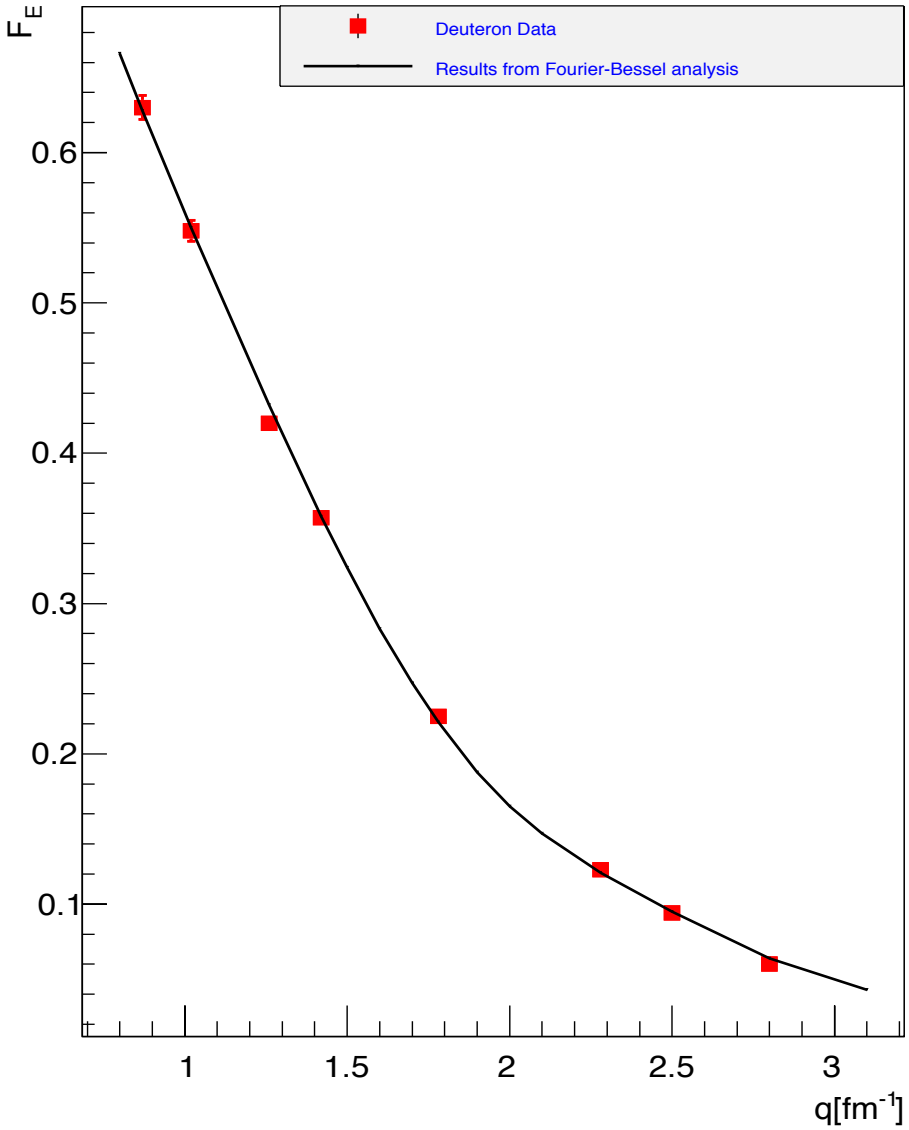

Fig. 6.13: Comparison between the experimental electric form factor and the F-B parametrization curve for the deuteron.

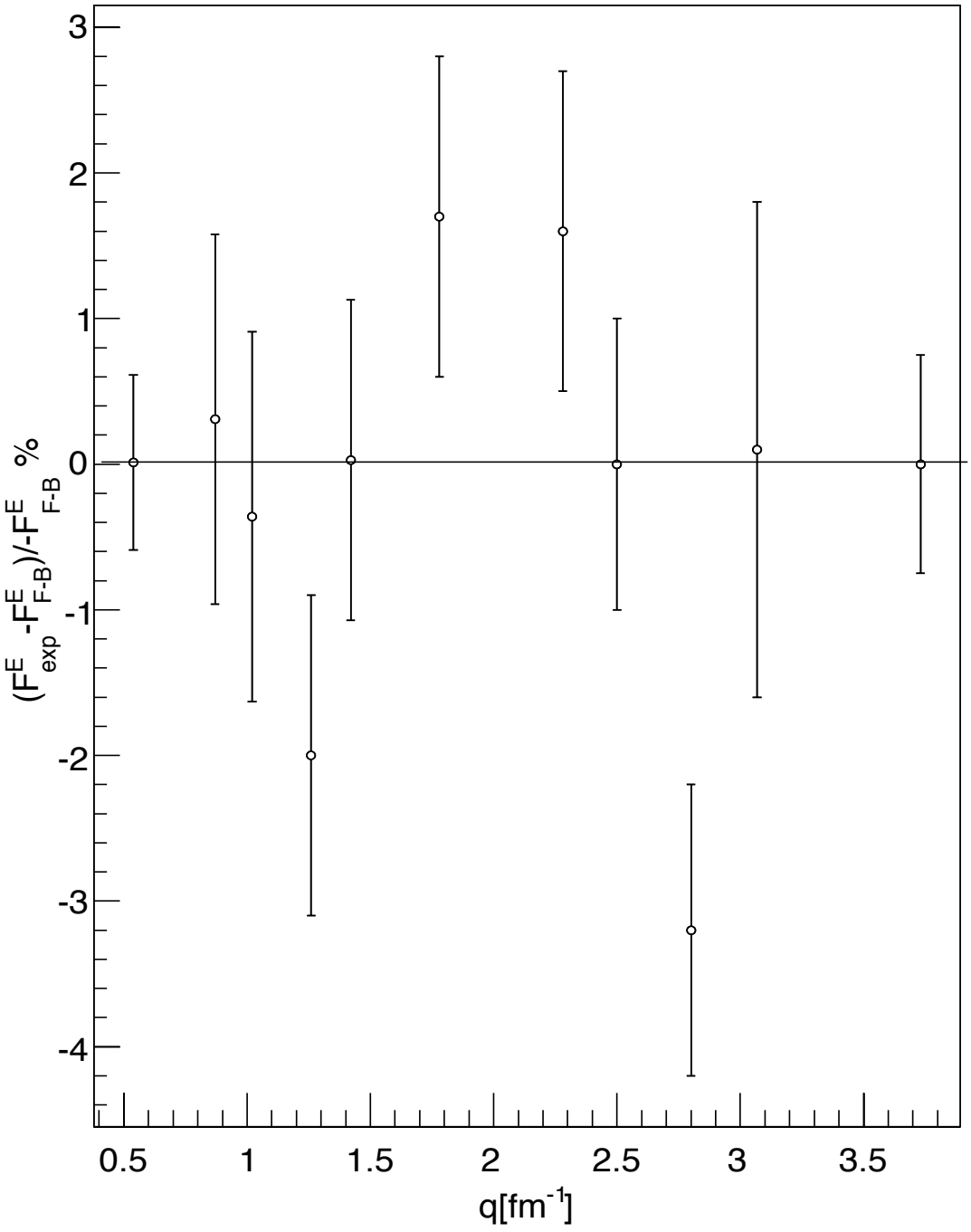

Fig. 6.14: Percentage deviation of the experimental values of form factors from the F-B parametrization results for the deuteron.

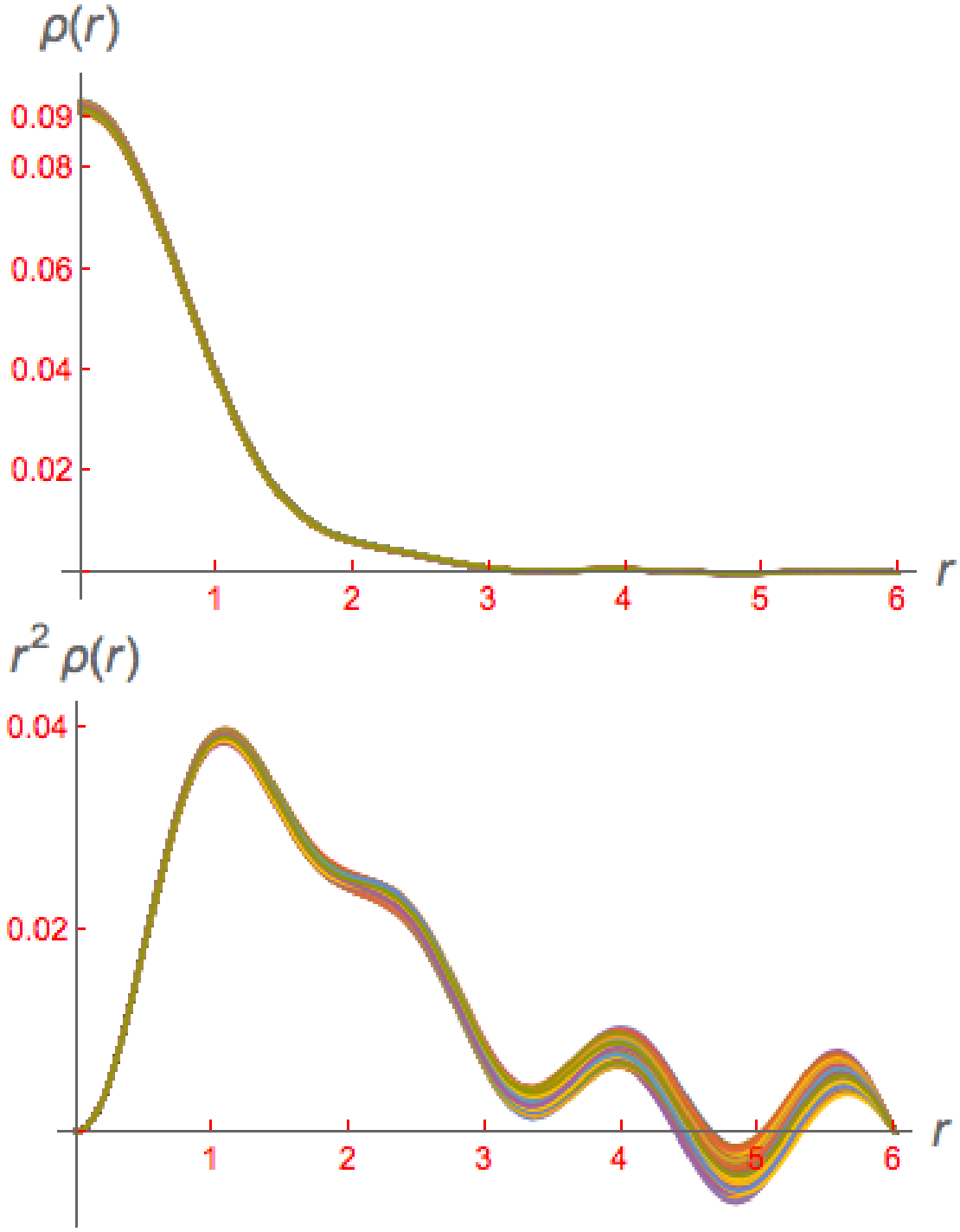

Fig. 6.15: Top diagram is for the deuteron's charge distribution obtained from F-B analysis. In the bottom picture, r^2 is multiplied with the charge density to emphasize the nuclear surface and tail region

The charge radius of the deuteron and its uncertainty were found with the same

scheme as we described for carbon. The result is shown diagramatically in Fig. 6.16, and its numerical value is,

$$\langle r_{rms} \rangle = 2.136 \pm 0.051\, fm.$$

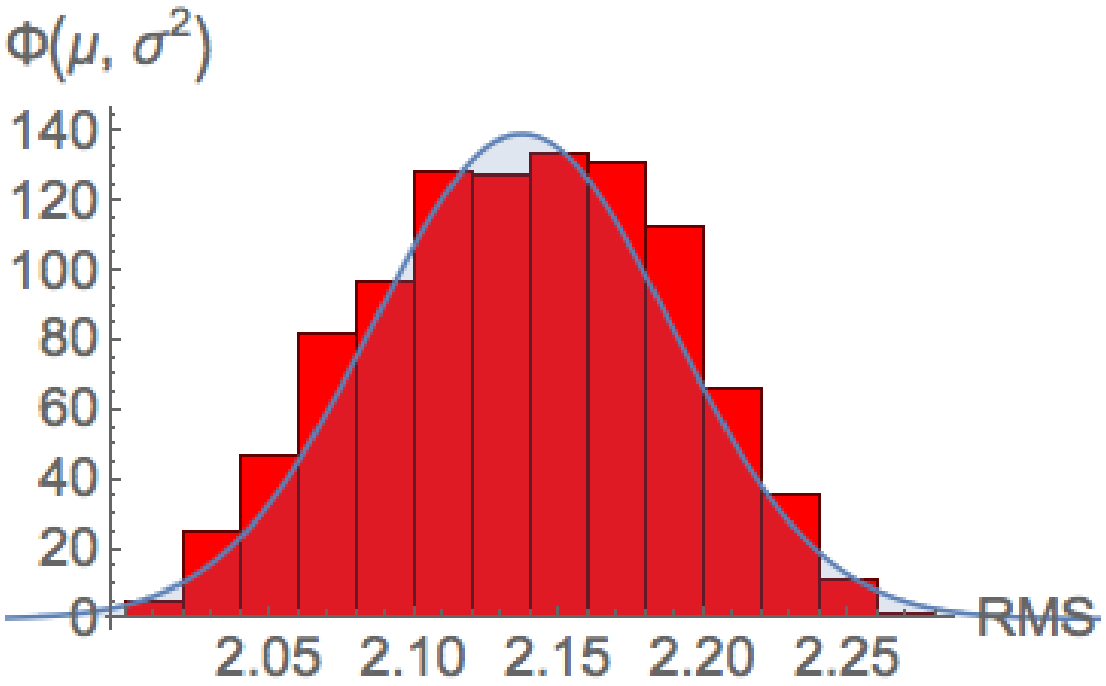

Fig. 6.16: Distribution of deuteron's charge radius results.

The deuteron structure function, A(q), for the LEDEX experiment was measured previously by Byungwuek Lee [31]. We have presented both ours and his data in Fig. 6.17. We also have parametrized the structure function with F-B analysis, which is also shown in this figure.

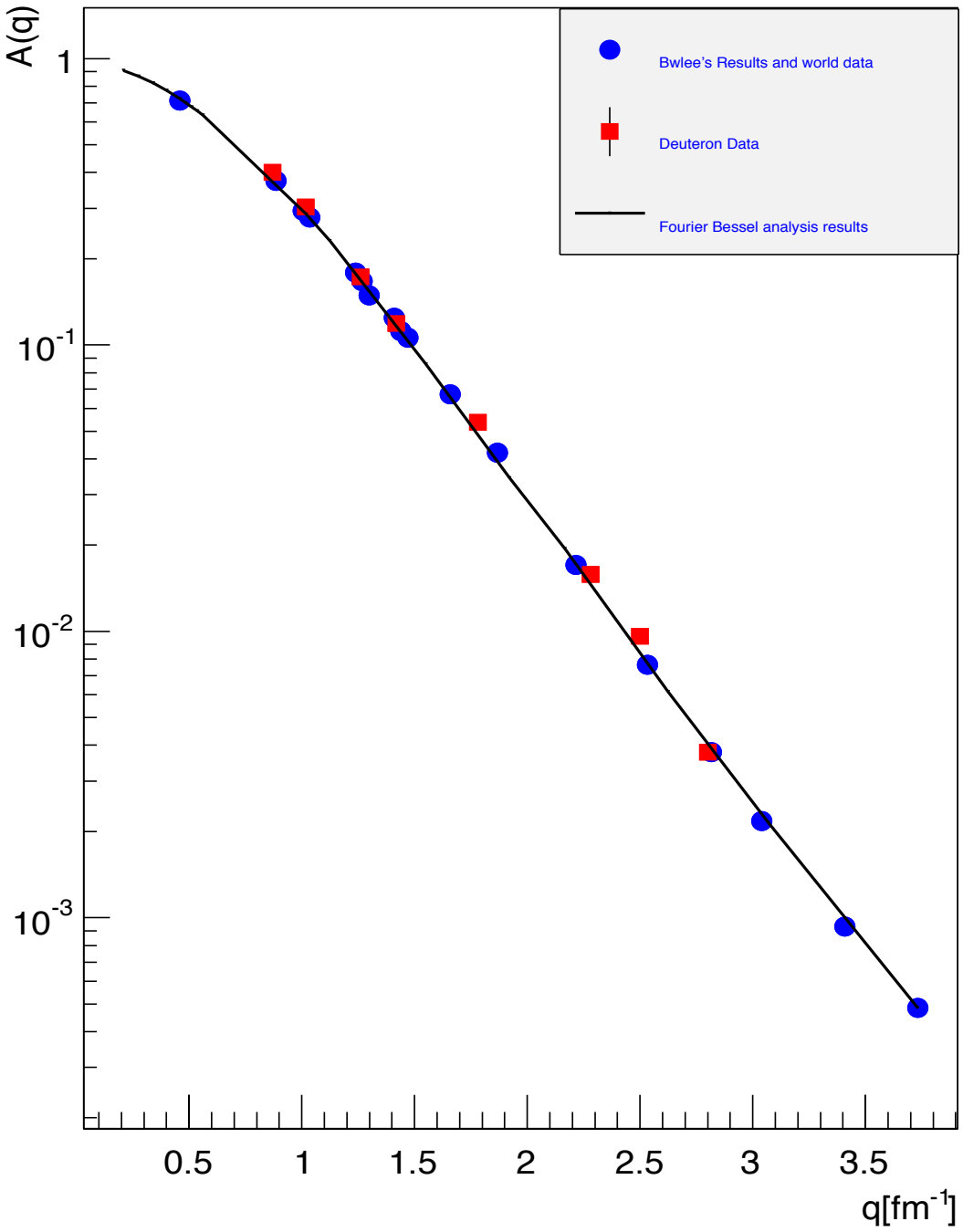

Fig. 6.17: The structure function $A(q)$ for deuteron.

6.1.5 F-B Parametrization and Charge Radius Result for Hydrogen

Carbon is a spin-zero nucleus, so the quantity, $F^2 = \sigma_{red} = \frac{\sigma}{\sigma_{mott}}$, is all electric. However, the hydrogen is a spin-half nucleus so its reduced crosssection has both electric and magnetic contributions. The Rosenbluth separation technique is a well known and widely used method to separate the electric and magnetic contributions in the form factor [30]. This technique requires at least two reduced cross sections at the same momentum transfer but at different angles. That means we would require having different energy settings to do a Rosenbluth separation. We do not have these two measurements in this experiment, so, we need to use other information.

We know from other experimental results [61] [62] that the ratio G_E/G_M is almost unity. Furthermore, we see the deviation of this ratio from unity is smaller than our experimental uncertainty. We make use of this information to find the relation between σ_{red} and G_E as follows,

$$\begin{aligned}
\sigma_{red} &= [2\tau \tan^2(\frac{\theta}{2})G_M^2 + \frac{G_E^2 + \tau G_M^2}{1+\tau}] \\
&= [2\tau \tan^2(\frac{\theta}{2})G_E^2 + \frac{G_E^2 + \tau G_E^2}{1+\tau}] \\
&= [2\tau \tan^2(\frac{\theta}{2}) + 1]G_E^2
\end{aligned}$$

At low angles and small momentum transfers, the contribution from the $2\tau \tan^2(\frac{\theta}{2})$ is negligible but, at larger angles, the contribution from this factor becomes significant (a few percent). The following table describes the situation:

After finding the charge form factors, we parametrize them with the Fourier-Bessel (F-B) ansatz as described in the previous section. Here, we choose 4 fm as a

Table 6.9: Correction factors due to the magnetic contribution

Angle (°)	$q[\mathrm{fm}^{-1}]$	$1 + 2\tau \tan^2(\frac{\theta}{2})$
30.5	1.76	1.01
40.0	2.20	1.01
45.0	2.42	1.02
50.5	2.64	1.04

cut-off radius and we determine the first six coefficients. We took the first three form factors from our experimental results and last three from references: [61, 62]. Figure 6.23 shows the charge distribution drawn from these coefficients. The figure shows clearly an unphysical oscillation at the tail of the distribution that makes it difficult to extract an unambiguous charge radius result.

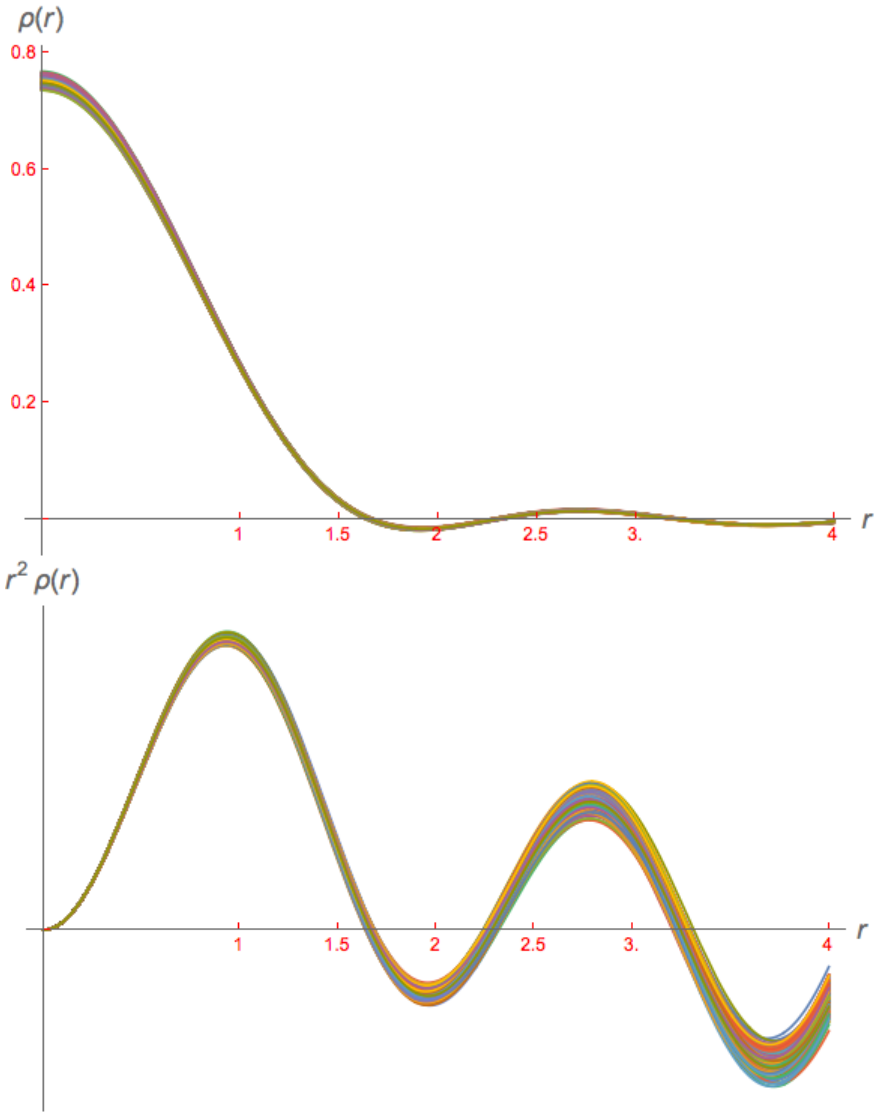

Fig. 6.18: Top diagram is for hydrogen's charge distribution obtained from F-B analysis. At the bottom picture, r^2 is multiplied with the charge density to emphasize the nuclear surface and tail region. Different colors of the diagram coreespond to N different sets of coefficients we evaluated by a random number generation technique.

A F-B analysis relies on the fact that at a large enough distance from the center of the nucleus, the charge distribution is zero. In reality, the true charge distribution of the proton has an exponential tail. Sick and Trautmann, in a recent paper [63], suggested that one needs to choose a cut-off radius about three times larger than the rms radius of the hydrogen nucleus. Indeed, we have taken this into account and

placed the cut off radius roughly at four times the rms radius.

On the other hand, the form factor as a Fourier transform is defined in the Breit frame (also known as the brick wall frame). In this frame, an electron will rebound at the same momentum as it's incident momentum and thus exchanges no energy. However, the hydrogen nucleus is relatively light and there will be a significant recoil in a collision event with electrons. This recoil effect can be addressed by making changes in the formulas for momentum transfer and the charge form factor, in the following manner [64],

$$k^2 = \frac{q^2}{1+\tau}, \tag{6.13}$$

$$G_E(k) = G_E(q)(1+\tau)^{\lambda}, \tag{6.14}$$

Where, λ is a model dependent parameter. The value of λ is 0 according to the soliton model [65], 1 according to the cluster model [66], and 2 in the perturbative QCD model (PQCD) [67]. We have taken all these models into account and have performed calculations for each of them. Figures 6.19 and 6.20 compares of the charge density behaviors for these models .

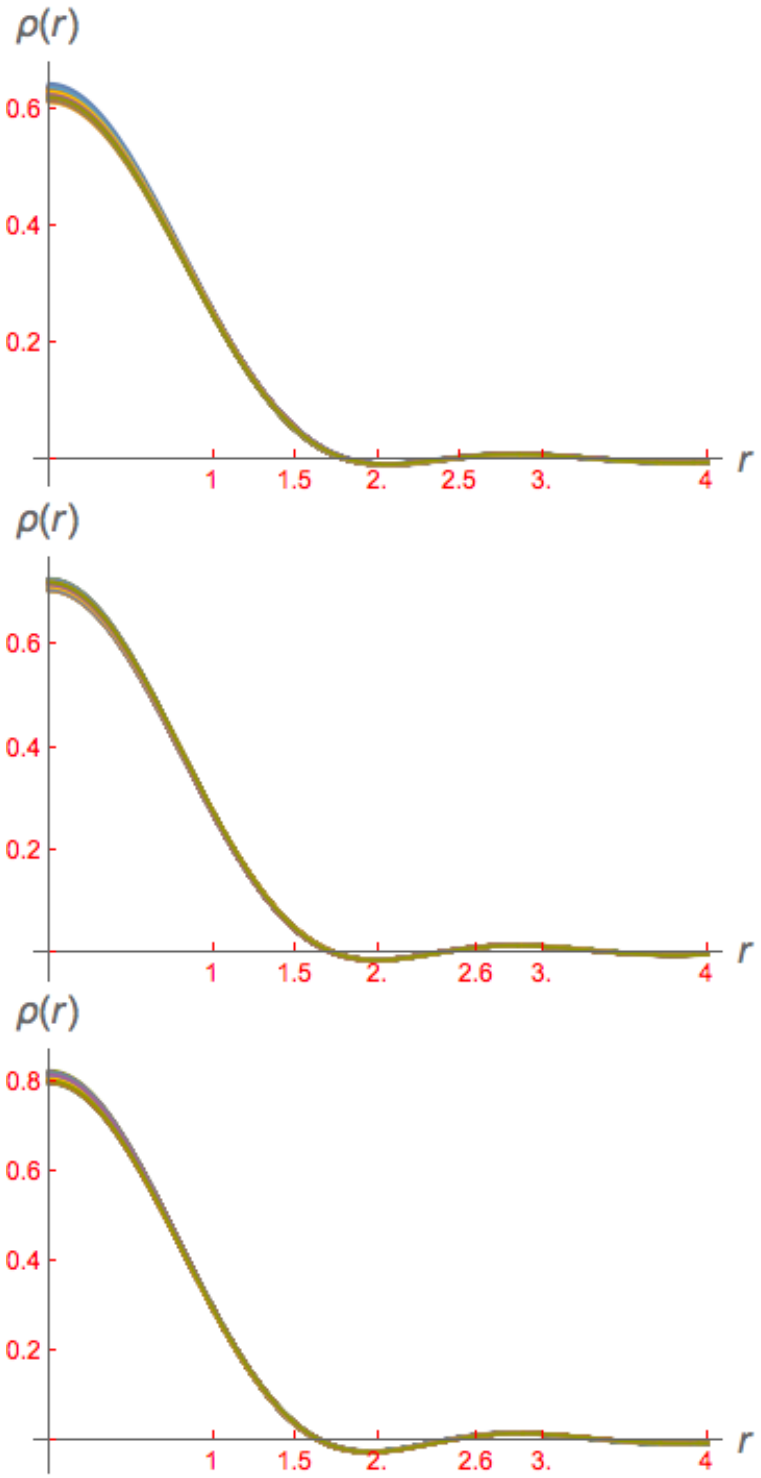

Fig. 6.19: Charge distribution for Hydrogen. Top diagram is for soliton model, middle is for cluster, and bottom one is for the perturbative QCD model

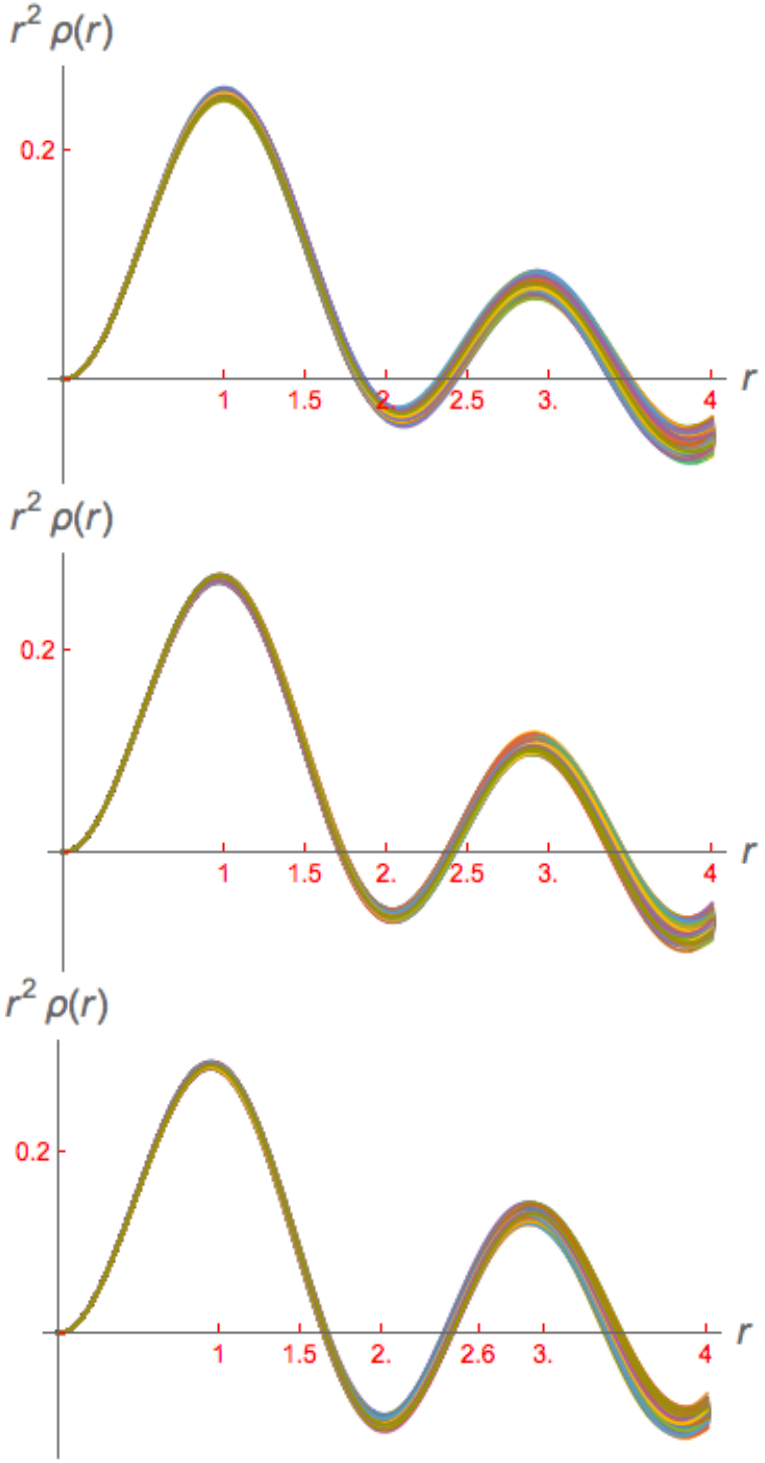

Fig. 6.20: Tail behavior $[r^2\rho(r)$ plot] for $\lambda = 0, 1, 2$, respectively, for the soliton (top), cluster (middle), and PQCD (bottom) models.

It is quite obvious from the charge density distribution diagram that none of the models removes the oscillations at the tail; the soliton model has the fewest and the PQCD model has the most oscillations. These oscillations completely blow up the charge-radius extraction; in fact, integrating eq. 6.8 over the full cut-off radius yields an imaginary number for the charge radius value, although it describes the experimental data surprisingly well! In order to extract a meaningful charge radius, we reduced the integration limit to around the point R_{red} where the charge distribution function hits the first zero (which is around half of the cut-off radius), and such that it gives the correct normaliztion ($Z = 1$). With this, r^2 does not suffer the frenzy in oscillation at large r. However, it is also observed that moving the integration limit also moves the charge radius result to some extent. Tables 6.10, 6.11 summarize the results from the F-B analyses:

Table 6.10: F-B coefficients for hydrogen

ν	$a_\nu(\lambda = 0)$	$a_\nu(\lambda = 1)$	$a_\nu(\lambda = 2)$
1	0.0229 ± 0.00045	0.0230 ± 0.00044	0.0232 ± 0.00044
2	0.0720 ± 0.00083	0.0739 ± 0.00084	0.0762 ± 0.00084
3	0.1219 ± 0.00153	0.1302 ± 0.00151	0.1373 ± 0.00148
4	0.1512 ± 0.00169	0.1693 ± 0.00168	0.1853 ± 0.00154
5	0.1546 ± 0.00184	0.1870 ± 0.00186	0.2229 ± 0.00177
6	0.1099 ± 0.00414	0.1412 ± 0.00417	0.1630 ± 0.00413

Table 6.11: Charge radius result for hydrogen with F-B analysis.

λ	R_{red}	$\int_0^R \rho(r) d^3r$	ξ_λ	r_λ
0	2.045	1.00003	0.91 ± 0.015	0.91 ± 0.014
1	2.02	1.0034	0.89 ± 0.014	0.86 ± 0.014
2	2.02	1.0063	0.88 ± 0.015	0.79 ± 0.013

Here, R_{red} is the reduced cut-off radius. ξ_λ is the model independent charge radius result which is based upon taking the derivative of the charge form factor without any recoil effect ($\langle \xi_\lambda^2 \rangle = -6 \frac{dF_{ch}(q^2)}{dq^2}|_{q \to 0}$), whereas, r_λ is model dependent and these are related to each other by [64]:

$$r_\lambda^2 = \xi_\lambda^2 - \frac{3\lambda}{2m^2}. \tag{6.15}$$

It is quite obvious from Table 6.11 that there is a large model dependence to the extracted charge radius for hydrogen.

6.2 Results With a Few Other Parametrization Models for Hydrogen

As we have seen, the F-B parametrization technique has some drawbacks in extracting the charge radius; therefore, we also tried some other available parametrizations. Among them, a few do very well in explaining our charge form factor values and a few reveal some interesting insights. We will discuss them one by one in this section.

The most promising parametrization we found during our study is the inverse

polynomial expansion [68] which has the following form:

$$F_{ch} = G_E = \frac{1}{1 + p_0 q^2 + p_1 q^4 + p_3 q^6} \tag{6.16}$$

We started with the lowest-order term and then added higher-order terms to observe which order of polynomial best describes our experimental results. This has been illustrated in figs. 6.21, 6.22 Figure 6.21 shows fits through the experimental points and Fig. 6.22 shows an extrapolation of fit function to $q = 0\,\mathrm{fm}^{-1}$.

It is clear from these fitting results that the best fit function for our experimental data is,

$$F_{ch} = G_E = \frac{1}{1 + p_0 q^2 + p_1 q^4} \tag{6.17}$$

Differentiating this equation with respect to q^2 and multiplying with the necessary factors to find the charge radius according to eq. 6.7, we obtain

$$\langle r^2_{rms} \rangle = -6 \frac{dF_{ch}}{dq^2} = 6 \frac{p_0 + 2p_1 q^2}{(1 + p_0 q^2 + p_1 q^4)^2}. \tag{6.18}$$

When $q^2 = 0$, it becomes $\langle r_{rms} \rangle = \sqrt{6 p_0}$. So, in this parametriztion model with $p_0 = 0.133 \pm 0.0051\,\mathrm{fm}^2$, the value of hydrogen charge radius is;

$\langle r_{rms} \rangle = 0.894 \pm 0.017\,\mathrm{fm}^{-1}$.

The uncertainty here on the rms radius comes purely from the uncertainty in the fit parameter p_0. However, during our study we found that if the form factor values change, then the charge radius also changes. Assigning errors this way may not reflect this fact. To find the spread of charge radii due to the change in value of the form factors is deduced as follows:

We kept statistical and random systematics on the form factors. Then we subtracted the correlated systematic to the nominal values of form factors and fit them with a fit function (Eq. 6.17) to extract the highest possible value of the charge-radius [57]. Then we fitted with the maximum values (added correlated systematics

to the nominal values) of form factors and then only with nominal values (Fig. 6.23). We observed that a 0.02 fm shift in either direction from the nominal value of charge-radius is possible due to the correlated systematics. On the other hand, random and statistical uncertainties contributed a ± 0.004 fm uncertainty to the charge-radius result.

$\therefore < r_{rms} > = 0.89398 \pm 0.02\,(\text{correlated}) \pm 0.004\,(\text{uncorrelated})\,\text{fm}.$

Note that the result above is for the two-parameter inverse polynomial fit function.

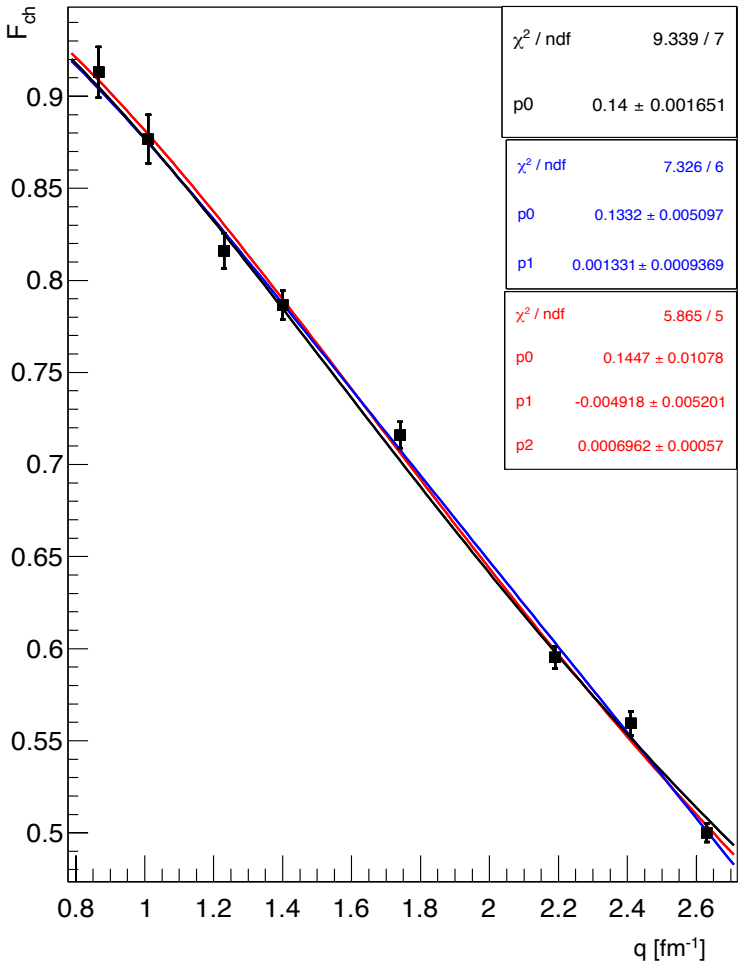

Fig. 6.21: Inverse polynomial fit of hydrogen form factor.

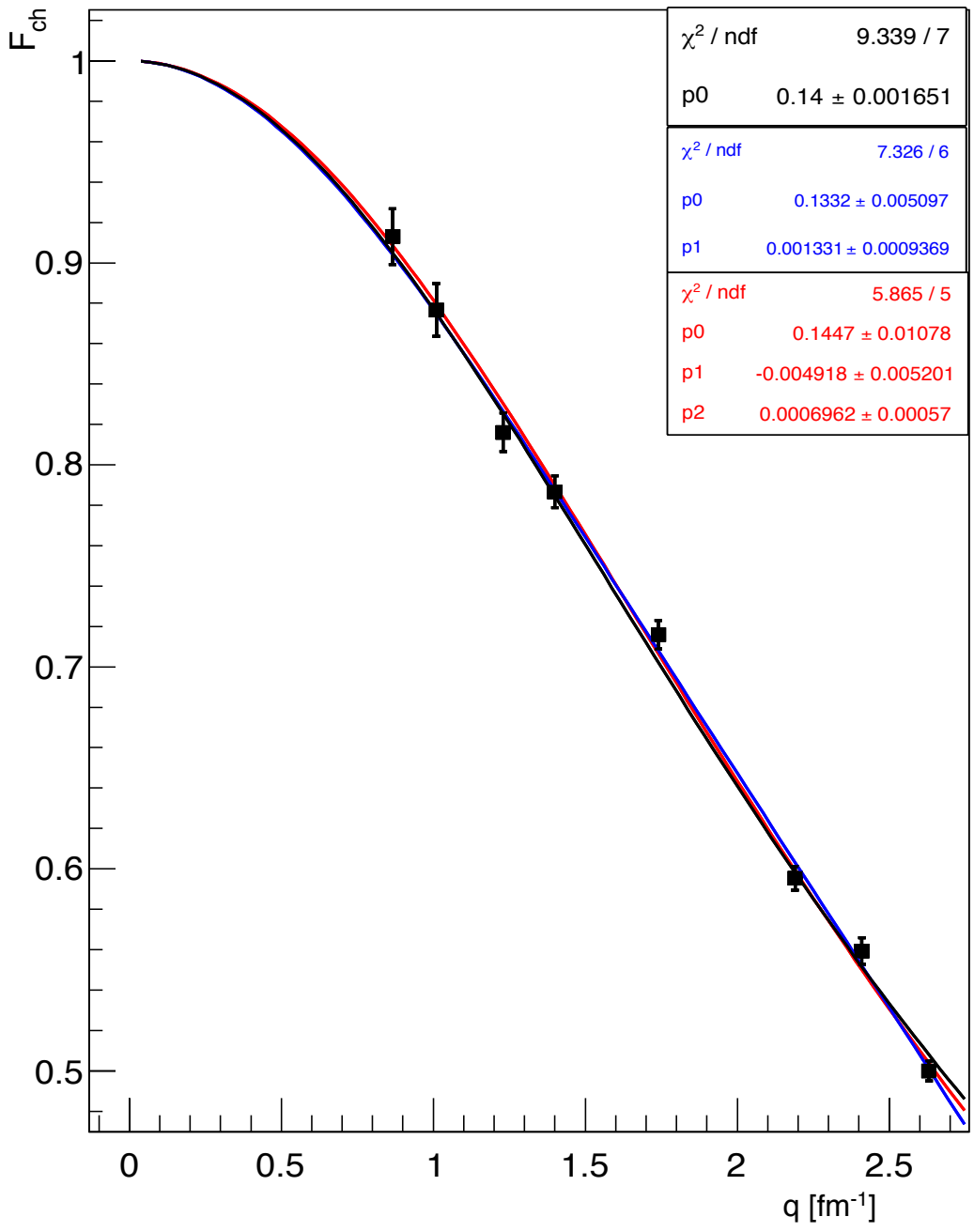

Fig. 6.22: Extrapolation of Inverse polynomial fit for hydrogen form factor to low q.

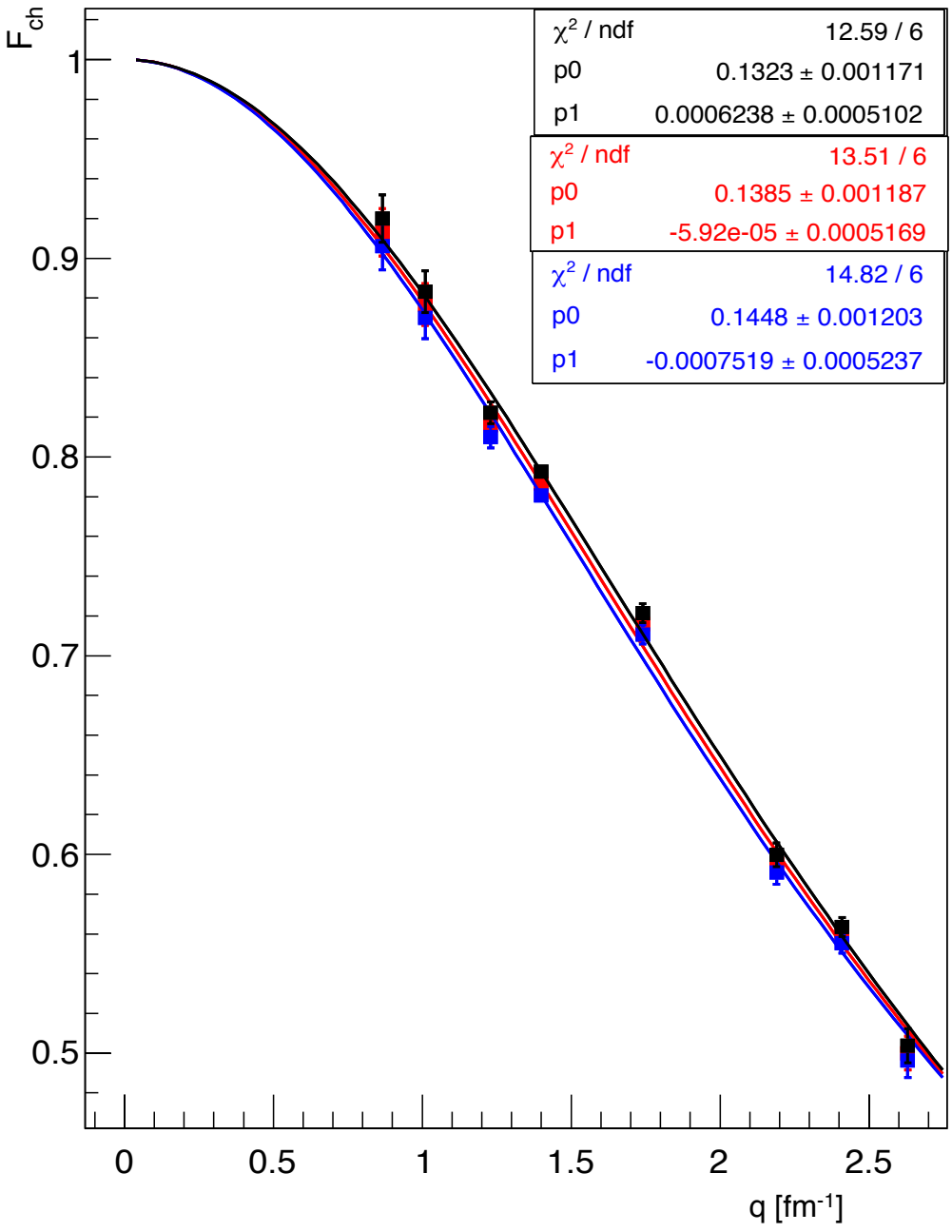

Fig. 6.23: Fitting hydrogen data with inverse polynomial function. Black points represent the maxima of the form factor and blue are the minima.

The next promising model we tried uses an expansion in $\tau = \frac{q^2}{4m^2}$, both in the

numerator and denomenator as a functional form of the charge form factor [69],

$$F_{ch} = \frac{1 + \sum_{k=1} a_k \tau^k}{1 + \sum_{k=1} b_k \tau^k} \tag{6.19}$$

We tried several combinations, but keeping only one or two coefficients in the denomenator shows very good agreement. The parametrization result is depicted Fig. 6.24 .

Although the derivative of the one- and two-parameter fit functions with respect to q^2 have different forms, - $\frac{p_0}{4m^2(1+p_o\tau)^2}$ and -$\frac{\frac{p_0}{4m^2}+\frac{p_1}{2m^2}\tau}{(1+p_0\tau+p_1\tau^2)^2}$, respectively, at $q = 0$ the slope reduces to just $-\frac{p_0}{4m^2}$. So, the charge radius can be extracted using, $\langle r_{rms}\rangle = \sqrt{\frac{6p_0}{4m^2}}$.

From the one parameter fit we obtain, $\langle r_{rms}\rangle = 0.912 \pm 0.006\,\text{fm}$, and using the two parameter fit we obtain, $\langle r_{rms}\rangle = 0.894 \pm 0.017\,\text{fm}$.

We found that if our overall uncertainty were larger by 1% then the dipole approximation would be a very good fit in that case. Fig. 6.25 illustrates this situation. The charge radius value in this case would be $0.853 \pm 0.007\,\text{fm}$.

Throughout our analysis, we have seen that the charge radius depends primarily on the value of only one parameter. This lead us to investigate the possibility of fixing the parameter responsible for the charge radius and tuning others (remaining parameters) so that we could describe experimental data. We infact were able to do that, which is shown in the Fig. 6.25. In this way, we see that one can "obtain" nearly any result that one wishes for the charge radius of the hydrogen nucleus (the proton).

Since, we have data only in the moderate momentum transfer range ($0.17 < q\,[\text{GeV}/c] < 0.52$), we performed a gobal analysis taking the Saskatoon [70] and Mainz [71] data in the low-momentum transfer regime $0.07 < q\,[\text{GeV}/c] < 0.24$ and

Jlab data [62] for the high-momentum transfer regime. At first, we tried the lowest-order polynomial fit function or the dipole fit [fig: 6.26] and then with an inverse polynomial fit function [Fig. 6.28]. The charge radius from the dipole fit is found to be 0.849 ± 0.004 fm, whereas the inverse polynomial gives 0.861 ± 0.003 fm. It is to be noted that only the statistical uncertainty is counted on the Saskatoon and the Mainz data during the analysis.

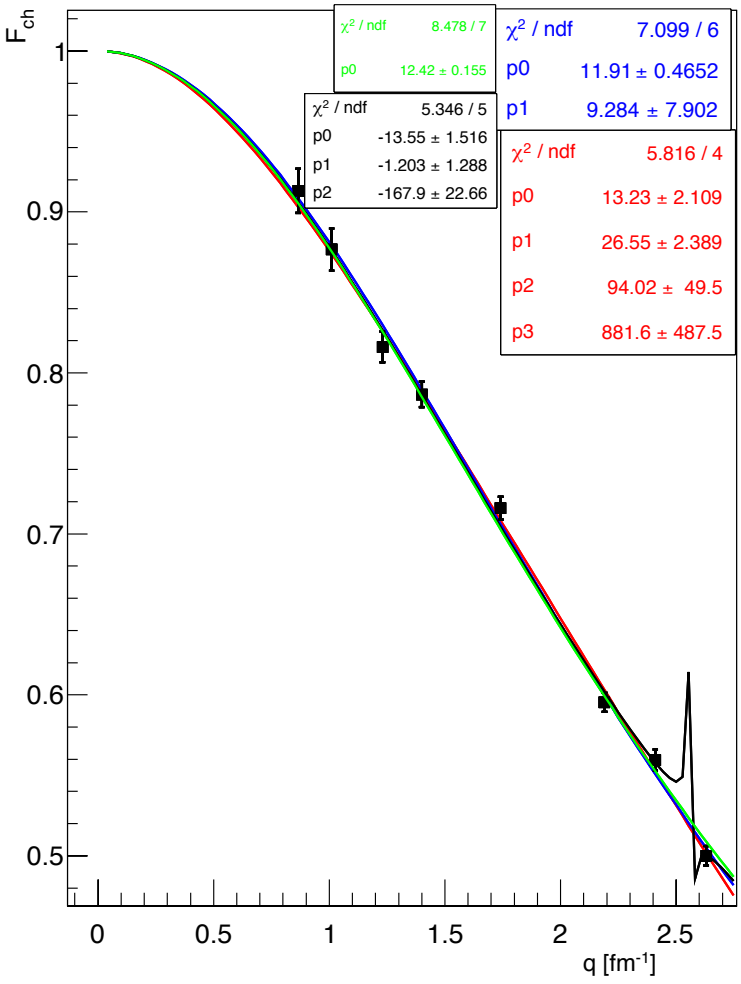

Fig. 6.24: Data fitting. The green curve corresponds to $\frac{1}{1+p_0\tau}$ and the blue curve corresponds to $\frac{1}{1+p_0\tau+p_1\tau^2}$. Red curve is not disscussed because of its large χ^2/ndf value, whereas, black curve is ommitted because of it has an ambiguious jump around $q = 2.5$ fm^{-1}.

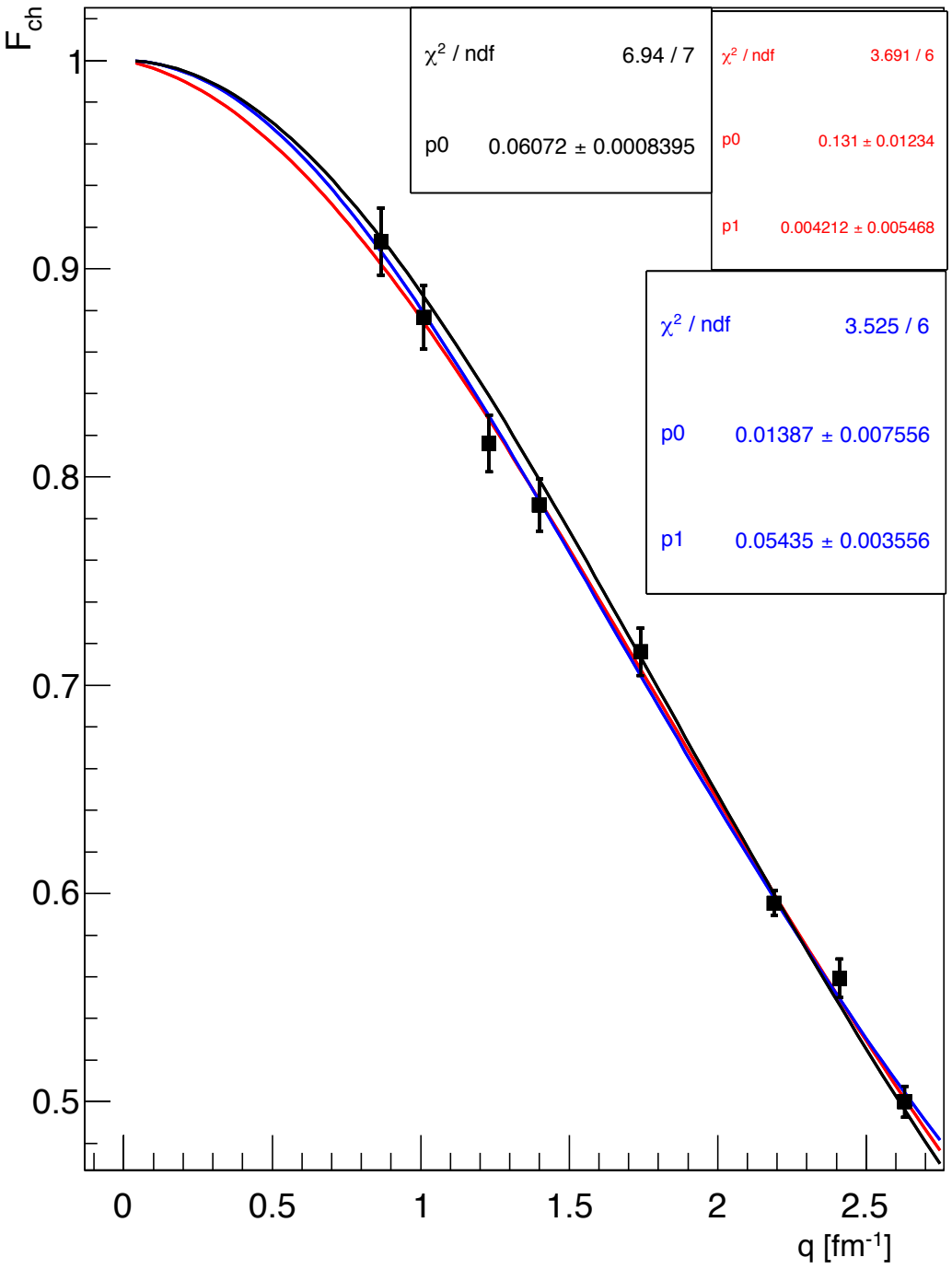

Fig. 6.25: Charge form-factor parametrization. The black line corresponds to $\frac{1}{(1+p_0 q^2)^2}$. Other models were rejected based on their χ^2 values.

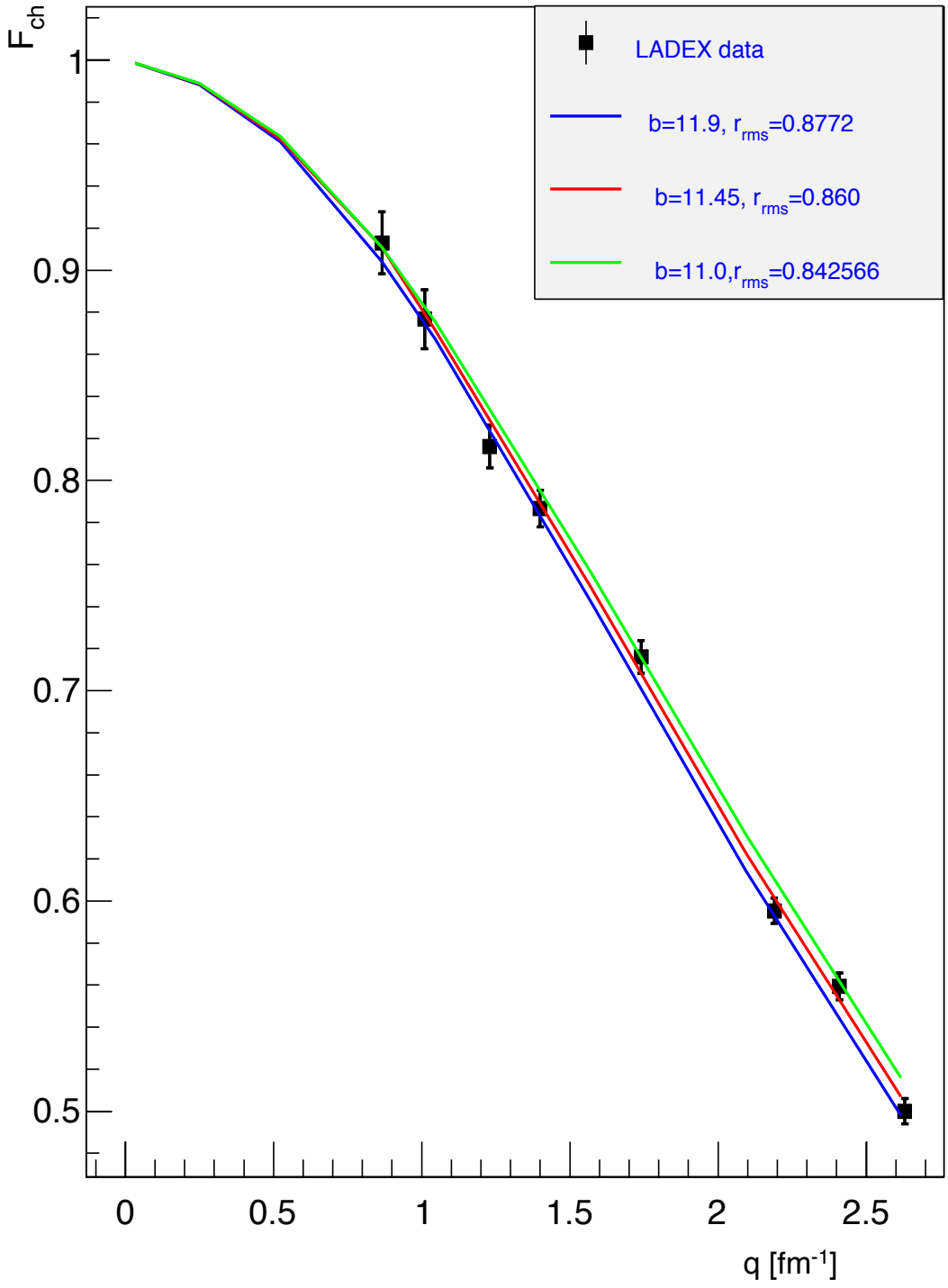

Fig. 6.26: Manipulating charge radius result. Here we have used Kelly's model [69]. The χ^2/N for the blue,red and green curve are $\sim$ 0.8,0.6 and 0.6 respectively

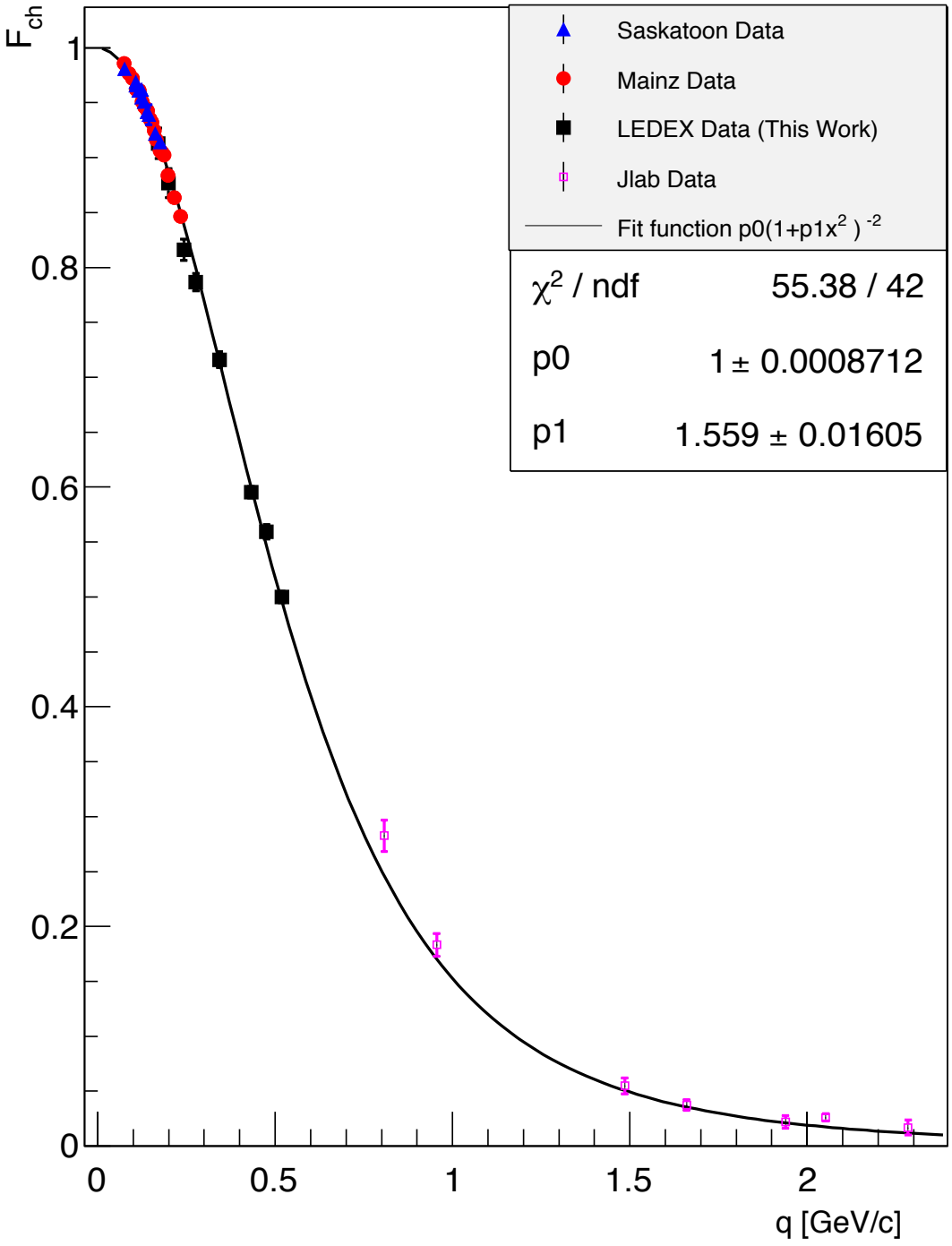

Fig. 6.27: Dipole fit to hydrogen world data.

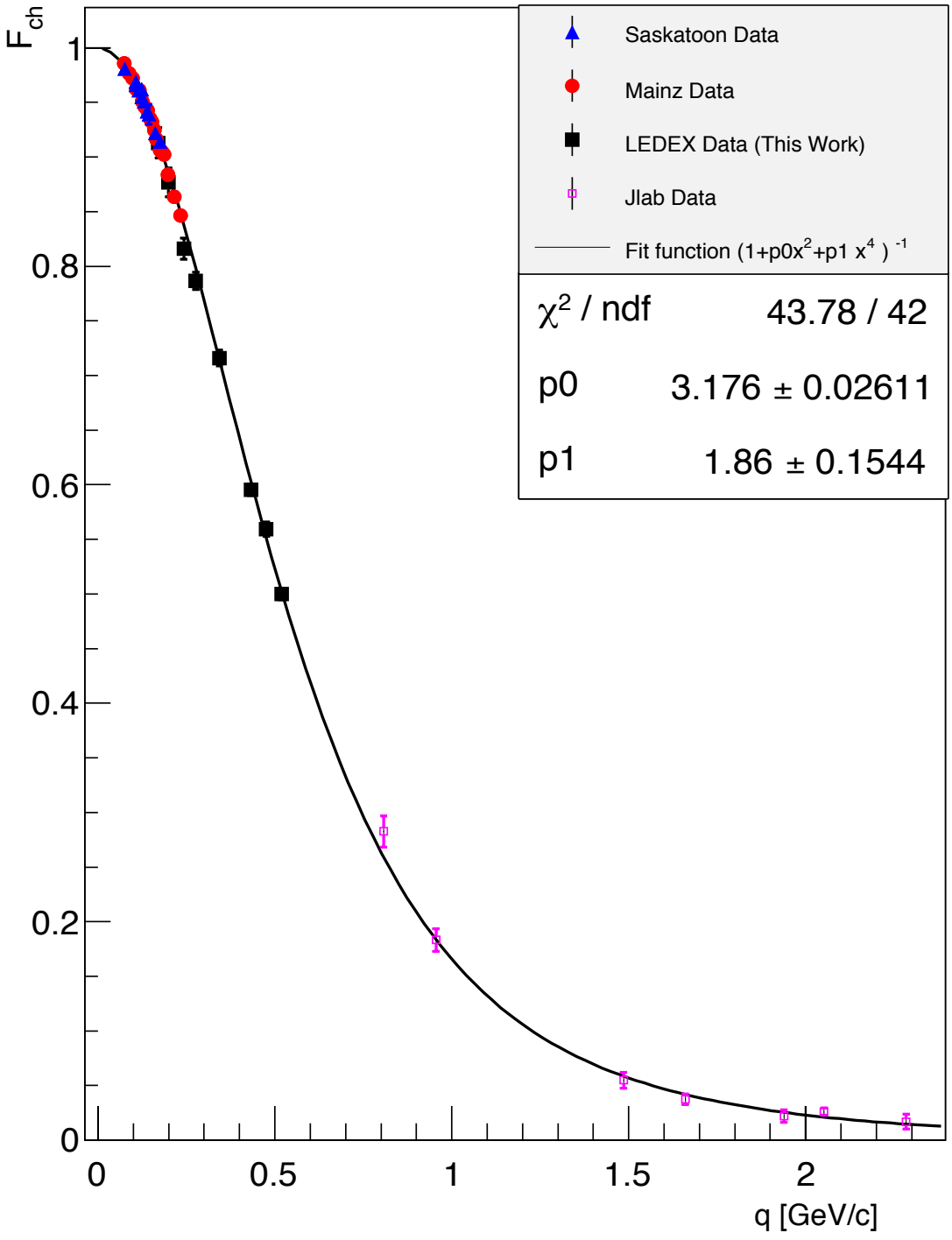

Fig. 6.28: Inverse polynomial fit to hydrogen world data.

Table 6.12 gives a summary of results for hydrogen that we obtained with different parametrizations.

Table 6.12: Charge radius results for hydrogen

Parametrization	Data Source	$r_{\rm rms}$ [fm]
$\frac{p0}{(1+p1q^2)^2}$	$LEDEX + Saskatoon + Mainz + JLab$	0.849 ± 0.004
$\frac{1}{1+p0q^2+p1q^4}$	$LEDEX + Saskatoon + Mainz + JLab$	0.861 ± 0.003
F-B (Soliton)	$LEDEX$	0.912 ± 0.0147
F-B (Cluster)	$LEDEX$	0.893 ± 0.0142
F-B (PQCD)	$LEDEX$	0.879 ± 0.0147
$\frac{1}{1+p0q^2+p1q^4}$	$LEDEX$	$0.894 \pm 0.02 \pm 0.004$
$\frac{p0}{1+p1\tau^2}$	$LEDEX$	0.912 ± 0.006
$\frac{p0}{1+p1\tau^2+p2\tau^4}$	$LEDEX$	0.894 ± 0.0178
$\frac{1}{(1+p0q^2)^2}$	$LEDEX$	0.853 ± 0.007
$\frac{p0}{1+11.9\tau^2+p1\tau^4}$	$LEDEX$	0.877
$\frac{p0}{1+11.45\tau^2+p1\tau^4}$	$LEDEX$	0.860
$\frac{p0}{1+11.0\tau^2+p1\tau^4}$	$LEDEX$	0.842

We have seen so far that there is no definite conclusion can be drawn about the charge-radius of hydrogen either from the LEDEX data or from the existing world data set following usual techniquess. There is also a strong model dependence in determining the charge-radius of hydrogen. However, we made a striking observation that if we restrict ourselves to only the low q^2 (upto 0.40 fm^2) Saskatoon and Mainz data, all the parametrizations coincide and all generate a consistent charge radius ($\sim 0.84 \pm 0.01$ fm) [72]; a value closer to the muonic-hydrogen result. On the other hand, inclusion of data points at high q^2 in the parametrization results in an increase in the charge-radius value. Figure 6.29 shows parametrizations of low q^2 Saskatoon and Mainz data with Monopole ($ao[1-a_1 \times q^2]^{-1}$), dipole ($ao[1-a_1 \times q^2]^{-2}$), Gaussian ($a0\exp[a1 \times q^2]$), and Taylor(N=1) ($ao[1 + a_1 \times q^2]$) functional forms.

The point that one should consider only the lowest momentum transfer data in extracting the charge radius is not unreasonable. If we look at the assumption to define the charge radius as the slope of form factor (Eq. 6.7), we immediately see that the formula is ill defined for high q^2. Recently, Keith Griffioen *et al.*, analyzed the latest Mainz data on hydrogen [73], and they came to a conclusion very similar to this.

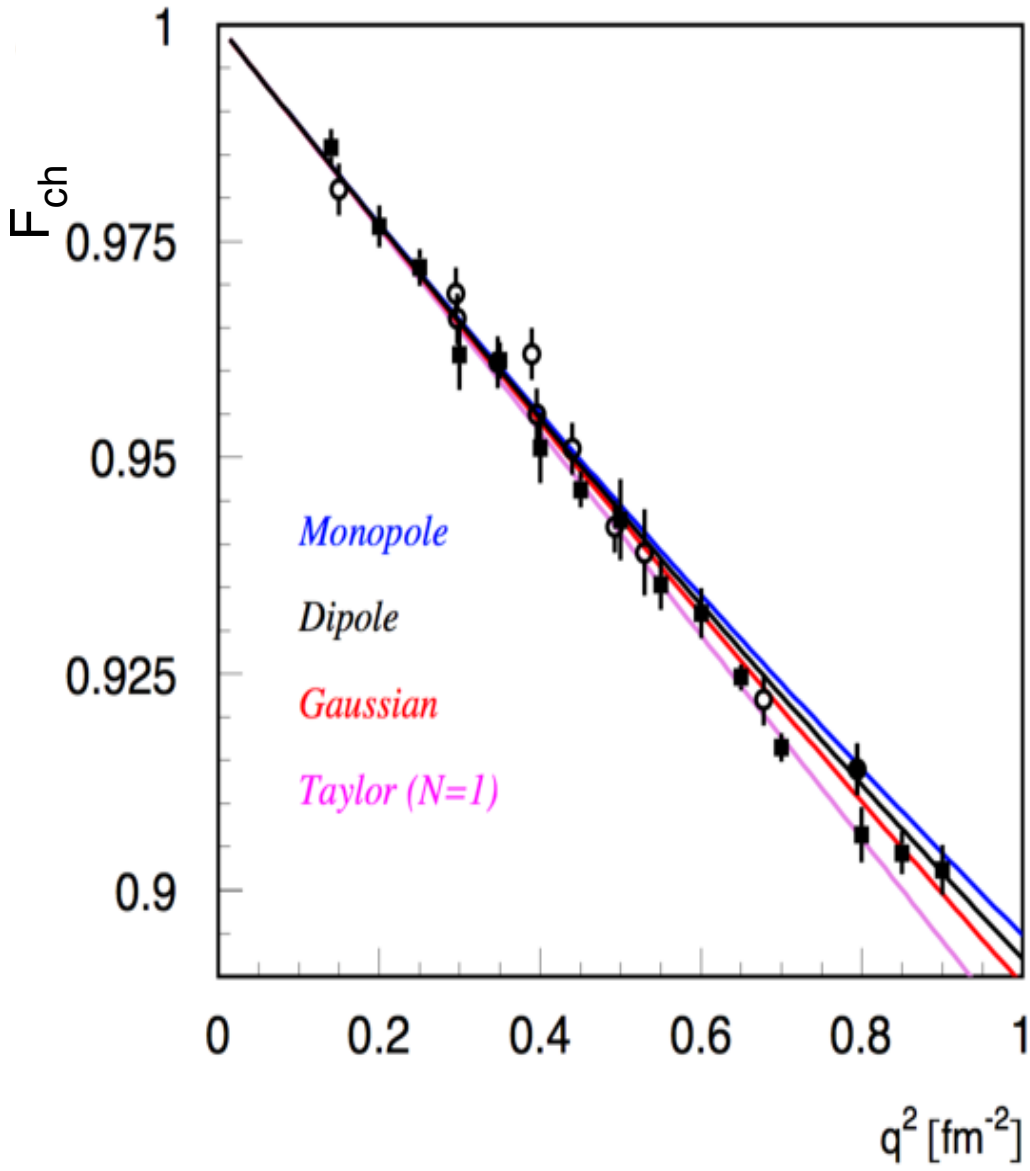

Fig. 6.29: Fitting of low q^2 data from Saskatoon, open circles, and Mainz, solid squaresare with monopole, dipole, Gaussian, and Taylor (N=1) functional forms with a radius set to the muonic Lamb shift result of 0.84 fm for a q^2 up to 1 fm^2 [72] .

Chapter 7

CONCLUSIONS

High-energy electron scattering has been a useful tool for studying charge distributions in nuclei for several decades. Recent work to extract the rms charge radius of hydrogen from the analysis of the Lamb-shift in muonic hydrogen has yieldedided a significantly different result than that from electron scattering analyses. Part of the motivation for this work was to provide a new, independent analysiss of high-energy electron scattering on hydrogen to help adress this discrepancy. At the same time, we have also analyzed new measurements for several less studied light nuclei.

For this dissertation, the elastic scattering cross sections for carbon (^{12}C), boron (^{10}B), lithium (^{6}Li), Deuterium (^{2}H) and hydrogen (^{1}H) were obtained. Whenever necessary, the magnetic scattering contribution is approximated and substracted from the total cross section to find the electric (charge) elastic scattering cross section. The charge form factor is then described with the model independent Fourier-Bessel parametrization which does not depend on the details of the charge distibution, e.g., skin depth. The charge distribution and the charge radius for each of these nuclei was then obtained.

Our charge radii results, 2.45 ± 0.09 fm for ^{12}C, 2.425 ± 0.122 fm for ^{10}B, 2.519 ± 0.048 fm for ^{6}Li, and 2.136 ± 0.051 fm for ^{2}H show excellent agreement with the latest theoretical calculations of ~ 2.46 fm for ^{12}C, ~ 2.43 fm for ^{10}B, 2.53 fm for ^{6}Li, and ~ 2.146 fm for ^{2}H, obtained from a Green's function Monte Carlo (GFMC) approach [74, 75]. However, in the theoretical calculations for the charge radii of ^{10}B, and ^{6}Li, values from two contributions, spin-orbit and meson-exchange currents have yet to be determined, but these contributions are estimated to be very small [76].

In our study, we found that the F-B parametrization technique works quite well for the heavier nuclei, such as ^{12}C, ^{10}B, and ^{6}Li , but starts to have difficulty as the nuclear mass decreases. It is shown in this dissertation that this somehow still works for deuterium with some ambiguity (i.e., tail oscillations) but it is very questionable for hydrogen.

We think that this is due to the recoil associated with the lighter nuclei and their large exponential tail in the high q^2 region, unlike the heavier nuclei whose tails fall much more sharply. To recreate such a long exponential tail with the F-B parametrization, the cut-off radius has to be very large, which will eventually leave us with a unreasonably large set of F-B coefficients.

We therefore, moved to more usual parametrization techniques that calculate the slope of the form factor at $q^2 = 0$. These parametrization techniques have their own difficulties. There are no data available to test the models below $q = 0.17$ fm^{-1}, and, at very low q the form-factor results with various parametrization models started to coincide and to predict unity at $q = 0$. We observed also that at low and medium q regions, there are many models that can describe our data as well, but produce different charge radius results. Also, it is also possible to tune the parameters so that they describe the data reasonably well but produce different results for the charge radius from the muonic hydrogen result to the CODATA value. In fact, this trend can be seen in the history of the determination of the proton's charge radius; the older experiments [77], [70] and their analyses with lowest-order polynomial fits yield a value closer to the muonic hydrogen result; but the latest higher-order polynomial fits, along with some newer data sets, [71] produce a much larger charge-radius results (closer to the CODATA result). Possibly, lower q measurements may resolve this ambiguity.

We also have doubt about how precisely the proton's charge radius can be known

from the elastic scattering data. The charge radius and the uncertainty on it with the usual parametrization techniques come from only one of the parameters at the end, but we found that the result varies substantially if we take the form factor values at its systematic extremes. We think that a study of the correlations between the fit parameters needs to be conducted on the previous data sets and the uncertainty on the charge radius has to be revised before one can compare with the results from the Lamb shift of muonic hydrogen. This study is beyond the scope of this project.

BIBLIOGRAPHY

[1] E. Lyman, A. Hanson, and M. Scott, Phys. Rev. **84**, 626 (1951).

[2] R. Hofstadter, H. Fechter, and J. Mclntyre, Phys. Rev. **91**, 422 (1953).

[3] R. Hofstadter, H. Fechter, and J. Mclntyre, Phys. ReV. **92**, 978 (1953).

[4] R. Pidd, C. Hammer, and E. Raka, Phys. Rev. **92**, 436 (1953).

[5] R. W. McAllister and R. Hofstadter, Phys. Rev. **102**, (1956).

[6] R. Hofstadter, *The Electron Scattering Method and its Application to the Structure of Nuclei and Neucleon* (Elsevier Pub. Co, Amsterdam-London-New York, 1961).

[7] I. Sick, Phys. Lett. B **576**, 62 (2003).

[8] www.nupec.org/pans/Data/CHAPT4.PDF.

[9] A. Palffy, arXiv:1106.3218v1 (2011).

[10] R. Pohl *et al.*, Nature **466**, 213 (2010).

[11] M. Eides, H.Grotch, and V. Shelyuto, Phys. Rep. **342**, 63 (2001).

[12] K. Pachuki, Phys. Rev. A **53**, 2092 (1996).

[13] K. Pachuki, Phys. Rev. A **60**, 3593 (1999).

[14] E. Borie, Phys. Rev. A **71**, 032508 (2005).

[15] A. Martynenko, Phys. Rev. A **71**, 022506 (2005).

[16] A. Martynenko, Phys. At. Nucl. **71**, 125 (2008).

[17] A. Antognini *et al.*, Science **339**, 417 (2013).

[18] P. Blunden and I. Sick, Phys. Rev. C **72**, 057601 (2005).

[19] P. Mohr, B. Taylor, and D. Newell, Rev. Mod. Phys **80**, 633 (2008).

[20] http://hallaweb.jlab.org/experiment/LEDEX/documents/E05-004-Extended.pdf.

[21] T. Stovall, J. Goldemberg, and D. Isabelle, Nuclear Phys. **86**, 225 (1966).

[22] G. Li, I. Sick, R. Whitney, and M. Yearian, Nucl. Phys. A **162**, 583 (1970).

[23] http://hallaweb.jlab.org/experiment/LEDEX/documents/PR05-004.pdf.

[24] S. Wolfram, The Physics of Subatomic Particles.

[25] E. Rutherford, Philos. Mag **6**, 21 (1911).

[26] Goldstein, *Classical Mechanics*, 3rd ed. (Pearson Education, EdinBurgh Gate, Essex, 2003).

[27] D. Griffith, *Introduction to Elementary Particle Physics*, 2 ed. (Wiley-VCH, New York, 2008).

[28] F. H. A. D. Martin, *Quarks and Leptons An Introductory Course in Modern Particle Physics* (John Wiley and Sons, New York, 1984).

[29] N. F. Mott, Proc. Roy. Soc London A **124**, 425 (1929).

[30] P. R. S. Zetsche, *Particles And Nuclei*, 2 ed. (Springer, Berlin, 1999).

[31] B. Lee, Ph.D. thesis, Seoul National University, 2009.

[32] J. Alcorn *et al.*, Nucl. Inst. Meth. A **522**, 294 (2004).

[33] C. Leemann, D. Douglas, and G. Krafft, Ann.Rev.Nucl.Part.Sci. **51**, 413 (2001).

[34] N. Falletto *et al.*, Nucl. Inst. Meth. A **459**, 412 (2001).

[35] E. A. Long, Ph.D. thesis, Kent State University, 2012.

[36] http://hallaweb.jlab.org/photos/2015/Hall 20A/.

[37] V. A. Sulkosky, Ph.D. thesis, The College of William and Mary, 2007.

[38] P. Monaghan, Ph.D. thesis, Massachusetts Institute of Technology, 2008.

[39] K. G. Fissum *et al.*, Nucl. Instrum. Meth. A **474**, 108 (2001).

[40] http://hallaweb.jlab.org/experiment/LEDEX/.

[41] N. Liyanage, Optics Calibration of the Hall A High Resolution Spectrome- ters using the C Optimizer, Jefferson Lab Hall A Tech. Note (2002).

[42] http://hallaweb.jlab.org/equipment/daq/daq-trig.html.

[43] W. Leo, *Techniques for Nuclear and Particle Experiments* (Springer - Verlag, Berlin, 1987).

[44] http://hallaweb.jlab.org/software/mceep.

[45] J. Schwinger, Phys. Rev. **75**, 898 (1949).

[46] S. Penner, Proceedings of the 18th Scottish Univ. Summer School in Physics, 1977.

[47] L. Mo and Y. Tsai, Rev. Mod. Phys **41**, 205 (1969).

[48] C. Amsler *et al.*, Phys. Lett. B **667**, 1 (2008).

[49] W. R. Leo, *Techniques for Nuclear and Particle Experiments* (Springer-Verlag, Berlin, 1987).

[50] G. Lynch and O. Dahl, Nucl. Inst.Meth. in Phys. Res. B **58**, 6 (1991).

[51] http://hallaweb.jlab.org/experiment/LEDEX/Targets.

[52] E. Offerman *et al.*, Phys. Rev. C **44**, 1096 (1991).

[53] B. Dreher *et al.*, Nuclear Physics A **235**, 219 (1974).

[54] W. Reuter *et al.*, Phys. Rev. C **26**, 806 (1982).

[55] I. Sick and J. Mccarthy, Nuclear Physics A **150**, 631 (1970).

[56] R. Hofstadter, Annu. Rev. Nucl. Sci **7**, 231 (1957).

[57] L. Cardman *et al.*, Phys. Lett **91 B**, 203 (1980).

[58] J. Goldemberg and R. Pratt, Rev. Mod. Phys **38**, 311 (1966).

[59] S. Platchkov *et al.*, Nucl. Phys. A **510**, 740 (1990).

[60] G. Simon, C. Schmitt, and V. Walther, Nucl. Phys. A **364**, 285 (1981).

[61] T. Janssens *et al.*, Phys. Rev. **142**, 922 (1966).

[62] M. Christy *et al.*, Phys. Rev. C **70**, 15206 (2004).

[63] I. Sick and D. Trautmann, Phys. Rev. C **89**, 12201 (2014).

[64] J. J. Kelly, Phys. Rev. C **66**, 065203 (2002).

[65] X. Ji, Phys. Lett. B **254**, 456 (1991).

[66] A. Licht and A. Pagnamenta, Phys. Rev. D **2**, 1156 (1970).

[67] A. Mitra and I. Kumari, Phys. Rev. D **15**, 261 (1977).

[68] E. Kraus *et al.*, Phys. Rev. C **90**, 045206 (2014).

[69] J. J. Kelly, Phys. Rev. C **70**, 068202 (2004).

[70] J. Murphy, Y. Shin, and D. Skopik, Phys. Rev. C **9**, 2125 (1974).

[71] G. Simon, C. Schmitt, F. Borkowski, and V. Walther, Nucl. Phys. A **333**, 381 (1980).

[72] D. Higinbotham *et al.*, arXiv:1510.01293 (2015).

[73] K. Griffioen *et al.*, arXiv:1509.06676 (2015).

[74] J. Carlson *et al.*, Rev. Mod.Phys **87**, 1067 (2015).

[75] Z.-T. Lu *et al.*, Rev. Mod. Phys **85**, 1383 (2013).

[76] R. Schiavilla and R. Wiringa, Private Communication .

[77] L. Hand, D. Miller, and R. Wilson, Rev. Mod. Phys **35**, 335 (1963).